HEAVY FLAVORS
IN HIGH ENERGY ELECTRON-POSITRON COLLISIONS

J.H. Kühn [1] and P.M. Zerwas [2]

[1] *Institut f. Theor. Teilchenphysik, Universität Karlsruhe*
D–76131 Karlsruhe, Germany

[2] *Deutsches Elektronen-Synchrotron DESY*
D–22603 Hamburg, Germany

Contents

The search for the fundamental building blocks of matter and their interactions is the central objective of high energy physics. While the domain of light quark matter has well been explored in the past decades, heavy flavor physics has advanced very rapidly in recent years, but still poses a large number of important problems which can be solved in the years to come at existing and future colliders.

In the context of the Standard Model [1] three points are outstanding.

(i) The long awaited discovery of the top quark [2] which completes the fermionic spectrum of the Standard Model [SM], had been expected with certainty in the ongoing experiments at the Tevatron or the future proton colliders [see the preceding version of this report]. These theoretical predictions have been realized experimentally when the top quark was discovered at the Tevatron [3]. This is a triumph of quantum field theory and the high precision measurements of electroweak radiative corrections at LEP and in deep inelastic lepton–nucleon scattering [4] from which a value $m_t = 162 \pm 16 \pm 19$ GeV of the top quark mass could be derived before the particle was isolated in $p\overline{p}$ collisions. Future e^+e^- linear colliders [5] in the 350 GeV to 1 TeV c.m. energy range will provide a high precision determination of the top quark mass within a fraction of one GeV [6]. Anticipating the development of a flavor theory in the future, the demand of such high accuracy appears meaningful as the heavy top quark with a mass of the order of the electroweak symmetry breaking scale will play a key rôle among the fermions in such a theory. In the SM this is apparent from the large Yukawa coupling between the Higgs boson and the top quark, giving rise to sizeable indirect and direct effects in $t\bar{t}$ production.

(ii) A similarly fundamental problem is the embedding of $\mathcal{CP}$ violation in the Standard Model [7]. Being a rationale for the existence of three families [2], $\mathcal{CP}$ violation enters through the quark mixing in the weak interactions. While the information from the neutral $K - \overline{K}$ complex is nearly exhausted, the experimental investigation of $B^0 - \overline{B^0}$ mixing and of $\mathcal{CP}$ violation in the b quark sector allows for conclusive tests of the validity of this parametrization. Even though the Standard Model does not shed light on the physical origin of the $\mathcal{CP}$ asymmetry [in the same way as it does not predict the mass spectrum of quarks and leptons], it is nevertheless of utmost importance to prove experimentally that $\mathcal{CP}$ violation can be traced back to quark mixing. In particular, since in extended theories like supersymmetry additional $\mathcal{CP}$ violating mechanisms are operative.

(iii) It has already been possible to tag b quarks with high efficiency and purity in jet final states of high energy processes. They may therefore serve as a powerful instrument to discriminate quark jets from gluon jets, a necessary step to refine the exploration of QCD at short distances [8]. This method facilitates considerably the isolation of the three–gluon vertex, the measurement of gluon–jet properties and many other applications.

Heavy quarks are the fermionic particles closest to the magic TeV scale which is likely to be the energy threshold to a more profound theory, encompassing the Standard Model and resolving some of its enigmatic patterns. Mixing effects of order $m_i m_j / m_W^2$, too small to be observable in the light quark sector, may manifest themselves through flavor–changing neutral current processes between heavy quarks [9] and through rare heavy–meson decays [10].

This report is divided into two parts. In the first chapter we will summarize the conclusions which can be drawn from precision measurements of Z decays into b–quark pairs, the partial width and the forward–backward asymmetry [11]. The important subject of $\mathcal{CP}$-violation is adressed separately in an extensive report elsewhere in this book and it will not be treated in this article. In the second chapter the properties of top quarks in the Standard Model and beyond will be described, followed by a discussion of t production in high energy proton–(anti)proton [12] and e^+e^- colliders [13, 14].

Chapter 1

b QUARK

A substantial fraction of all Z decay modes are decays into bottom quarks. The branching ratio was predicted in the Standard Model to be close to

$$BR(Z \to b\bar{b}) \approx 15\%$$

so that approximately 3×10^6 bottom hadrons are produced in a sample of 10^7 Z decays. [A similarly large number of charm quarks has been produced, as expected from a branching ratio $BR(Z \to c\bar{c}) \approx 12\%$. However, for theoretical as well as experimental reasons we will concentrate on b quarks.]

Three different time steps can be distinguished in the evolution of the final state. The decay process $Z \to b\bar{b}$ is completed after a time of order $m_Z^{-1} \sim 10^{-3}$ fm,

including the most important genuine electroweak vertex corrections. Perturbative gluon radiation and non–perturbative fragmentation proceeds up to a time scale of $\gamma\Lambda_{QCD}^{-1} \sim 10$ fm in the lab frame. Given a lifetime of ~ 1 ps, the b–flavored hadrons travel to macroscopic distances of order $\gamma\tau_B \sim 3$ mm before they decay weakly.

The total number of b final states is sufficiently large to carry out precision measurements in the <u>*b quark sector*</u> [11]. Fundamental aspects of the Standard Model can be tested in the heavy quark sector by determining the vector and axial vector electroweak charges from cross sections and asymmetries. The accuracy of $\sin^2\vartheta_W$ which has been achieved by measuring the forward–backward asymmetry of b jets, is at the level of $\pm$ 0.001 and better, and thus competes well with other methods in the lepton sector. Moreover, vertex corrections due to the exchange of new particles predicted in theories beyond the Standard Model, affect the partial decay width of Z bosons to b quark pairs. Thus, these experiments allow for a glimpse at the physics beyond the standard or, at least, lead to interesting constraints.

QCD inspired fragmentation models developed to describe the hadronization of quarks and gluons in jets, can be scrutinized experimentally in Z decays to heavy–quark jets [11]. Because heavy quark pair creation in the jet evolution is strongly suppressed, the fragmentation of heavy quarks provides the most powerful tool to tackle this rather involved problem. The tagging of heavy quark jets will allow us to isolate clearly gluon jets in 3– and multi–jet final states so that their profile and their interactions can be explored.

The properties of *b hadrons* can be investigated experimentally in great detail [11, 15]. The high particle energies make feasible the measurement of individual lifetimes in vertex detectors. The mixing parameters in the B_d system can well be determined by analyzing the time evolution of the $B_d^0 - \overline{B}_d^0$ states. The oscillations in the $B_s^0 - \overline{B}_s^0$ system, however, are so rapid that, even though nearly complete mixing can easily be established by measuring time–integrated observables, a quantitative measurement of the mixing parameter appears very difficult, yet powerful lower bounds could already be established.

1.1 Electroweak properties of b quarks

1.1.1 Production of b quarks

The Z boson couples to quarks through vector and axial–vector charges with the well–known strength

$$= \sqrt{\frac{G_F m_Z^2}{2\sqrt{2}}}\gamma_\mu \left[v_q - a_q\gamma_5\right]$$

In the Standard Model these charges are defined as

$$\left.\begin{array}{lcl} v_q & = & 2I_q^{3L} - 4e_q \sin^2\vartheta_W \\ a_q & = & 2I_q^{3L} \end{array}\right\} \qquad 2I_q^{3L} = \pm 1 \qquad \text{for up/down particles}$$

For many applications the Born approximation provides an excellent representation of the partial Z decay rate

$$\Gamma_B(Z \to b\bar{b}) = \frac{G_F m_Z^3}{8\sqrt{2}\pi}\beta\left[\frac{3-\beta^2}{2}v_b^2 + \beta^2 a_b^2\right] \tag{1.1}$$

The mass dependence which enters through the velocity $\beta = \sqrt{1-\mu_b^2}$ $[\mu_b^2 = 4m_b^2/s]$ is $\mathcal{O}(\mu_b^2) = \mathcal{O}(10^{-2})$ in the axial term for b quarks; in the vector term the correction is of order $\mu_b^4 \sim 10^{-4}$ and thus of minor importance. Defining the strength of the Z coupling to $q\overline{q}$ by the Fermi μ decay constant G_F and the electroweak mixing angle through $\sin^2\vartheta_W = 1 - m_W^2/m_Z^2$ the *bulk* of radiative corrections to the width, i. e. the logarithmic corrections from the running of α_{QED}, are automatically incorporated.

QCD corrections to the width $\Gamma(Z \to q\overline{q}\ldots)$ are known for non-zero (but small) quark masses up to second order and for zero quark masses even up to third order in α_s (for a recent review see [16]). They are different for vector and axial–vector couplings not only because masses break chiral invariance but also due to the large mass splitting between bottom and top quarks. Decomposing the width into the vector and the axial–vector part we expand both parts separately in the strong coupling constant

$$\begin{aligned} \Gamma(Z \to q\overline{q} + \ldots) \quad = \quad & \Gamma_B^V \left[1 + c_1\left(\frac{\alpha_s}{\pi}\right) + c_2\left(\frac{\alpha_s}{\pi}\right)^2 + \cdots\right] \\ & + \Gamma_B^A \left[1 + d_1\left(\frac{\alpha_s}{\pi}\right) + d_2\left(\frac{\alpha_s}{\pi}\right)^2 + \cdots\right] \end{aligned} \tag{1.2}$$

The *vector* coefficients c_1, c_2, c_3 have been calculated for massless quarks. In the $\overline{MS}$ scheme one obtains [17, 18]

$$\begin{aligned} c_1 &= 1 \\ c_2 &= 1.9857 - 0.1153N_f = 1.4092 \\ c_3 &= -6.6368 - 1.2001N_f - 0.0052N_f^2 = -12.77 \end{aligned} \tag{1.3}$$

and

$$\frac{\alpha_s(s)}{\pi} = \frac{4}{\beta_0 L}\left[1 - \frac{1}{\beta_0 L}\frac{\beta_1 \ln L}{\beta_0} + \frac{1}{\beta_0^2 L^2}\left(\frac{\beta_1^2}{\beta_0^2}(\ln^2 L - \ln L - 1) + \frac{\beta_2}{\beta_0}\right)\right] \tag{1.4}$$

$$\beta_0 = 11 - \frac{2}{3}N_f, \qquad \beta_1 = 102 - \frac{38}{3}N_f, \qquad \beta_2 = \frac{2857}{2} - \frac{5033}{18}N_f + \frac{325}{54}N_f^2 \tag{1.5}$$

In the total hadronic decay rate one must include a contribution to c_3 which arises from 3 gluon intermediate states and hence corresponds to a flavor singlet configuration. This piece cannot be assigned easily to a specific flavor. For $\sin^2\vartheta_W = 0.23$ it amounts to

$$c_3(singlet) = -1.2395\frac{(\sum v_f)^2}{\sum 3v_f^2} = -0.405 \tag{1.6}$$

This small term, which affects the rate by less than $0.5 \cdot 10^{-4}$, indicates an inherent limit for flavor separation in Z decays. In fact, already in $O(\alpha_s^2)$ the separation of Γ_b

requires same care: b quarks may be produced from virtual gluons radiated off light quarks and hence are present in the $Z \to u\bar{u}$ or $d\bar{d}$ channel. However, these quarks are soft and can, therefore, be separated kinematically.
A similar discussion applies for the *axial* decay rate. For massless quarks d_1 and c_1 coincide

$$d_1 = 1$$

However, the coefficient d_2 deviates from c_2 even for massless quarks [19]. This is a consequence of the cut triangular diagrams exemplified below. Whereas vector couplings do not give a contribution because of C invariance, axial couplings do. This is due to the $4b$ final state in the last diagram and the mass difference between the top and the bottom quark in the first two diagrams. The large mass splitting between top and bottom breaks the symmetry in this weak isodoublet so that up and down contributions do not add up to zero any longer. In the $\overline{MS}$ renormalization scheme one finds for $N_F = 5$ flavors

$$d_2 \quad = \quad 1.41 \mp f_2(m_t) \qquad\qquad \mp \text{ for } q = \text{up/down} \tag{1.7}$$

$f_2(m_t)$ is well parametrized by

$$f_2(m_t) = 2\log\left(\frac{m_Z}{m_t}\right) - 3.083 + 0.346\left(\frac{m_Z}{2m_t}\right)^2 + 0.211\left(\frac{m_Z}{2m_t}\right)^4 \tag{1.8}$$

For a top quark mass of 175 ± 5 GeV the function $f_2(m_t)$ amounts to -4.34 ± 0.06.

Also d_3 differs from c_3. The leading logarithms as well as the constant parts in the additional term have been evaluated in [20] and [21] respectively:

$$f_3 = \frac{23}{12}\ln^2\frac{m_Z}{m_t} + \frac{67}{18}\ln\frac{m_Z}{m_t} - 15.99 \approx -17.6. \tag{1.9}$$

QCD corrections for arbitrary quark masses have been calculated up to first order [22, 23, 24] and recently even up to second order [25, 26] for vector and axial vector contributions. For the present purpose an expansion in $\mu_b = 2m_b/m_Z$ is adequate. The leading terms are given by

$$\begin{aligned} c_1 &= 1 + 3\mu_b^2 + \ldots \\ d_1 &= 1 + 3\mu_b^2\log(4/\mu_b^2) + \ldots \end{aligned} \tag{1.10}$$

The coefficient d_1 exceeds unity by ~ 0.20 for b quarks. The large logarithm of μ_b that arises in d_1 (and in $d_2, \ldots$ as well as in $c_2, \ldots$) can be absorbed in a redefined running b mass

$$\begin{aligned}\overline{m}(s) &= \overline{m}(\overline{m}^2)\Big(\frac{\alpha_s(s)}{\alpha_s(\overline{m}^2)}\Big)^{\gamma_0/\beta_0}\Big\{1+\Big(\frac{\gamma_1}{\beta_0}-\frac{\beta_1\gamma_0}{\beta_0^2}\Big)\Big(\frac{\alpha_s(s)}{4\pi}-\frac{\alpha_s(\overline{m}^2)}{4\pi}\Big) \\ &+\frac{1}{2}\Big[\Big(\frac{\gamma_1}{\beta_0}-\frac{\beta_1\gamma_0}{\beta_0^2}\Big)\Big(\frac{\alpha_s(s)}{4\pi}-\frac{\alpha_s(\overline{m}^2)}{4\pi}\Big)\Big]^2 \\ &+\frac{1}{2}\Big(\frac{\gamma_2}{\beta_0}+\frac{\beta_1^2\gamma_0}{\beta_0^3}-\frac{\beta_1\gamma_1}{\beta_0^2}-\frac{\beta_2\gamma_0}{\beta_0^2}\Big)\Big((\frac{\alpha_s(s)}{4\pi})^2-(\frac{\alpha_s(\overline{m}^2)}{4\pi})^2\Big)\Big\} \qquad (1.11)\end{aligned}$$

$$\gamma_0 = 4, \qquad \gamma_1 = \frac{202}{3} - \frac{20}{9}N_f, \qquad \gamma_2 = 1249 - (\frac{2216}{27} + \frac{160}{3}\zeta(3))N_f - \frac{140}{81}N_f^2$$

Recently even the four loop beta function β_3 [27] and anomalous mass dimension γ_3 [28] have been calculated. The "on-shell mass" m which appears in (1.10) and $\overline{m}(\overline{m}^2)$ are, for the b quark, related through [29]

$$m = \overline{m}(\overline{m}^2)\Big(1 + \frac{4}{3}\frac{\alpha_s(\overline{m}^2)}{\pi} + 9.6(\frac{\alpha_s(\overline{m}^2)}{\pi})^2\Big)$$

Evaluating higher order terms in α_s, but keeping only corrections of order m_b^2/m_Z^2 and summing logarithms of m_b^2/m_Z^2 one finds the following correction for the partial width [24, 16]

$$\begin{aligned}\Gamma(Z\to b\bar{b}+\ldots) &= \Gamma_b^V\Big|_{m_b=0}\Big[1+\frac{\alpha_s}{\pi}+1.41(\frac{\alpha_s}{\pi})^2-12.77(\frac{\alpha_s}{\pi})^3+\ldots \\ &\qquad +12\frac{\overline{m}^2(m_Z^2)}{m_Z^2}\Big(\frac{\alpha_s}{\pi}+8.7(\frac{\alpha_s}{\pi})^2+45(\frac{\alpha_s}{\pi})^3+\ldots\Big)\Big] \\ &+\Gamma_b^A\Big|_{m_b=0}\Big[1+\frac{\alpha_s}{\pi}+\Big(1.41+f(m_t)\Big)(\frac{\alpha_s}{\pi})^2-12.77(\frac{\alpha_s}{\pi})^3+\ldots \\ &\qquad -6\frac{\overline{m}^2(m_Z^2)}{m_Z^2}\Big(1+\frac{11}{3}\frac{\alpha_s}{\pi}+(11.3+\ln\frac{m_Z^2}{m_t^2})(\frac{\alpha_s}{\pi})^2+\ldots\Big)\Big] \qquad (1.12)\end{aligned}$$

The tiny QED corrections to the width $\delta\Gamma^{QED}/\Gamma^{QED} = (1 + \frac{3}{4}e_q^2\frac{\alpha}{\pi})$, being 0.017% for down and 0.068% for up quarks, are included in Γ^V and Γ^A, as well as the electroweak corrections.

A quantity of considerable practical interest is the ratio Γ_b/Γ_{had}. The bulk of QCD corrections cancels in this ratio and one finds [16]

$$\frac{\Gamma(Z\to b\bar{b}+\ldots)}{\Gamma(Z\to had)} \approx \frac{\Gamma_b}{\sum_q\Gamma_q}\Big|_{m_b=0}\left\{1-0.0031-0.005\frac{\alpha_s}{\pi}-2.3\left(\frac{\alpha_s}{\pi}\right)^2-6.9\left(\frac{\alpha_s}{\pi}\right)^3\right\}. \qquad (1.13)$$

The error in the leading coefficient from the uncertainty in the bottom mass amounts to $3 \cdot 10^{-4}$ and is thus neglibible for all practical purposes. For $m_b = 4.7$ GeV and $\alpha_s = 0.12$ corresponding to $\overline{m}_b(m_Z^2) = 2.77$ GeV the overall correction factor yields $(1 - 0.7 \cdot 10^{-3})$. At this point we should reiterate that b quarks can be produced also through virtual gluons radiated off light quarks. These final states may be interpreted as part of the Z decay rate into light quarks and treated in this context. The b energy spectrum is particularly soft. These events must be subtracted if one aims at an experimental determination of $\Gamma_{b\bar{b}}$ as calculated in the electroweak theory.

The relative rate for this "secondary" b and c quark production amounts to $\approx 2 \cdot 10^{-3}$ and $(1-2) \cdot 10^{-2}$ [30].

Being proportional to the square of α_s, the result is quite sensitive to the choice of α_s and, furthermore, to the mass of the bottom quark. These predictions are in fair agreement with the experimental results $\overline{n}(g \to c\bar{c}) = (2.27 \pm 0.28 \pm 0.41) \cdot 10^{-2}$ [31] and $\overline{n}(g \to b\bar{b}) = (2.10 \pm 1.1 \pm 0.09) \cdot 10^{-3}$ [32].

Genuine electroweak corrections [33]–[34], on the other hand, become sizeable for a large top mass $m_t \simeq 175$ GeV. They are also sensitive to the value of the Higgs mass. Two categories can be distinguished[1].

(i) The universal electroweak corrections are built–up by loop corrections to the W,Z propagators and γ–Z mixing. They induce a universal shift of the Fermi coupling and the electroweak mixing angle

$$\begin{aligned} G_F &\to G_{eff} = G_F(1+\Delta\rho) \\ \sin^2\vartheta_W &\to \sin^2\theta_{eff} = \sin^2\vartheta_W[1+\Delta\kappa_{SE}] \end{aligned} \tag{1.14}$$

The leading contributions to the Veltman parameter [36] $\Delta\rho$ and to $\Delta\kappa_{SE}$ are due to $(b\bar{b}), (t\bar{b})$ and $(t\bar{t})$ loops,

$$\begin{aligned} \Delta\rho_t &= \frac{3\sqrt{2}G_F m_t^2}{16\pi^2} + \cdots \\ \Delta\kappa_{SE} &= \cot^2\theta_W \Delta\rho + \text{subleading } t \text{ and } H \text{ contributions} \end{aligned} \tag{1.15}$$

The electroweak mixing angle is related to the electric and weak coupling constants in the usual way

$$m_Z^2 \cos^2\theta_W \sin^2\vartheta_W = \frac{\pi\alpha(m_Z^2)}{\sqrt{2}G_F(1+cot^2\theta_W\Delta\rho_t)} \tag{1.16}$$

with the running electric charge $\alpha(m_Z^2) = 1/128.896...$ [37] and subleading top and Higgs contributions again neglected.

[1]The on–shell renormalization scheme with $\sin^2\vartheta_W \equiv 1 - m_W^2/m_Z^2$ will be adopted in the following discussion.

(ii) Of particular interest are the electroweak vertex corrections for b–quark final states because they involve the exchange of virtual top quarks. These diagrams alter the vector and axial–vector charge of b quarks by the same amount

$$\begin{aligned} v_f &\rightarrow v_{eff} = v_f + \delta_b \frac{2}{3}\Delta\rho \qquad (1.17) \\ a_f &\rightarrow a_{eff} = a_f + \delta_b \frac{2}{3}\Delta\rho \end{aligned}$$

where subleading t contributions have been suppressed again.

In view of the high precision reached in the LEP experiments, even the calculation of mixed QCD-electroweak corrections has become necessary. The top contributions to the ρ parameter and Δr have been calculated in order $G_F m_t^2 \alpha_s$ [38, 39] and the three–loop results of order $G_F m_t^2 \alpha_s^2$ are now available [40, 41]. This leads to an overall shift in m_t of roughly 10 GeV, which should be compared with the current experimental error in precision measurements of 7 GeV. To interprete correctly the precise determination of R_b in the context of the SM (or its SUSY extensions), the mixed QCD-electroweak corrections to the $Zb\bar{b}$ vertex must be included. The leading terms of order $G_F m_t^2 \alpha_s$ and $G_F \alpha_s \ln(m_t^2/m_Z^2)$ have been obtained in Ref. [42]. Non-enhanced corrections of order $G_F \alpha_s m_Z^2$ are presently available for light flavour final states only [43].

Utilizing effective couplings, $G_{eff}, \sin^2\theta_{eff}$ and v_{eff}, a_{eff}, in the Born expression for the partial width $\Gamma(Z \to b\bar{b})$ in eq.(1) and the forward–backward asymmetry to be discussed later, the dominant electroweak corrections are incorporated in a compact and elegant form.

The b partial width of the Z boson including all QCD, QED and genuine electroweak corrections may then be summarized as

$$\begin{aligned} \Gamma(Z \to b\bar{b} + \cdots)\Big|_{m_b=0} &= \Gamma_B^V(G_{eff}, v_{eff})\Big|_{m_b=0} \left[1 + \frac{3}{4}\frac{e_b^2\alpha}{\pi}\right]\left[1 + c_1\left(\frac{\alpha_s}{\pi}\right) + \cdots\right] \\ &\quad + \Gamma_B^A(G_{eff}, a_{eff})\Big|_{m_b=0} \left[1 + \frac{3}{4}\frac{e_b^2\alpha}{\pi}\right]\left[1 + d_1\left(\frac{\alpha_s}{\pi}\right) + \cdots\right] \end{aligned}$$

The partial widths including all these corrections are given for b decays by

$$\Gamma(Z \to b\bar{b} + \ldots)/\Gamma_{had} = 0.2157 \pm 0.0003 \qquad (1.18)$$

and for c decays by

$$\Gamma(Z \to c\bar{c} + \ldots)/\Gamma_{had} = 0.1724 \pm 0.0001 \qquad (1.19)$$

	TAG	$BR(Z \to b\bar{b})$	TAG	$BR(Z \to c\bar{c})$
Aleph	multi	0.2156 (9)(11)	$D^{*\pm}$	0.1724 (98)(100)
			lepton	0.1649 (70)(106)
Delphi	multi	0.2202 (14)(17)	c_count $\oplus D^{*\pm}$	0.1692 (80)(83)
L3	lifetime	0.2185 (28)(32)		
Opal	multi	0.2175 (14)(15)	c_count	0.1670 (110)(120)
SLD	multi	0.2149 (34)(16)		
Average		0.2177 ± 0.0011		0.1722 ± 0.0053
Standard Model		0.2158 ± 0.0003		0.1723 ± 0.0001

Table 1.1: *Excerpts of experimental results; for a comprehensive summary see [44]. Measurements are quoted for bb only if the stat/syst errors are less than (40)(40), for cc if less than (120)(120).*

These values, derived within the Standard Model, are based on $\sin^2 \vartheta_w^{l,eff} = 0.2317 \pm 0.0003$ and a top mass of 175 ± 6 GeV in the higher–order corrections.

The experimental results for Z decays to b quarks and c quarks are collected in Table 1.1 for the four LEP experiments Aleph, Delphi, L3 and Opal, and the SLC experiment SLD. The world average of the b decay branching ratio agrees with the theoretical prediction within less than two standard deviations. While the Aleph results match the theoretical prediction almost perfectly, the slight positive deviation in the overall picture leaves room for small contributions from areas beyond the Standard Model, *notabene* supersymmetric theories. However, supersymmetric theories do not necessarily lead to deviations from the Standard Model which could be detected within the present experimental accuracy.

The close agreement of the experimental data with the predictions of the Standard Model allows us to draw interesting physical conclusions.

(i) The weak isospin of the left– and right–handed bottom quarks are, respectively,

$$\begin{aligned} I_3(b_L) &= -1/2 \\ I_3(b_R) &= 0 \end{aligned}$$

A topless model with $I(b) = 0$ would have been in gross disagreement with the Z decay width to b quarks

$$\frac{\Gamma(b\bar{b})^{topless}}{\Gamma(b\bar{b})^{SM}} = \frac{\left(4e_b \sin^2\vartheta_W\right)^2}{\left(1 + 4e_b \sin^2\vartheta_W\right)^2 + 1} \approx \frac{1}{13} \tag{1.20}$$

(ii) The universal electroweak corrections can be eliminated from a combination of Z decay observables and the specific b vertex corrections [45] can be isolated in this way:

$$\begin{aligned} T &= \frac{3}{59}\frac{\Gamma_{had}}{\Gamma_l} - \frac{30}{59}\frac{9}{\alpha(m_Z^2)}\frac{\Gamma_l}{m_Z} \\ &\propto 1 + \Delta_V^b \end{aligned} \tag{1.21}$$

The *SM* top contribution to $\Delta_V^b = -\frac{20}{19}\frac{\alpha}{\pi}\frac{m_t^2}{m_Z^2} - \cdots$ is negative for $m_t > m_Z$. And so are vertex corrections in the minimal supersymmetric extension of the Standard Model. Z mixing with new E(6) type Z' bosons, on the other hand, may either lower or raise the vertex correction Δ_V^b relative to the Standard Model. The same conclusion applies for vertex corrections in a general two–Higgs doublet model with large $\tan\beta = v_2/v_1$, if the masses of scalar (m_1, m_2) and pseudoscalar (m_3) Higgs bosons are not too large [46].

1.1.2 Forward–backward asymmetry

For quarks tagged at an angle ϑ the differential production cross section $e^+e^- \to b + \ldots$ is a binomial in $\cos\vartheta$

$$\frac{d\sigma}{d\cos\vartheta} = \frac{3}{8}(1+\cos^2\vartheta)\sigma_U + \frac{3}{4}\sin^2\vartheta\sigma_L + \frac{3}{4}\cos\vartheta\sigma_F \tag{1.22}$$

U and L denote the contributions of unpolarized and longitudinally polarized gauge bosons along the ϑ-axis, and F denotes the difference between right and left polarizations. The total cross section is the sum of U and L,

$$\sigma = \sigma_U + \sigma_L \tag{1.23}$$

The forward-backward asymmetry for a fixed angle ϑ vs. $\pi - \vartheta$ can be cast into the form

$$A^{FB}(\vartheta) = \frac{2\cos\vartheta}{1 + \alpha_Q\cos^2\vartheta}\beta_Q \tag{1.24}$$

with the parameters

$$\alpha_Q = \frac{\sigma_U - 2\sigma_L}{\sigma_U + 2\sigma_L} \qquad \beta_Q = \frac{\sigma_F}{\sigma_U + 2\sigma_L} \tag{1.25}$$

If only a limited angular range $|\cos\vartheta| \le x$ is covered, the integrated asymmetry is modified to

$$A_{FB}(|\cos\vartheta| \le x) = \frac{3}{4}\frac{x\sigma_F}{\sigma_U + \sigma_L - (1-x^2)(\sigma_U - 2\sigma_L)/4} \tag{1.26}$$

Including the full angular range this simplifies to

$$A^{FB} = \frac{3}{4}\frac{\sigma_F}{\sigma} \tag{1.27}$$

The σ^i can be expressed in terms of the cross sections for the massless case ($\mu = 0$); in Born approximation,

$$\begin{aligned} \sigma_B^U &= \beta\sigma^{VV} + \beta^3\sigma^{AA} \\ \sigma_B^L &= \frac{1}{2}(1-\beta^2)\beta\sigma^{VV} \\ \sigma_B^F &= \beta^2\sigma^{VA} \end{aligned} \tag{1.28}$$

with

$$\begin{aligned} \sigma^{VV} &= \frac{4\pi\alpha^2(m_Z^2)e_e^2e_Q^2}{s} + \frac{G_F\alpha(m_Z^2)}{\sqrt{2}}e_e e_Q v_e v_Q \frac{m_Z^2(s-m_Z^2)}{(s-m_Z^2)^2 + (\frac{s}{m_Z}\Gamma_Z)^2} \\ &\quad + \frac{G_F^2}{32\pi}(v_e^2 + a_e^2)v_Q^2 \frac{m_Z^4 s}{(s-m_Z^2)^2 + (\frac{s}{m_Z}\Gamma_Z)^2} \\ \sigma^{AA} &= \frac{G_F^2}{32\pi}(v_e^2 + \alpha_e^2)a_Q^2 \frac{m_Z^4 s}{(s-m_Z^2)^2 + (\frac{s}{m_Z}\Gamma_Z)^2} \\ \sigma^{VA} &= \frac{G_F\alpha(m_Z^2)}{\sqrt{2}}e_e e_Q a_e a_Q \frac{m_Z^2(s-m_Z^2)}{(s-m_Z^2)^2 + (\frac{s}{m_Z}\Gamma_Z)^2} \\ &\quad + \frac{G_F^2}{8\pi}v_e v_Q a_e a_Q \frac{m_Z^4 s}{(s-m_Z^2)^2 + (\frac{s}{m_z}\Gamma_Z)^2} \end{aligned} \tag{1.29}$$

On top of the Z resonance the asymmetry is dominated by the Z amplitude, so that to a very good approximation

$$\begin{aligned} A_B^{FB} &= \frac{3}{4}\frac{2v_e a_e}{v_e^2 + a_e^2}\frac{2v_Q a_Q \beta}{v_Q^2(3-\beta^2)/2 + a_Q^2\beta^2} \\ &\approx \frac{3}{4}\frac{2v_e a_e}{v_e^2 + a_e^2}\frac{2v_Q v_Q}{v_Q^2 + a_Q^2} \end{aligned} \tag{1.30}$$

As a consequence of an accidental cancellation among the couplings ($v_b^2 \approx a_b^2/2$), the mass correction $\simeq \mu^2(-v_Q^2 + a_Q^2/2)/(v_Q^2 + a_Q^2)$ is strongly suppressed to $\mathcal{O}(10^{-4})$.

The first factor,

$$P_{long} = -2v_e a_e/(v_e^2 + a_e^2)$$

measures the degree of Z polarization along the e^- axis while the same factor for the b quarks describes their analysing power.

In the neighborhood of the Z peak the variation of the asymmetry is approximately linear in the energy

$$A_{FB}(\sqrt{s}) - A_{FB}(m_Z) = \frac{8\pi\alpha\sqrt{2}}{G_\mu m_Z^2} A_{FB}(m_Z)\left(\frac{e_e e_Q}{v_e v_Q} - \frac{e_e e_Q}{a_e a_Q}\frac{4}{3}A_{FB}\right)\frac{\sqrt{s}-m_Z}{m_Z} \quad (1.31)$$

$$\approx 8.6\frac{|e_Q|}{v_Q^2+1}\frac{\sqrt{s}-m_Z}{m_Z} = \frac{\sqrt{s}-m_Z}{m_Z}\begin{cases} 8.6 & \text{for muons} \\ 5.0 & \text{for charmed quarks} \\ 1.9 & \text{for bottom quarks}\end{cases}$$

$$A^{FB}(b) = \frac{3}{4}\frac{2v_e a_e}{v_e^2 + a_e^2}\frac{2v_b a_b}{v_b^2 + a_b^2} \quad (1.32)$$

As a result of the general discussion in the preceding section, the vector charges v_e and v_b are defined by their respective effective mixing angles $\sin^2\vartheta_W^{eff}$ in eq. (12,15), thus incorporating the leading m_t dependent electroweak corrections in the asymmetry.

Once QCD and QED corrections are included, a careful definition of the scattering angle is necessary. Two different definitions appropriate for heavy quark production have been used:

(1) b quark direction: $e^+e^- \to b(\vartheta_b) + \ldots$ (2) thrust axis: $e^+e^- \to j_b(\vartheta_T) + j$

QCD corrections to the cross section and A_{FB}, based on the first definition, have been calculated in [23]. For small μ the formulae simplify considerably. On top of the Z, the corrections to the various terms can be cast into the form

$$\sigma_i = \sigma_i^0\left(1 + c_i\frac{\alpha_s}{\pi}\right) \quad (1.33)$$

with [34, 35]

$$\begin{aligned} c_F &= \frac{8}{3}\mu + \frac{\mu^2}{3}\left(7 + \frac{\pi^2}{6} + \log\frac{4}{\mu^2} + \frac{1}{4}\log^2\frac{4}{\mu^2}\right) + \ldots \approx 0.367 \\ c_V &= 1 + 3\mu^2 + \ldots \approx 1.033 \\ c_A &= 1 + 3\mu^2\log\frac{4}{\mu^2} + \ldots \approx 1.196 \end{aligned} \quad (1.34)$$

(numerical values for $\mu = 2 \times 4.8\ GeV/91\ GeV$). After introducing the running quark mass in the Born and $\mathcal{O}(\alpha_s)$ expressions, the large logarithm in C_A is absorbed (see eq. 1.10). A similar study for c_F has not been performed so far. Note that c_F vanishes in the zero-mass limit. The correction to A_{FB} on top of the resonance then reads

$$A_0^{FB} \to A^{FB} \approx A_0^{FB}\left(1 - \frac{\alpha_s}{\pi}\left(1 - c_F + 3\mu^2 \frac{v_Q^2 + a_Q^2 \log \frac{4}{\mu^2}}{v_Q^2 + a_Q^2}\right)\right) \tag{1.35}$$

with the leading part of the correction due to the change of the normalization. The dominant effect is thus a reduction of the asymmetry by about 4% through a factor $(1 - \frac{\alpha_s}{\pi})$ for $\mu^2 = 0$; mass corrections lower the the coefficient of $\frac{\alpha_s}{\pi}$ from 1 to about 0.8. If ϑ_b is not summed over, corrections are needed for the vector and axial-vector parts of the U and L terms separately and can be found in [34]. Analytical results for QCD corrections, including quark mass effects and a cut on the gluon energy, can be deduced from [47].

Table 1.2: *QCD corrections to forward–backward asymmetries of b quarks in 2–jet events [34] .*

y	k_A
0.02	-0.05
0.04	-0.14
0.08	-0.34

Similar results are obtained if the thrust axis is chosen as the reference axis. If the jet masses are bounded to values below $m_j^2 \leq y m_Z^2$, the QCD correction in 2–jet events

$$A^{FB}(2\text{–jet}) = A^{FB}(b)\left[1 + k_A\left(\frac{\alpha_s}{\pi}\right)\right] \tag{1.36}$$

remains small, Table 1.2. This is intuitively expected as infrared and collinear gluon bremsstrahlung leave the b–quark direction nearly unaffected.

The impact of QED corrections on A_{FB} for $b\bar{b}$ final states is small for loose cuts on the photon energy and angle.

Final state radiation is treated in complete analogy to gluon radiation. Defining the scattering angle through the direction of the b quark (as adopted above) the asymmetry is reduced by a factor $(1 + \frac{3}{4}Q_b^2\frac{\alpha}{\pi})^{-1}$ through the increase in the overall normalization, an effect completely negligible.

Analytical results for the influence of the interference between γ-emission from the initial and final states can be found in [48], [12] for the μ-pair final states. Although two different definitions of the scattering angle are adopted, for loose cuts the effect is found to be negligible, just as for the total cross section [49]. Around the Z peak the corrections are of relative order $< \frac{\alpha}{\pi}(\Gamma_Z/m_Z)$.

The influence of initial state radiation is strongly dependent on the energy. It is modest below and on top of the Z peak. A full treatment, including the impact on the kinematics and the change of the effective energy can only be performed in a Monte Carlo calculation. Formulae have been developed for the μ-pair asymmetry, which are based on the approximation of collinear radiation; they are accurate to better than 0.3×10^{-2} and can easily be improved to include also multiple photon emission. Without any cut on the photon energy [50, 51] (see also [48])

$$\langle A_{FB} \rangle = \frac{3}{4} \frac{\int_0^1 dz F(s,z)(\frac{1-z}{1+z})^2 \sigma_F(sz)}{\int_0^1 dz F(s,z) \sigma(sz)} \tag{1.37}$$

To $\mathcal{O}(\alpha)$, the distribution $F(s, z)$ is given by the Bonneau-Martin formula, to $\mathcal{O}(\alpha^2)$ – including exponentiation – $F(s, z)$ is given in [52]. For $\sqrt{s}$ about 200 MeV above m_Z the corrected asymmetry coincides with $A_0^{FB}(m_Z)$. A simple analytical calculation gives $\delta W = \alpha(\ln(s/m_e^2) - 1)\Gamma_Z)/2 = 217\ MeV$ for this shift. Conversely it is clear from eq. (28) that the asymmetry for $\sqrt{s} = m_Z$ is lowered by

$$\delta A|_{QED} = 8.6 \frac{|e_Q|}{v_Q^2 + 1} \frac{\delta W}{m_Z} = \begin{cases} 0.46 \times 10^{-2} & \text{for bottom quarks} \\ 1.2 \times 10^{-2} & \text{for charmed quarks} \end{cases}$$

Mixing. Forward–backward asymmetries of quarks are extracted by measuring the asymmetries of mesons and baryons endowed with this particular quark flavor. For b quarks this is not a one–to–one correspondence due to mixing in the neutral B_d^0 and B_s^0 systems [53]. Because associate production of $b\overline{b}$ pairs in the jet development, perturbative as well as non–perturbative, can safely be neglected, the hadronic asymmetries are related to the asymmetry of the primarily produced b quarks in the following way.

(i) *b tagging through* B_u^-, Λ_b:

$$A^{FB}(B_u^-, \Lambda_b) = A^{FB}(b) \tag{1.38}$$

(ii) *b tagging through* $\overline{B}_d^0$ or $\overline{B}_s^0$:

These particles mix with their partners $\overline{B}_d^0 \leftrightarrow B_d^0$ and $\overline{B}_s^0 \leftrightarrow B_s^0$ so that the b flavor is changed at a rate comparable or much more frequent than the decay rate for $\overline{B}_d^0$ and $\overline{B}_s^0$, respectively. Denoting the time–integrated probability by χ_q for observing a B_q^0 particle in a beam of originally produced $\overline{B}_q^0$ particles, these parameters have been determined in time–integrated and time–dependent measurements (see Sect. 1.5.2), for B_d^0: $\chi_d = 0.174 \pm 0.006$, or are bounded strongly by the Standard Model and experimentally very close to 1/2 for B_s^0. Mixing reduces the observed asymmetry so that

$$A^{FB}(\overline{B}_q^0) = (1 - 2\chi_q) A^{FB}(b) \tag{1.39}$$

While the impact of B_d mixing is already quite noticeable $\sim 35\%$, the asymmetry in the B_s system is almost completely washed out.

(iii) *b tagging through* l^-:

Denoting the probability to find a $\overline{b}$ quark in a b beam by $\overline{\chi}$, a weighted mixture of B_d and B_s mixing parameters, this probability is directly measurable in the like–sign dilepton rate,

$$R_{ll} = \frac{l^{\pm}l^{\pm}}{\text{all } ll} = 2\overline{\chi}(1-\overline{\chi}) \tag{1.40}$$

With $\overline{\chi} = 0.126 \pm 0.008$ [54] the ensuing lepton asymmetry

$$A^{FB}(l^-) = (1-2\overline{\chi})A^{FB}(b) \tag{1.41}$$

is reduced to $\sim 75\%$ of the original b quark asymmetry .

The forward–backward asymmetry of b–quarks is highly sensitive to the precise value of the electroweak mixing angle $\sin^2\vartheta_W$. This follows from the fact that the term

$$P_{long}(b) = -2v_b a_b/(v_b^2 + a_b^2) \approx -0.93$$

in the asymmetry is close to its maximum and almost constant so that $A^{FB}(b) \approx -\frac{3}{4}P_{long}$ nearly coincides with the degree of the Z polarization and the corresponding LR asymmetry. This asymmetry is well known to be strongly dependent on $\sin^2\vartheta_W$ because $2v_e a_e/(v_e^2 + a_e^2) \sim 2(1-4\sin^2\vartheta_W)$ falls steeply near $\sin^2\vartheta_W \sim 1/4$. Let us assume, for example, that b quarks are tagged through the semileptonic decays of B mesons, then

$$A_{FB}(l^-) = A_{FB}(b)\left[1-2\overline{\chi}\right]\left[1-\kappa\frac{\alpha_s}{\pi}\right] \tag{1.42}$$

For $\overline{\chi} = 0.15$ and $\kappa\frac{\alpha_s}{\pi} = 0.03$ this leads to a sensitivity of

$$\delta\sin^2\vartheta_W = \delta A_{FB}(l^-)/3.8 \quad .$$

Because the error migrating from the mixing parameter $\overline{\chi}$ to A_{FB} is proportional to the asymmetry itself, its impact is small. An error of $\delta\sin^2\vartheta_W \sim 0.0004$ has been achieved so far, so that this method competes well with other measurements of $\sin^2\vartheta_W$ in the purely leptonic μ and τ sectors. The FB asymmetry of b quarks measured at LEP [44], $A_{FB}^b = 0.0979 \pm 0.0022$, is smaller than the expectation in the Standard Model, i.e. 01017. This gives rise to a slightly larger value of the electroweak mixing angle compared to the LEP + SLC average of $\sin^2\vartheta_{eff}^{lep} = 0.23153 \pm 0.00023$. The SLC value of the LR/FB asymmetry ($A^b = 0.897 \pm 0.047$) coincides with the *SM* prediction ($= 0.934$), albeit with larger error due to the reduced statistics. The evolution of the asymmetry from PETRA/PEP energies via TRISTAN to LEP/SLC is illustrated in Fig. 1.1.

1.1.3 Final State Polarization

Due to the parity violation of the electroweak interactions, quarks are produced with non-zero polarization in e^+e^-annihilation. For "light" heavy flavours (c, b), only the longitudinal component along the flight direction is sufficiently large [56] to be accessible experimentally, while transverse and perpendicular components are suppressed

Figure 1.1: *Comparison of the Standard Model prediction for the forward-backward asymmetry of b quarks with data; full line: b asymmetry, broken line: observed ℓ^- asymmetry including mixing effects. (Adopted from [55].)*

$\sim m_Q/m_Z$. For $\sqrt{s} = m_Z$ and neglecting non-zero-mass corrections the variation of the longitudinal polarization with the scattering angle ϑ is given by

$$P_L(\vartheta) = -\frac{\lambda_Q(1+\cos^2\vartheta) + \lambda_e \cdot 2\cos\vartheta}{(1+\cos^2\vartheta) + \lambda_e\lambda_Q\cos\vartheta} \tag{1.43}$$

where $\lambda_Q = 2v_Q a_Q/(v_Q^2 + a_Q^2)$ etc. Because the Z vector coupling to electrons is small, the variation with ϑ is moderate and, in contrast to the τ polarization, the average value ($\sin^2\theta_W = 0.23$)

$$P_L = -\lambda_Q = \begin{cases} -0.68 & \text{for charm} \\ -0.94 & \text{for bottom} \end{cases}$$

provides an adequate approximation. Thus the longitudinal quark polarizations are almost maximal.

The observable polarization is strongly affected by the hadronization. Assuming 100% longitudinal quark polarization, one expects *vector and pseudoscalar mesons* to be produced with the relative proportion 50:25:0:25 for the different spin configurations $[S, S_z] = [1,1] : [1,0] : [1,-1] : [0,0]$. Similar relations could be derived for baryons. Experimentally little is known about the spin transfer in hard reactions.

A variety of decay modes have been investigated to measure the baryon polarization, in particular for Λ_c and Λ_b. The semileptonic $\Lambda_c \to \Lambda \ell^+ \nu_\ell$ decay [57] as well as the nonleptonic decays [58] appear to be promising candidates. The polarization of Λ_b can be studied in particular through an analysis of the neutrino energy spectrum or its moments [59].

Besides the parity-violating polarization itself, spin-spin correlations between quarks and antiquarks have been studied. The formalism is somewhat involved and we refer to the original papers [56, 60] for details.

1.2 Fragmentation

The fragmentation of quarks into hadrons can qualitatively be deduced from QCD, yet a rigorous quantitative understanding is still lacking due to its complex nature. The intertwining of perturbative and nonperturbative mechanisms has therefore been formulated in algorithmic models. The gross characteristics of hadron (energy) distributions are adequately described in the independent jet fragmentation model [61]–[62]. This model is based on just one general assumption: that quark–gluon configurations in the femto–universe transform into jets, bunches of hadrons with small relative transverse momenta, at large distances. Not relying on unproven theoretical hypotheses, the model provided a solid base for establishing experimentally the existence of gluon jets. Picturing the basic jet structures sufficiently well, the model is too crude though to account properly for the small particle flow between the jets. Two different approaches have been pursued which refine this picture. Non–perturbative strong forces are the driving forces in the string picture [63], an approximation to the color flux tube stretched between quarks in QCD. Perturbative gluon bremsstrahlung, on the other hand, is considered to be the main mechanism for building–up jets in parton shower models [64]. Even though a mixture of both elements is responsible for the jet development as a whole, it remains an important physical problem to explore the dynamical driving mechanism of the jet formation. Heavy quark jets are the simplest systems to study the hadronization mechanism because spontaneous heavy quark–pair production is suppressed in the jet evolution.

Since the non–perturbative binding of a heavy quark Q into a hadron $(Q\overline{q})$ is the final step after the perturbative radiation of gluons, the fragmentation function

$$D(z) = \int_z^1 \frac{d\xi}{\xi} d_{NP}(z/\xi) d_{PT}(\xi) \tag{1.44}$$

is built–up by the convolution of the non–perturbative fragmentation function d_{NP} with the perturbative fragmentation function d_{PT}. ξ is the fraction of energy [in units of the initial energy] residing in the quark Q after the early perturbative gluon radiation, z the fraction of energy in the Q flavored hadron. The average energy fraction $\langle z \rangle$ is the product of the energy fraction $\langle z \rangle_{PT}$ after gluon radiation and the fraction $\langle z\rangle_{NP}$ transferred from the quark to the hadron non–perturbatively,

$$\langle z\rangle = \langle z\rangle_{NP}\langle z\rangle_{PT} \tag{1.45}$$

Both mechanisms are described in the next two subsections.

In contrast to light quarks, heavy quark fragmentation is hard because of the inertia of heavy quarks. The energy transfer by soft non–perturbative hadronization is small, and similarly for perturbative gluon radiation as long as $\log E/\log m_Q \not\gg 1$.

1.2.1 Gluon bremsstrahlung

Perturbative radiation is described by the non–singlet Altarelli–Parisi equation [65], the solution of which leads to an energy fraction

$$\langle z\rangle_{PT} = \left[\frac{\alpha_s(E^2)}{\alpha_s(m_Q^2)}\right]^{\frac{32}{3(33-2N_f)}} \tag{1.46}$$

left for the heavy quark after the perturbative gluon radiation [66]. For $E = m_Z/2$ in Z decays, the b quark looses about 20% of its initial energy to perturbative gluons. In next–to–leading order perturbation theory, the perturbative fragmentation function $d_{PT}(z)$ has a sharp maximum [67] just below 1 so that the fragmentation function vanishes at the boundary as a result of repeated infrared radiation, Fig.1.2.

Perturbative gluon radiation alone is insufficient to account for the spectrum of b mesons as measured at LEP, $\langle z\rangle_B = 0.705 \pm 0.011$ (to be compared with $\langle z\rangle_D = 0.5088 \pm 0.015$) [68]. Furthermore, with a probability of a few percent, events without radiation are predicted which require non–perturbative mechanisms to bridge the color gap between quarks and antiquarks in the final state. This is evident in particular for heavy quarks where perturbative gluon radiation

$$dN_g = \frac{4\alpha_s}{3\pi}\frac{\vartheta^2 d\vartheta^2}{[\vartheta^2 + (m_Q/E)^2]^2} \tag{1.47}$$

is concentrated on the surface of a cone about the Q direction with half–aperture $\vartheta_c = m_Q/E$ [$\sim 6^o$ for b quarks at LEP] while the interior is depleted from gluons.

1.2.2 Non–perturbative fragmentation

In contrast to light–quark hadronization the fragmentation of heavy quarks is hard [69]–[70] because the inertia carried by the heavy quarks is retained in the heavy–flavour hadrons. This can most transparently be proven by analyzing the hadronization $Q \to (Q\overline{q}) + q$ in the rest frame of the heavy quark Q. In this frame the left–over

Figure 1.2: *Shape of the perturbative b fragmentation function [67].*

Figure 1.3: *Momentum distribution of the hadrons produced in* $e^+e^- \rightarrow \overline{Q}Q$*, viewed in the* e^+e^- *center–of–mass frame; from [69].*

light–quark q is endowed only with little energy $\sim m_q^{eff}$ so that, when boosting the particles back to the e^+e^- c.m. frame with the γ factor $\gamma = \sqrt{s}/2m_Q$, q develops a light quark jet of energy $E_q \sim \gamma m_q^{eff} \sim \sqrt{s}/2m_Q \times$ GeV. The average [scaled] energy to the heavy hadron $(Q\overline{q})$ is therefore expected to be

$$\langle z \rangle_{NP} \sim 1 - \Lambda_{\text{QCD}}/m_Q \tag{1.48}$$

The ensuing particle distribution is depicted in Fig.1.3. Several detailed forms have been elaborated to parametrize the shape of the fragmentation functions.

Peterson et al. form [70]

The transition amplitude for a fast moving quark Q fragmenting into $(Q\overline{q}) + q$ is proportional to the inverse of the energy transfer ΔE^{-1}. Denoting by z the fraction of energy ($\approx$ momentum) retained in the heavy meson, it follows that

$$\begin{aligned}
\Delta E &= \sqrt{m_Q^2 + P^2} - \sqrt{m_H^2 + (zP)^2} \\
&\quad - \sqrt{m_q^2 + [(1-z)P]^2} \\
&\sim 1 - \frac{1}{z} - \frac{\varepsilon_Q}{1-z}
\end{aligned}$$

The parameter ϵ_Q is the squared ratio of the effective light to the heavy quark mass

$$\begin{array}{lcccccc}
\text{charm} & : & \varepsilon_c & \approx & \frac{m_q^2}{m_c^2} & \sim & 0.10 \\
\text{bottom} & : & \frac{\varepsilon_b}{\varepsilon_c} & \approx & \frac{m_c^2}{m_b^2} & \sim & \frac{1}{10}
\end{array}$$

Including the longitudinal phase space factor, we derive the following form of the heavy–quark fragmentation function

$$d_{NP}(z) = \frac{N}{z\left[1 - \frac{1}{z} - \frac{\varepsilon_Q}{1-z}\right]^2} \tag{1.49}$$

which is shown in Fig.1.4. The normalization factor N is given by $4\sqrt{\epsilon_Q}/\pi$ for small ϵ_Q. The average scaled energy of the heavy meson $< z >= 1 - \sqrt{\epsilon_Q}$ approaches unity at the order of $1/m_Q$.

Figure 1.4: *Peterson et al. form of the heavy quark fragmentation function for charm and bottom.*

Even though data is presently insufficient to distinguish between different forms of the heavy quark fragmentation functions, it is clearly established [68] that they are hard.

String form [71]–[72]

In string fragmentation two different approaches have been elaborated to describe the non–perturbative heavy–flavor fragmentation. While in one model the momentum–space aspects are emphasized [73], the other model, which will be discussed in more detail, is based on the space–time properties of the string, leading to a cluster picture, yet with sharply peaked mass distributions for heavy–flavor particles [74, 72].

At large distances the force between heavy quark–antiquark pairs approaches the constant value

$$\sigma = 1\,\mathrm{GeV/fm} = (400\,\mathrm{MeV})^2 \tag{1.50}$$

independent of the distance. This corresponds to a linearly rising potential between the quarks, as nicely demonstrated in lattice QCD simulations [75]. The associated flux tube may be approximated by a string [71] with the string tension σ given by the value (1.50). The mechanical equation of motion for the quark Q

$$\frac{d}{dt}\frac{m_Q v}{\sqrt{1-v^2}} = -\sigma \tag{1.51}$$

is solved by the position vector

$$x(t) = \frac{1}{\sigma}\left[E_0 - \sqrt{(p_0 - \sigma t)^2 + m_Q^2}\,\right] \tag{1.52}$$

and the momentum vector

$$p(t) = p_0 - \sigma t \tag{1.53}$$

E_0, p_0 denote the initial values of energy and momentum. The quarks move on hyperbolae in the 4–dimensional world, spanning a string between the two color sources that sweeps the area between the Q and $\overline{Q}$ branch of the hyperbolae, Fig. 1.5.

In analogy to point–particle decays an area law is postulated for the breaking of the string by the spontaneous creation of a light–quark pair at the position x. The probability of string breaking after an area A has been swept, is taken to be

$$dP_{BREAK} = \lambda e^{-\lambda A} dA \tag{1.54}$$

A is defined as the area bounded by the world lines of the two quarks and a light–like line along which the string break occurs randomly. Relating the break coordinates (x, t) to the energy and momentum of the daughter string spanned between x and Q

$$E = E_0 - \sigma x \qquad \text{and} \qquad p = p_0 - \sigma t \tag{1.55}$$

the invariant area is found to be

Figure 1.5: *Motion of the heavy quarks in the 4–dimensional world and the breaking of the color string.*

$$
\begin{aligned}
A &= \int_0^{\xi_-} d\xi_- \left[\xi_+(Q) - \xi_+(\overline{Q})\right] && (1.56)\\
&= \frac{m_Q^2}{2\sigma^2}\left[\frac{M^2}{m_Q^2}\frac{1}{z} - 1 - \log\left(\frac{M^2}{m_Q^2}\frac{1}{z}\right)\right]
\end{aligned}
$$

in the high–energy limit. M is the mass of the string piece including Q. $\xi_+ = (t \pm x)/\sqrt{2}$ are the light–cone coordinates and z is the scaled energy E/E_0. Elaborating the mechanism for finite energies and accounting for repeated breakings of the daughter strings, the energy spectrum of the final $(Q\overline{q})$ clusters develops a pronounced peak close to $z < 1$, and the cluster masses accumulate at the minimum heavy–flavor particle mass. The numerical results [72] are shown in Fig.1.6 for charm and bottom fragmentation functions in Z decays. A reasonable parametrization is provided by the simple form

$$
D_Q(z) \sim \frac{(1-z)^a}{z^{1+bm_Q^2}} \exp\left[-\frac{bm_Q^2}{z}\right] \qquad (1.57)
$$

with $b = 0.8\,\mathrm{GeV}^{-2}$ and $a \approx 0.5$, the charm/bottom quark masses identified with the masses of the lowest–lying vector meson states.

This form of the string fragmentation function is surprisingly close to the Peterson et al. form as evident by comparing Fig.1.8 and Fig.1.6. The spectrum is considerably softer than the Lund form as a result of the different factor in front which shifts the maximum of the distribution to lower z values. The average z value predicted by this space–time motivated string picture $\langle z \rangle \approx 1 - 1\mathrm{GeV}/m_Q$ coincides with Bjorken's conjecture outlined at the beginning of this section. This is not surprising because in both approaches the hadronic interaction energy between the heavy and the light

Figure 1.6: *Heavy quark fragmentation in the Bowler–Morris string approach.*

quark is provided by the energy of the string piece or of the flux tube, independent of the nature of the quarks as gluonic field sources. The string picture of heavy quark fragmentation may therefore be considered as an approximation to (non–perturbative) QCD that comes closest to intuitive expectations.

The average b–hadron energy [68] at LEP $\langle z_b \rangle = 0.705 \pm 0.011$ can adequately be understood by the convolution of perturbative ($\langle z \rangle_{PT} = 0.8$) with non–perturbative ($\langle z \rangle_{NP} = 0.9$) fragmentation mechanisms.

1.3 Tagging b quarks: QCD tests

Many of the QCD tests are refined considerably if gluon jets can be discriminated from quark jets. Most obvious is the measurement of gluon jet properties: hadron multiplicities, transverse momentum spectra etc. From a variety of other points, two are particularly important, shedding new light on the basic couplings in the QCD interaction density and the particle distributions in multi–jet events.

1.3.1 ggg Coupling in 4–jet events

A key property of QCD is the self–interaction of gluons, a consequence of the non–zero color charges of the gauge particles. The self–coupling is a necessary ingredient to overcome the fermionic screening of color sources and to render the quark–gluon interaction asymptotically free. A variety of tests for the triple–gluon vertex have been discussed in the past, comprising deep–inelastic lepton–nucleon scattering, high–transverse momentum jets in hadron–hadron collisions and heavy quarkonium decays. A qualitatively new test ground has opened with the huge number of high–energy 4–jet events in Z decays. Sufficiently large invariant masses of all jet pairs ensure that these jets truly reflect the distribution of quark and gluon quanta in the femto–universe and thus reveal the basic couplings of the QCD Lagrangian.

The triple–gluon coupling affects jet distributions only at the 4–parton level in the Born approximation. Several methods have been proposed to isolate the ggg diagram [76]–[77]. For this purpose, QCD jet distributions are compared with an

abelian gauge theory in which only the two last diagrams are present. Endowing quarks with three color degrees of freedom and adjusting the quark–gauge boson coupling as $\alpha_A = \frac{4}{3}\alpha_{QCD}$, the total hadronic e^+e^- annihilation cross section, the three–jet cross section and all three–jet distributions are perfectly well described by such an effective theory. Large discrepancies between QCD and this model however occur in 4–jet events. Whereas the dominant contribution in QCD is due to the triple gluon diagram and the 4–quark final state is highly suppressed, the different color flow in the abelian model raises the $q\bar{q}q\bar{q}$ contribution to the same level as the $q\bar{q}g_Ag_A$ bremsstrahl cross section. This induces characteristic differences in the 4–jet distributions even if gluon jets are not tagged. Two examples in which LEP data are compared with the predictions derived from QCD and the abelian theory, are displayed in Fig.1.7.

The comparison proves that the angular distributions are sensitive to the form of the 3–gluon vertex, its Lorentz and color structure. The strength of the coupling has been measured by fitting the ratio of the Casimir invariants [78]

$$N_C/C_F = 2.20 \pm 0.09 \pm 0.13$$

Figure 1.7: *Comparison of 4–jet angular distributions with prediction from QCD and the abelian theory. Data are from the L3 [79] Collaboration at LEP.*

to be compared with the value 9/4 in QCD and 0 in the abelian toy model.

The direct discrimination of the gluon bremsstrahl diagram from the gluon splitting diagram can most convincingly be achieved by tagging quark *vs.* gluon jets. Besides AI techniques [80], b quark tagging provides the most efficient method [8].

(i) *Gluon alignment [76]*

The alignment of the daughter gluons in the splitting process $g \to gg$ forces the two planes, each formed by a high–energy jet together with a low–energy jet, to orient preferentially parallel, with the low–energy jets pointing into the same hemisphere. Unlike the abelian model where the planes tend to be perpendicular to each other. This is demonstrated in Fig.1.8 where non–zero jet resolutions are properly taken into account.

(ii) *NR polar angle [81]*

Virtual helicity–zero gluons of low invariant mass that are radiated from almost back–to–back high–energy quark–antiquark jets cannot decay into gluon jets at 90^o relative to the quark axis. Exploiting the only zero in the spin–one rotation matrix, the range of large polar angles is depleted from low–energy jets in QCD and the jets accumulate at small angles. This is just opposite to virtual gluon decays into quark–antiquark pairs which cannot be emitted along the helicity–zero axis in the massless limit of vector theories. Fig.1.8.

(iii) *Azimuthal angle χ [77]*

Gluons radiated from quarks and antiquarks in $e^+e^- \to q\bar{q}g$ are linearly polarized to a high degree *in* the $q\bar{q}g$ final state plane. Denoting the cross sections for polarizations in and perpendicular to this plane by $d\sigma_{||}$ and $d\sigma_{\perp}$, respectively, QCD predicts

$$\begin{aligned} P(x_g) &= (d\sigma_{||} - d\sigma_{\perp})/(d\sigma_{||} + d\sigma_{\perp}) \\ &= 2(1-x_g)/(x_q^2 + x_{\bar{q}}^2) \end{aligned} \tag{1.58}$$

where, as usual, $x_i = 2E_i/\sqrt{s}$ are the scaled quark and gluon energies in the laboratory frame. The fragmentation of a linearly polarized gluon into daughter partons depends on the azimuthal angle χ between the final state plane and the polarization vector. The asymmetric term is just opposite in sign for gg and $q\bar{q}$ decays,

$$D_{g\to gg}(z,\chi) = \frac{6}{2\pi}\left\{\frac{(1-z+z^2)^2}{z(1-z)} + z(1-z)\cos 2\chi\right\} \tag{59a}$$

$$D_{g\to q\bar{q}}(z,\chi) = \frac{1}{2\pi}\left\{\frac{1}{2}[z^2+(1-z)^2] - z(1-z)\cos 2\chi\right\} \tag{59b}$$

Quark jets accumulate perpendicular to the polarization vector with a maximally pronounced angular distribution $\sim[1-\cos 2\chi]$ for $z=\frac{1}{2}$. The distribution of gluon jets is more isotropic, $\sim[1+\frac{1}{9}\cos 2\chi]$ even for $z=\frac{1}{2}$, so that the angular distribution in QCD is quite distinct from abelian theories. In 4–jet events of e^+e^- annihilation we therefore expect the angle between the plane formed by the two gluon jets and the plane formed by the high–energy primordial quark–antiquark jets to be distributed nearly isotropically in QCD while these planes should be preferentially perpendicular in abelian theories. This is borne out by a detailed 4–jet analysis, Fig.1.8.

Figure 1.8: *4–jet angular distributions in QCD and the abelian model if quark and gluon jets can be distinguished; Ref. [8].*

1.3.2 Particle flow in 3–jet events

In the string picture of quark–antiquark hadronization [63] the boost exerted on the string by the emission of a high–energy gluon, depletes the angular region between the quark and antiquark from particles, while accumulating the particles between the quarks and the gluon. This phenomenon [82], however, may also be explained, in an alternative way, as a perturbative color coherence effect [83]. In QED, soft γ radiation from a configuration of charged antennae as shown on the left, is predicted by Low's theorem:

$$M_\gamma = M_{\rm BORN} \times F_{\rm RAD} \qquad \text{with} \qquad F_{\rm RAD} = \Sigma \frac{e_i \vec{n}_i \vec{\varepsilon}}{\vec{n}_i \vec{n}} \tag{1.60}$$

where $\vec{n}$ is the γ flight direction. Apparently $F_{RAD}(\vec{n})$ vanishes for $\vec{n}$ midway between $\vec{n}_1$ and $\vec{n}_2$.

This approach, translated to QCD, predicts many fine details of the particle flow in multi–jet events. For a given $q\overline{q}g$ jet configuration, kinematically fixed by tagged heavy quarks, the angular distribution of the particle flow between the jets can be written as [83]

$$\frac{dN^{q\overline{q}g}}{d\vec{n}} \propto [gq] + [g\overline{q}] - \frac{1}{N_c^2}[q\overline{q}] \tag{1.61}$$

where

$$[ij] = \frac{a_{ij}}{a_i a_j} \qquad \left\{ \begin{array}{lcl} a_i & = & 1 - \cos\theta_i \\ a_{ij} & = & 1 - \cos\theta_{ij} \end{array} \right. \qquad \begin{array}{lcl} \theta_i & = & [\vec{n}, \vec{n}_j] \\ \theta_{ij} & = & [\vec{n}_i, \vec{n}_j] \end{array}$$

The first two terms in (1.61) agree with the celebrated string effect while the last negative term is the result of interference effects between the radiation from the q, $\overline{q}$ and g antennae, not accounted for by independent string fragmentation. These interference effects enhance the asymmetry of particle yields between quark–gluon and quark–antiquark jets, a consequence of the repulsive force between q and $\overline{q}$ in a colour octet state. The result can best be illustrated for 3–fold symmetric $q\overline{q}g$ events ($\theta_{q\overline{q}} = \theta_{qg} = \theta_{g\overline{q}} = 120^o$). The ratios of the multiplicity flows projected onto the $q\overline{q}g$ plane in the qg and $q\overline{q}$ sectors, are

$$\frac{N_{qg}}{N_{q\overline{q}}} \simeq \frac{5 - 1/N_c^2}{2 - 4/N_c^2} = \left\{ \begin{array}{ll} 3.14 & \text{with interference} \\ 2.5 & \text{without } [N_c \to \infty] \end{array} \right. \tag{1.62}$$

Thus with interference this ratio is markedly different from the prediction of non–interacting strings. [In the case of untagged jets the ratio is considerably reduced due to the smearing which is caused by the mismatch of quark and gluon jets.]

1.4 Inclusive production of J/ψ, Υ and B_c

In addition to the resonant production of spin 1 quarkonia at low energies these states can also be produced in Z decays through a variety of processes.

The clean initial state configuration typical for e^+e^- annihilation is ideal to investigate the relative importance of different quarkonium production mechanisms. Two distinctly different situations have been considered: high energy reactions like Z decays with large event rates available at LEP and alternatively the 10 GeV region that can be explored at present at CESR or in the near future at the B-meson factories. Three mechanisms have been identified at which contribute in the high energy region with comparable rates. The reaction [84]

$$Z \to J/\psi c\bar{c} + X \tag{1.63}$$

requires the production of two $c\bar{c}$ pairs with a rate proportional to $\alpha_s^2|R(0)|^2$. The second mechanism [85, 86] is the splitting of a virtual gluon in a color octet $c\bar{c}$:

$$Z \to q\bar{q}(c\bar{c})_8 \tag{1.64}$$

with the subsequent nonperturbative conversion of $(c\bar{c})_8$ into J/ψ. The rate for this mechanism is proportional to $\alpha_s^2\langle\mathcal{O}^8\rangle$ where the second factor characterizes the nonperturbative matrix element and must be considered as an additional free parameter. Rates and distributions calculated in this approach are fairly close to those expected in the "color evaporation" model [87]. The third, color singlet, contribution [88]

$$Z \to q\bar{q}J/\psi gg \tag{1.65}$$

is strongly suppressed by the factor $\alpha_s^4|R(0)|^2$ and, furthermore, by the small phase space. The branching ratios of the three reactions are given by $0.8 \cdot 10^{-4}$, $1.9 \cdot 10^{-4}$, $0.2 \cdot 10^{-4}$, respectively. The total inclusive rate is reasonably consistent with the observations by the OPAL collaboration [89] of $(1.9 \pm 0.7 \pm 0.5 \pm 0.5) \cdot 10^{-4}$. However, a statement about the dominance of any of these processes seems premature. The analysis of J/ψ energy and momentum distributions, however, could help to settle this issue.

Also B meson factories and CESR give rise to a large sample of events with prompt J/ψ production. Two mechanisms have been proposed which might well describe complementary kinematical regions. The leading process in the CSM

$$e^+e^- \to J/\psi + gg \tag{1.66}$$

is proportional to $\alpha_s^2|R(0)|^2$. It leads to a three body final state and hence to a continuous energy distribution. Predictions for the rate, the angular and the momentum distribution and the polarization can be found in [90]. The alternative approach [91] is based on "color octet production", $e^+e^- \to (c\bar{c})_8 + g$. The rate is of order α_s and multiplied by a nonperturbative matrix element. The J/ψ energy is essentially fixed at $E_{max} = (s + m_\psi^2)/(2\sqrt{s})$. The angular distribution is proportional to $(1 + \cos^2\theta)$. These features are identical to the predictions of the "color evaporation model" [92] formulated a long time ago. An excess of J/ψ at this special kinematical point with the predicted angular distribution would be a strong indication for this "octet mechanism". The angular distribution of the J/ψ in the CSM is of the form $1 + \alpha(y)\cos^2\theta$ where $\alpha(y)$ depends on $y \equiv E_\psi/E_{Beam}$ and approaches roughly -0.8 at the endpoint. This difference will be crucial in disentangling the two mechanisms.

Charmed bottom mesons B_c can be produced at an appreciable rate only through $\left(\bar{b}c\right) \to B_c$ fusion in perturbatively generated $Z \to b\bar{b}, c\bar{c}$ final states. [Spontaneous nonperturbative $c\bar{c}$ pair creation in a gluonic flux tube is suppressed at a level of 10^{-11}]. Folding the 4-quark production amplitude with the $b\bar{c}$ quark-antiquark bound-state wave function, a branching ratio for $Z \to B_c$ of order 10^{-4} to 10^{-5} has been estimated in [93, 94, 95] so that order 100 to 1,000 B_c are expected in 10^7 Z decays. The final state has a remarkable signature: an isolated B_c meson plus 2 jets. The lifetime of the B_c meson is determined by the combination of charmed and bottom quark lifetimes. Decay modes like $B_c \to J/\psi + \pi^-$ or $J/\psi + l\bar{\nu}$ with branching ratio around 1% [96] have allowed to set nontrivial bounds on this channel [97].

1.5 Lifetimes and mixing of b–flavor hadrons

The measurement of lifetimes and mixing of hadrons built–up by b quarks is made possible by the large time dilation factor γ in high energy machines, leading to flight distances of macroscopic size.

1.5.1 Lifetimes of b–particles

Hadrons with b flavor are known to have a long lifetime (see e.g. [98, 99, 100]). This is the consequence of the small Kobayashi–Maskawa coupling between b and c quarks that neutralizes the large mass m_b in the Fermi decay of the b quark. Because the fragmentation of the b quarks to mesons and baryons is hard, they have a large γ factor ≤ 8 when they are produced in Z decays. The average flight distance is about 2 mm, the average impact parameter in the transverse plane is about 0.2 mm, so that the particles can well be analyzed in high–resolution vertex detectors. Three methods are employed to measure the lifetimes: (i) Average lifetimes can be determined from the impact parameter δ of the charged lepton in semileptonic decays. At LEP this parameter is insensitive to the momentum of the decaying particle and directly proportional to τ [$\delta \sim c\tau$]. (ii) Exclusive B lifetime measurements can be carried out by reconstructing fully hadronic decays. This method is ideal for hadron collider experiments with the $J/\psi K$ or $J/\psi K^*$ channels as prominent examples. However, it suffers from low statistics in Z decays. (iii) Partial reconstruction of B mesons, for example in semileptonic decays to D or D^*, allows at the same time for the separation between B^0 and B^- and the identification of B meson decay vertices.

With the advent of sophisticated microvertex detectors the exponential decay distribution of B mesons has been nicely established (Fig. 1.9).

Unlike charm, the spectator model is expected to provide a valid approximation for b–particle decays. In this model the lifetime is determined by the b–quark, irrespective of the other quarks in the hadronic environment. As a result, the lifetimes of b–particles [except B_c, see later] are approximately universal. The model includes perturbative QCD corrections of the b Fermi decay and phase space effects due to non–zero quark masses which – because being not well defined in the present context – introduce some uncertainties. These have been reduced during the past years through the evaluation of higher order perturbative corrections and the machinery of Heavy Quark Effective Theory. From the decay rate the dominating *CKM* matrix element can be extracted. Note that this matrix element, though coupling quarks of two neighboring families, is of the order of the Cabibbo angle squared.

Figure 1.9: *Plot of excess decay times showing an exponential distribution (from [98]).*

Non–spectator diagrams render the lifetimes individually different within a small margin. This is illustrated for the most prominent examples [101, 102]:

B^-	$=$	$(b\overline{u})$	:	destructive interference between $\overline{u}'s$, caused by the Pauli principle in the spectator diagram, prolonging the lifetime;
$\overline{B}^0_d$	$=$	$(\overline{b}d)$	:	W exchange diagram $\overline{b}d \to \overline{c}u$, shortening the lifetime;
$\overline{B}^0_s$	$=$	$(\overline{b}s)$	:	W exchange $\overline{b}s \to \overline{c}u$, shortening the lifetime;
Λ_b	$=$	(bud)	:	W exchange $bc \to ud$, shortening the lifetime; but overwhelming dd Pauli suppression;

The differences in the hierarchy

$$\tau(B^-) > \tau(\overline{B}^0_s) \geq \tau(\overline{B}^0_d) > \tau(\Lambda_b) \tag{1.67}$$

have conservatively been estimated to be at most at a level of 10%.

The most recent experimental results for B mesons [98, 100]

$$\begin{aligned} \tau(B^-) &= 1.65 \pm 0.04 \text{ ps}, \\ \tau(B^0) &= 1.55 \pm 0.04 \text{ ps}, \\ \tau(B_s) &= 1.52 \pm 0.07 \text{ ps}; \\ \tau(B^-)/\tau(B^0) &= 1.04 \pm 0.04, \qquad \tau(B_s)/\tau(B^0) = 0.98 \pm 0.05, \end{aligned} \tag{1.68}$$

are well consistent with these expectations. The present measurement of $\tau(\Lambda_b)$ [99], however, with

$$\tau(\Lambda_b) = 1.21 \pm 0.06 \text{ ps}, \qquad \tau(\Lambda_b)/\tau(B^0) = 0.78 \pm 0.04, \tag{1.69}$$

is difficult to accomodate in calculations based on HQET [102].

1.5.2 $B-\overline{B}$ mixing

Oscillations between neutral B_d^0, B_s^0 particles and antiparticles are induced by higher order weak diagrams as shown below. A B^0 beam at $t=0$ develops at time t a $\overline{B}^0$ component and vice versa [103],

$$\begin{aligned} B^0 &\to \left[\cos\left(\frac{\Delta m t}{2}\right) B^0 + \frac{iq}{p}\sin\left(\frac{\Delta m t}{2}\right)\overline{B}^0\right] \\ \overline{B}^0 &\to \left[\frac{ip}{q}\sin\left(\frac{\Delta m t}{2}\right) B^0 + \cos\left(\frac{\Delta m t}{2}\right)\overline{B}^0\right] \end{aligned} \tag{1.70}$$

[$\Delta\Gamma \equiv \Gamma_H - \Gamma_L = 0$ and hence $|p/q| = 1$ has been assumed for the moment].

Defining the average width of the long– and short–lived state by $\Gamma = \frac{1}{2}(\Gamma_H + \Gamma_L)$, the oscillatory behavior is governed by the ratio of the oscillation frequency to the decay rate,

$$x = \frac{\Delta m}{\Gamma} \tag{1.71}$$

with $\Delta m = m_H - m_L$ being the mass difference of the weak eigenstates. The strength of the oscillation amplitude is maximal for vanishing

$$y = \frac{\Delta\Gamma}{2\Gamma},$$

a valid approximation for the B_d^0 system. The particle/antiparticle components can be detected by recording, for example, the lepton charges in semileptonic $B^0 \to l^+$ and $\overline{B}^0 \to l^-$ decays. [This applies clearly to B_d^0; for B_s^0 the assumption $\Delta\Gamma \ll \Gamma$ has been disputed [104] and a more general analysis would then be required.]

$$B^0 \to \begin{cases} N[B^0 \xrightarrow{t} l^+] & \sim e^{-\Gamma t}[1 + \cos\Delta m t] \\ N[\overline{B}^0 \xrightarrow{t} l^-] & \sim e^{-\Gamma t}[1 - \cos\Delta m t] \end{cases} \tag{1.72}$$

Integrated over all times, the mixing probability follows from

$$\begin{aligned} \chi &= \frac{P\left\{B^0 \to \overline{B}^0\right\}}{P\left\{B^0 \to B^0\right\} + P\left\{B^0 \to \overline{B}^0\right\}} = \frac{1}{2}\frac{x^2+y^2}{x^2+1} \\ &\approx \frac{1}{2}\frac{x^2}{x^2+1} \qquad \text{for } B_d^0 \text{ and presumably also } B_s^0. \end{aligned} \tag{1.73}$$

The oscillation frequency in the B_d system,

$$\Delta m \sim |V_{td}|^2 m_t^2 f_{B_d}^2 \eta_B \tag{1.74}$$

is determined by three factors: (i) the *CKM* coupling of t quarks to d quarks [the *CKM* element (tb) is very close to unity]; (ii) the top quark mass which makes the t exchange dominating over u, c exchange contributions (note that the CKM elements are of order λ^3 for all three exchange amplitudes); (iii) the quark wave function of the meson at the origin; and (iv) perturbative QCD corrections. The ratio y_d on the other hand is expected to be small since the dominant decay channels are not self–conjugate.

The mixing parameter x_s can be estimated in the Standard Model by comparing the box diagrams for B_s^0 with B_d^0 transitions:

$$x_s \approx x_d \left|\frac{V_{ts}}{V_{td}}\right|^2 \frac{\tau(B_d)}{\tau(B_c)}\frac{m(B_s)}{m(B_d)}\xi^2 \approx x_d \left|\frac{V_{ts}}{V_{td}}\right|^2 \tag{1.75}$$

with the non-perturbative parameter ξ which parametrizes the deviation from SU(3) symmetry. In the Wolfenstein expansion of the Cabibbo–Kobayashi–Maskawa matrix

$$V = \left\| \begin{array}{ccc} V_{ud} & V_{uc} & V_{ub} \\ V_{cd} & V_{cs} & V_{cb} \\ V_{td} & V_{ts} & V_{tb} \end{array} \right\| = \left\| \begin{array}{ccc} 1-\frac{\lambda^2}{2} & \lambda & A\lambda^3[\rho - i\eta] \\ -\lambda & 1-\frac{\lambda^2}{2} & A\lambda^2 \\ A\lambda^3[1-\rho-i\eta] & -A\lambda^2 & 1 \end{array} \right\| + \mathcal{O}(\lambda^4)$$

[with $\lambda \approx 0.22$ being the Cabibbo angle] the ratio

$$\left|\frac{V_{ts}}{V_{td}}\right|^2 = \frac{1}{\lambda^2\left[(1-\rho)^2+\eta^2\right]} \tag{1.76}$$

is constrained from an analysis [103] of the unitarity triangle to the range between 10 and 40. For SU(3) symmetric quark wave functions, the Standard Model brackets thus x_s to

$$7.3 < x_s < 29.2$$

However, SU(3) symmetry breaking very likely raises ξ^2 to a value above unity. Recent results based on lattice calculations and QCD sum rules are consistent with an enhancement factor around 1.3. A mixing parameter x_s close to 1/2 is therefore expected and has indeed been observed experimentally [105], rendering the extraction of x_s difficult. For the same reason oscillations in the B_s^0 system will be very rapid, as exemplified in Fig.1.10.

The time integrated mixing, first observed by the ARGUS collaboration [107], has been explored in $\Upsilon(4s)$ decays with improved precision during the past years. When converted into a value for Δm_d, the present results $0.462 \pm 0.071 \pm 0.066$ ps^{-1} and $0.418 \pm 0.046 \pm 0.044$ ps^{-1} from ARGUS and CLEO respectively are nicely consistent with the present world average $0.466 \pm 0.012 \pm 0.013$ ps^{-1}. The latter is dominated by the time dependent measurement at high energy e^+e^- and $p\bar{p}$ colliders discussed below.

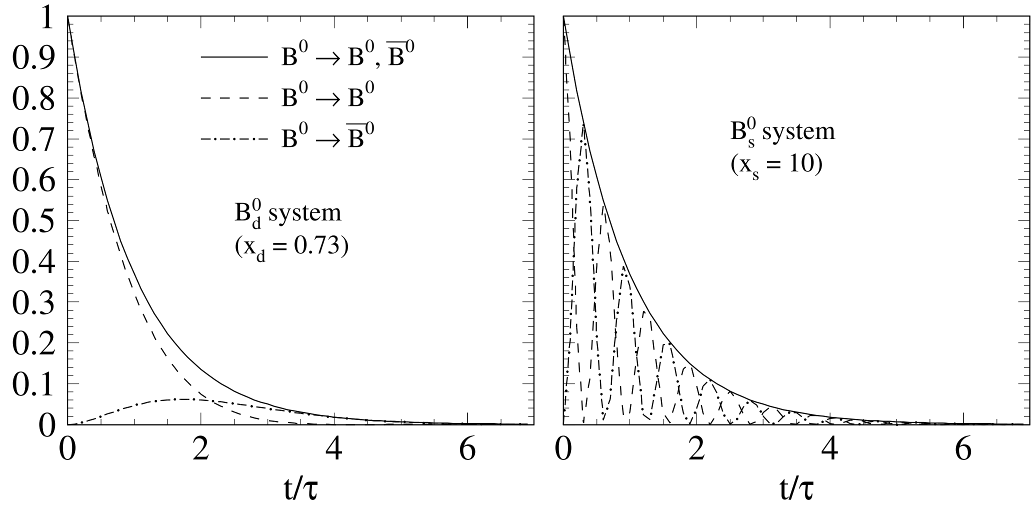

Figure 1.10: *Time evolution for the B_d^0 and B_s^0 system.*

Most flavor tags rely on the fact that b quarks are produced in pairs, with the like–sign dilepton analysis as the most prominent example. The SLD experiment utilizes furthermore the large forward backward asymmetry for polarized beams

$$A_{FB} = 2A_b \frac{A_e + P_e}{1 + A_e P_e} \frac{\cos\theta}{1 + \cos^2\theta} \tag{1.77}$$

with $A_e = 0.155$, $A_b = 0.94$, to enhance the purity of the b quark signal.

The time evolution resulting from the mixing has been demonstrated at LEP by analyzing the flavor as a function of the distance from the produciton vertex in one jet (decay tag) while the b-flavor of the jet on the opposite side is fixed (production tag). For the B_d system the oscillatory behavior is clearly visible (Fig. 1.11) and the oscillation frequency provides a direct measurement of Δm_d, independent of Γ_d. Only lower bounds on x_s (or Δm_s) have been established until now and no oscillation has been observed. The earlier inclusive analyses were based on like–sign dilepton events and thus heavily dependent on the relative fractions of B_s^0 vs. B_d^0 resulting from b quark hadronisation. More recent analyses identify specifically B_s mesons through their decay into (reconstructed!) D_s or ϕ mesons, selecting thus a fairly clean sample and allowing for an improved determination of the decay time. A compilation of the recent results for Δm_d and Δm_s can be found in [105]. The world average $\Delta m_d = 0.466 \pm 0.012 \pm 0.013$ ps^{-1} in combination with the lower limit $\Delta m_s > 9.2$ ps^{-1} leads to interesting constrains on quark mixing already now.

While the observation of $B_d^0 - \overline{B}_d^0$ mixing by ARGUS gave the first indication of a very heavy top quark in the past, the time dependence of $B_s - \overline{B}_s$ oscillations will serve in the future to determine the *CKM* matrix elements V_{td} and V_{ts}. With the mass parameter m_t measured experimentally, two cases can be realized. If the presently

Figure 1.11: *The ratio, R, of like–sign events to total events, as a function of reconstructed proper decay time, for selected $D^{*+}\ell^-/Q_J$ events.*

unknown decay constant f_{B_d} could be calculated reliably or measured in $B \to \tau\nu_\tau$ decays, the mixing parameter x_d determines the *CKM* element $|V_{td}|$. If f_B cannot be determined reliably, this *CKM* element must be extracted from the ratio x_s/x_d which depends less strongly on the mesonic wave functions. Since $|V_{ts}|$ is fairly close to $|V_{cb}|$ and can therefore be measured in B decays, the *CKM* matrix element $|V_{td}|$ can be deduced from the comparison of B_d^0 and B_s^0 mixing data.

Chapter 2

t QUARK

The top quark completes the fermion spectrum of the Standard Model so that all its properties are uniquely determined when the mass is fixed. Top quarks were elusive particles for a long time, searched for more than a decade before they could be isolated at the Tevatron [3] with a mass value [108]

$$m_t = 175.5 \pm 5.1 \text{ GeV} \tag{2.1}$$

This directly measured value matches very well early estimates which were derived from precision measurements of the electroweak parameters in e^+e^- annihilation: $m_t = 177 \pm 19$ GeV [109]. The coincidence of the two values is a triumph of field theory allowing us to control the quantum fluctuation in the W, Z boson masses which are affected by virtual top quarks.

The next major step after the discovery of the top quark will be the high–precision analysis of its properties. A large number of top quarks [order 10^7] will be produced at the pp collider LHC [12], necessary to measure the mass within a few GeV and to search for hypothetical very rare decay modes. High energy e^+e^- linear colliders [5] can improve the accuracy in the top sector considerably. The precision with which the fundamental t mass, a key parameter of flavor physics, can be determined, increases to a level of 100 MeV. Moreover, the static electroweak parameters and non–standard decay modes can be analysed with high precision.

2.1 Early evidence for top quarks

2.1.1 t – The ekasilicon of the Standard Model

Several experimental results had provided quite early very strong evidence that the fermion spectrum of the Standard Model

$$\begin{bmatrix} \nu_e \\ e^- \end{bmatrix}_L \quad e_R^- \qquad \begin{bmatrix} \nu_\mu \\ \mu^- \end{bmatrix}_L \quad \mu_R^- \qquad \begin{bmatrix} \nu_\tau \\ \tau^- \end{bmatrix}_L \quad \tau_R^-$$

$$\begin{bmatrix} u \\ d \end{bmatrix}_L \quad \begin{matrix} u_R \\ d_R \end{matrix} \qquad \begin{bmatrix} c \\ s \end{bmatrix}_L \quad \begin{matrix} c_R \\ s_R \end{matrix} \qquad \begin{bmatrix} t \\ b \end{bmatrix}_L \quad \begin{matrix} t_R \\ b_R \end{matrix}$$

must include the top quark, imprinting the same multiplet structure on the third family as observed in the first two families. The evidence was deduced from measurements of the weak isospin of the b quark which had been proved to be non-zero, $I_3 = -1/2$, thus demanding an $I_3 = +1/2$ partner in this isospin multiplet.

Absence of triangle anomalies

A compelling theoretical argument for the existence of top quarks follows from consistency requirements. The renormalizability of the Standard Model demands the absence of triangle anomalies. Triangular fermion loops built-up by an axialvector charge $I_{3A} = -I_{3L}$ combined with two electric vector charges Q would spoil the renormalizability of the gauge theory. Since the anomalies do not depend on the masses of the fermions circulating in the loops, it is sufficient to demand that the sum

$$\begin{aligned} &\sim \sum_L I_{3A} Q^2 = -\sum_L I_3 \left[I_3 + \frac{1}{2} Y \right]^2 \\ &\sim \sum_L Y \sim \sum_L Q \end{aligned}$$

of all contributions be zero. Such a requirement can be translated into a condition on the electric charges of all the left-handed fermions

$$\sum_L Q = 0 \tag{2.2}$$

This condition is met in a complete standard family in which the electric charges of the lepton plus those of all color components of the up and down quarks add up to zero,

$$\sum_L Q = -1 + 3 \times \left[\left(+\frac{2}{3} \right) + \left(-\frac{1}{3} \right) \right] = 0$$

If the top quark were absent from the third family, the condition would be violated and the Standard Model would be theoretically inconsistent.

Absence of FCNC decays

Mixing between quarks which belong to different isospin multiplets

$$\begin{bmatrix} c \\ s' \end{bmatrix}_L \quad b'_L \qquad\qquad \begin{aligned} s' &= s \cos\vartheta' + b \sin\vartheta' \\ b' &= -s \sin\vartheta' + b \cos\vartheta' \end{aligned}$$

generates non-diagonal neutral current couplings, i.e. the breaking of the GIM mechanism

$$
\begin{aligned}
< I_3 > &= +\frac{1}{2}(c_L, c_L) - \frac{1}{2}\left(s_L^{'}, s_L^{'}\right) \\
&= \text{diag.} - \frac{1}{2}\sin\vartheta^{'}\cos\vartheta^{'}\,(s_L, b_L) + \text{h.c.} \quad .
\end{aligned}
$$

The non-diagonal current induces flavor-changing neutral lepton pair decays $b\rightarrow s + l^+l^-$ which have been estimated to be a substantial fraction of all semileptonic B meson decays [110]

$$
\frac{\mathrm{BR}\,(B\rightarrow l^+l^-X)}{\mathrm{BR}\,(B\rightarrow l^+\nu_l X)} \geq 0.12 \tag{2.3}
$$

This ratio is four orders of magnitude larger than a bound set recently by the UA1 Collaboration [111]

$$
\frac{\mathrm{BR}\,(B\rightarrow \mu^+\mu^-X)}{\mathrm{BR}\,(B\rightarrow \mu\nu_\mu X)} < \frac{5.0\times 10^{-5}}{0.110\pm 0.008} \tag{2.4}
$$

so that the working hypothesis of an isosinglet b quark is clearly ruled out experimentally also by this method.

Partial width $\Gamma(Z\rightarrow b\bar{b})$ and forward-backward asymmetry of b quarks

The isospin quantum numbers of the b quarks have been measured directly through the Z–decay width to b quarks $\Gamma(Z\rightarrow b\bar{b})$ and the forward–backward asymmetry of b quarks on the Z, $A_{FB}(b)$, at LEP. If combined with b data from PETRA/PEP and TRISTAN, a unique solution can be derived for the third isospin components of the left– and right–handed b quarks [112], Fig.2.1,

$$
\begin{aligned}
\{I_3^L(b)\}_{exp} &= -0.490^{+0.015}_{-0.012} & &\rightarrow & I_3^L(b) &= -1/2 \\
\{I_3^R(b)\}_{exp} &= -0.028\pm 0.056 & &\rightarrow & I_3^R(b) &= 0
\end{aligned}
$$

which coincide with the isospin assignment of the Standard Model.

2.1.2 Mass estimate from radiative corrections

First indications of a very high top quark mass were derived from the rapid $(B-\overline{B})$ oscillations observed by ARGUS [107]. However, due to the uncertainties of the CKM matrix element V_{td} and of the $(b\bar{d})$ wave function, no more than qualitative conclusions can be drawn from such an analysis as the oscillation frequency $\Delta m \sim |V_{td}|^2 f_B^2 m_t^2$ depends on three [unknown] parameters.

The analysis of the radiative corrections to high precision electroweak observables, measured at LEP and elsewhere, could be carried out at a quantitativ level. Since Higgs mass effects are weak as a result of the screening theorem [113], the top mass is the central unknown parameter in the framework of the Standard Model. Combining

Figure 2.1: *The weak isospins $I_3^L(b)$ and $I_3^R(b)$ of the left– and right–handed b quark components, extracted from the data on $\Gamma(Z \to b\bar{b})$ and $A_{FB}(b)$ at LEP, and PETRA/PEP and TRISTAN, Ref.[112].*

the high precision measurements of the Z mass with $\sin^2\theta_W$ from the Z decay rate, the forward-backward asymmetry and LR polarization measurements, the top quark mass has been determined up to a residual uncertainty of ± 19 GeV, including the uncertainty through the variation of m_H.

The key rôle is played by the connection of the Z mass with $\sin^2\theta_W$ and the low-energy couplings α, G_F. Through radiative corrections [1] this connection is strongly affected by the t quark mass. Linking the Glashow-Salam-Weinberg theory to the effective low-energy Fermi theory of the weak interactions relates the Fermi coupling G_F with the GSW $SU(2)$ coupling $g = e/\sin\theta_W$ and the W mass. After the QED radiative corrections are taken into account by substituting for α the running coupling $\alpha\,(m_Z^2) = \alpha/\,(1-\Delta\alpha) = 1/128.896$ ..., the top quark mass is introduced through the genuine electroweak corrections, essentially the ρ parameter of the (tb) loop in the W

[1] Again, the on-shell renormalization scheme will be adopted.

propagator (see also Sect. 1.1.1). The final relation can be cast into the form

$$\sin^2\theta_W \cos^2\theta_W m_Z^2 = \frac{\pi\alpha}{\sqrt{2}G_F\left[1-\Delta\alpha+3G_F m_t^2\cot^2\theta_W/16\pi^2\right]} \tag{2.5}$$

Given the high precision with which m_Z and $\sin^2\theta_W$ have been measured, the mass of the top quark can be derived from eq.(2.5). Including small corrections from loops involving the Higgs particle, one finds [109]

$$m_t = 177^{+7+17}_{-8-19}\ \mathrm{GeV} \tag{2.6}$$

The second error results from the variation of the Higgs mass between 60 and 1000 GeV with a central value of 300 GeV. The same analysis leads to an upper limit of 181 GeV (95% CL). The present data are summarized in Fig.2.2 in the m_t, m_H plane. The predictions derived from the radiative corrections and the high–precision electroweak data are compared with an overall fit including the direct measurement of the top mass at the Tevatron. These analyses, in particular the ρ value, are quite stable when possible extensions of the Standard Model are taken into account.

With the enhanced precision for M_W and m_t expected from the next generation of experiments, it may well be possible to determine the mass of the Higgs boson by the same method with a precision around 20 %.

Present theoretical analyses of the Standard Model are based almost exclusively on perturbation theory. Since the t mass is still sufficiently small, this method can also be applied the top-quark sector. The following consistency conditions are fulfilled:

Yukawa coupling $g_Y\,(ttH)$

In the Standard Model the Yukawa coupling is related to the top mass by

$$g_Y\,(ttH) = m_t\sqrt{\sqrt{2}G_F} \tag{2.7}$$

For a top mass of 175 GeV the coupling $g_Y^2/4\pi \approx 0.04$ is comfortably small so that the perturbation theory can safely be applied in the top–Higgs sector.

Unitarity bound

At asymptotic energies the amplitude of the zeroth partial wave for elastic $t\bar{t}$ scattering in the color singlet same-helicity channel [114]

$$\begin{aligned} a_0\,(t\bar{t}\to t\bar{t}) &= -\frac{3g_Y^2}{8\pi} \\ &= -\frac{3G_F m_t^2}{4\sqrt{2}\pi} \end{aligned} \tag{2.8}$$

grows quadratically with the top mass. Unitarity, however, demands this real amplitude to be bounded by $|\mathrm{Re}\,a_0| \leq 1/2$. With $|a_0| \simeq 0.06$, this condition is met for a top mass of 175 GeV.

Figure 2.2: *The 68% confidence level contours in m_t and m_H for the fits to LEP data only (dashed curve) and to all data including the CDF/D0 m_t measurement (solid curve); Ref. [44].*

Stability of the Higgs system: top-Higgs bound

The quartic coupling λ in the effective Higgs potential

$$V = \mu^2 \left|\phi\right|^2 + \frac{\lambda}{2} \left|\phi\right|^4$$

depends on the scale at which the system is interacting. The running of λ is induced by higher-order loops built-up by the Higgs particles themselves, the vector bosons and the fermions in the Standard Model [115, 116]. For small values of the top mass, $m_t \leq 77$ GeV, these radiative corrections generate a lower bound on the Higgs mass [$< 7\,\mathrm{GeV}$]. At high energies they make λ rise,

$$\frac{\partial \lambda}{\partial \log s} = \frac{3}{8\pi^2}\left[\lambda^2 - 4g_Y^4 + \text{gauge couplings}\right] \tag{2.9}$$

up to the Landau pole at the cut-off parameter Λ beyond which the Standard Model in the present formulation cannot be continued ["triviality bound", as this bound could formally be misinterpreted as requiring the low energy coupling to vanish]. If for a fixed Higgs mass the top mass is increased, the top–loop radiative corrections lead to negative values of the quartic coupling λ. Since the potential is unbounded from below in this case, the Higgs system becomes instable. Thus the stability requirement defines an upper value of the top mass m_t for a given Higgs mass m_H and a cut-off scale Λ. The result of such an analysis is presented in Fig.2.1.2. If the fundamental particles remain weakly interacting up to the Planck scale, a top mass of 175 GeV restricts the range of possible Higgs mass to a narrow gap between 130 and 180 GeV.

Figure 2.3: *Bounds on the Higgs and top masses following from triviality of the Higgs's quartic self-coupling and the stability of the Higgs system; from [116].*

2.2 Top quark decays in the Standard Model and beyond

2.2.1 Born predictions

The total rate

Based on the Standard Model, the lower limit of the top quark mass $m_t > 91\ GeV$ has been shifted to a level well above the real W threshold for the decay mode $t \to b{+}W^+$. In the three-family SM the CKM matrix element of the tb coupling V_{tb} is well known to be very close to unity. As a result, the width of the top quark is dominated by decays into a W plus a b jet and can be precisely predicted in the SM [117, 66] :

$$\begin{aligned}\Gamma\left(t \to b + W\right) &= |V_{tb}|^2 \frac{G_F m_t^3}{8\sqrt{2}\pi} \frac{2P_W}{m_t} \left\{ \left[1 - \left(\frac{m_b}{m_t}\right)^2\right]^2 + \left[1 + \left(\frac{m_b}{m_t}\right)^2\right] \left(\frac{m_W}{m_t}\right)^2 \right. \\ &\left. -2\left(\frac{m_W}{m_t}\right)^4 \right\} \approx \frac{G_F m_t^3}{8\sqrt{2}\pi}\left(1 - \frac{m_W^2}{m_t^2}\right)^2 \left(1 + 2\frac{m_W^2}{m_t^2}\right) \qquad (2.10)\end{aligned}$$

The branching ratios BR($t \to q + W^+$) for q=b,s,d follow from [103]

$$\begin{aligned} 0.9991 \leq |V_{tb}| \leq 0.9993 &\Rightarrow BR(b) \approx 1 \\ 0.0353 \leq |V_{ts}| \leq 0.0429 &\Rightarrow BR(s) \approx 0.2\% \\ 4.5 \cdot 10^{-3} \leq |V_{td}| \leq 13.7 \cdot 10^{-3} &\Rightarrow BR(d) \approx 0.01\% \qquad (2.11)\end{aligned}$$

While the search for $s{+}W^+$ final states, though difficult, is not impossible, the t production rates will be too small to look for $d{+}W^+$ decay products.

For m_t around 175 GeV the width is already close to the asymptotic form

$$\Gamma\left(t \to b + W^+\right) \to 175MeV \cdot \left(\frac{m_t}{m_W}\right)^3 \qquad (2.12)$$

and the lifetime drops below $10^{-23}s$. This is illustrated in Fig. 2.4.

The final state consists of a b-quark jet plus a lepton pair or two other jets from the W decay which, being a color singlet system, fragments independent from the environment.

The decay rate can be split into the contribution from W's with longitudinal ($h_W = 0$) and transverse ($h_W = +1$) polarizations. Neglecting b-quark mass effects, the ratio

$$\Gamma_L/\Gamma_T = m_t^2/2m_W^2 \qquad (2.13)$$

amounts to 2.35 for m_t = 175 GeV.

Figure 2.4: *The width of the top quark in the Standard Model. The degree of longitudinal polarization is shown in the insert.*

Spectra

Arising from a two body decay the energy of the W and of the hadronic system ($\equiv b$ jet) are fixed to

$$\begin{aligned} E_W &= \frac{m_t^2 + m_W^2 - m_b^2}{2m_t} \\ E_h &= \frac{m_t^2 + m_b^2 - m_W^2}{2m_t} \end{aligned} \tag{2.14}$$

as long as gluon radiation is ignored. The smearing of this δ spike from the combined effects of perturbative QCD and from the finite width of the W will be treated in the next section.

The energy spectra of the leptons from the decay of the real W, and correspondingly the invariant (bl) mass are strongly affected by the chirality of the (tb) charged weak current for moderate top masses. Assuming the charged lepton current to be of the well-established $V-A$ form, the probability to observe a charged lepton of maximal energy $E_l = m_t/2$ vanishes for the conventional $V-A$ form of the (tb) current while it is nonzero for a speculative $V+A$ coupling.

$$\frac{dN}{dx} = f_\pm(x,y) \qquad (V \pm A)_{tb} \quad \text{coupling} \tag{2.15}$$

with $\quad y \leq x \leq 1$, where $x = 2E_l/m_t$, $y = m_W^2/m_t^2$, $m_b = 0$, and

$$
\begin{aligned}
f_-(x,y) &= 6x(1-x)/[(1-y)^2(1+2y)] \\
f_+(x,y) &= 6(x-y)(1+y-x)/[(1-y)^2(1+2y)]
\end{aligned} \tag{2.16}
$$

For a mixture of $V-A$ and $V+A$ amplitudes of relative weights w_- and w_+ with $w_+^2 + w_-^2 = 1$

$$
\mathcal{M} \sim \bar{u}_b \not{\epsilon}_W \left(w_-(1-\gamma_5) + w_+(1+\gamma_5)\right) u_t \tag{2.17}
$$

(assuming $m_b = 0$) one obtains an incoherent sum of their respective contributions

$$
\frac{dN}{dx} = w_-^2 f_- + w_+^2 f_+ \tag{2.18}
$$

A deviation from the V-A structure would thus lead to a stiffening of the charged lepton spectrum, and in particular to a nonvanishing distribution at the upper end point.

Equivalently, the distribution of the invariant (bl) mass $\mu^2 = m_{bl}^2/m_t^2$ is given by the same functions as above

$$
\frac{dN}{d\mu^2} = f_\pm(\mu^2 + y, y) \qquad (V \pm A) \quad \text{coupling} \tag{2.19}
$$

with $0 \leq \mu^2 \leq 1 - y$.

Angular distributions

Top quarks will in general be polarized through their electroweak production mechanism. For unpolarized beams and close to threshold their polarization is given by the right/left asymmetry which would be measured with longitudinally polarized beams [118]:

$$
P_t = A_{RL} \tag{2.20}
$$

For fully longitudinally polarized electron (and unpolarized positron) beams the spin of both t and $\bar{t}$ is aligned with the spin of the e^-. Quark polarization then leads to angular distributions of the decay products which allow for various tests of the chirality of the tbW vertex.

The angular distribution of the longitudinal and transverse W's is analogous to those of ρ mesons from τ decay $(m_\tau \to m_t, m_\rho \to m_W)$

$$
\begin{aligned}
\frac{dN_{T/L}}{d\cos\theta} &= \frac{1}{2}(1 \mp P_t \cos\theta) \\
\textit{for} \quad h_W &= \left\{ \begin{pmatrix} +1 \\ 0 \end{pmatrix} \right.
\end{aligned} \tag{2.21}
$$

and, after summation over the W polarizations

$$\frac{dN}{d\cos\theta} = \frac{1}{2}\left(1 + \frac{m_t^2 - 2m_W^2}{m_t^2 + 2m_W^2} P_t \cos\theta\right) \tag{2.22}$$

The angle between top quark spin and direction of the W is denoted by θ.

For an arbitrary admixture of right- and lefthanded couplings (and neglecting m_b)

$$P_t \to \left(w_L^2 - w_B^2\right) P_t \tag{2.23}$$

The angular distribution of leptons from the chain $t \to b + W(\to \ell^+\nu)$ will in general follow a complicated pattern with an energy dependent angular distribution

$$\frac{dN}{dx d\cos\theta} = f(x) + g(x) P_t \cos\theta \tag{2.24}$$

In the SM, however, a remarkable simplification arises. Energy and angular distribution factorize [118, 119]

$$\frac{dN}{dx d\cos\theta} = f(x)(1 + P_t \cos\theta)/2 \tag{2.25}$$

This factorization holds true for arbitrary m_t and even including the effect of the nonvanishing b-quark mass. For righthanded tb coupling, however,

$$\frac{dN}{dx d\cos\theta} = f_+(x) + g_+(x) P_t \cos\theta \tag{2.26}$$

with f_+ as given in (2.16) and [119]

$$\begin{aligned} \frac{g_+}{f_+} &= \frac{2y}{(1+y-x)x} - 1 \\ &= \begin{cases} 1 & \text{for } x = y \text{ or } 1 \\ \frac{8y}{(1+y^2)} - 1 & \text{for } x = (1+y)/2 \end{cases} \end{aligned} \tag{2.27}$$

Even after including QCD corrections [119, 120] the spectrum of both charged lepton and neutrino can be cast into the form

$$\frac{\mathrm{d}N}{\mathrm{d}x \mathrm{d}\cos\theta} = A(x) + B(x)\cos\theta \tag{2.28}$$

The shape of the charged lepton spectrum is hardly different from the lowest order result [119] with main corrections towards the end point. $B_e(x) \approx A_e(x)$ remains valid to extremely high precision [120]. The charged lepton direction is thus a perfect analyser of the top spin, even after inclusion of QCD corrections. A small admixture of $V + A$ couplings will affect spectrum and angular distributions of electron and neutrino as well. Assuming a $V + A$ admixture of relative rate $\kappa^2 = 0.1$, the functions

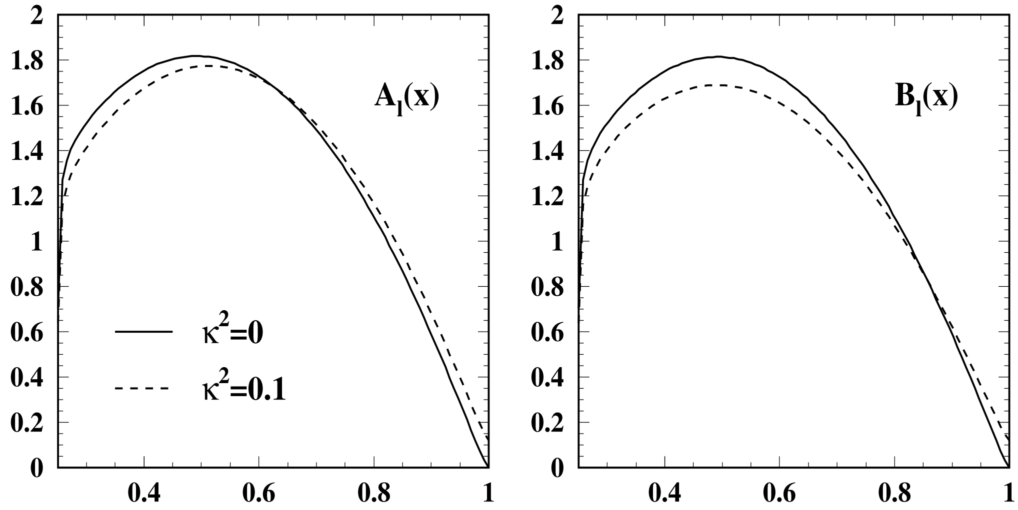

Figure 2.5: *The coefficient functions a)* $\mathrm{A}_\ell(x)$ *and b)* $\mathrm{B}_\ell(x)$ *defining the charged lepton angular-energy distribution for* $y = 0.25$ *and* $\alpha_s(m_t) = 0.11$ *:* $\kappa^2 = 0$ *– solid lines and* $\kappa^2 = 0.1$ *– dashed lines (from [121]).*

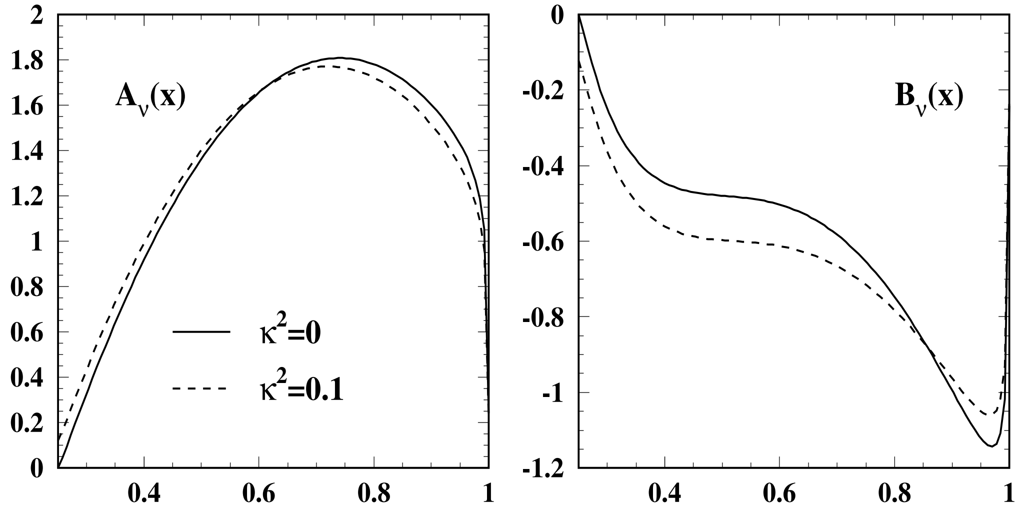

Figure 2.6: *The coefficient functions a)* $\mathrm{A}_\nu(x)$ *and b)* $\mathrm{B}_\nu(x)$ *defining the neutrino angular-energy distribution for* $y = 0.25$ *and* $\alpha_s(m_t) = 0.11$ *:* $\kappa^2 = 0$ *– solid lines and* $\kappa^2 = 0.1$ *– dashed lines (from [121]).*

A_e, B_e and A_ν are only marginally modified (Fig. 2.5 and 2.6). The angular dependent part of the neutrino spectrum B_ν, however, is changed significantly (Fig. 2.6). This observation [121] could provide a useful tool in the search for new couplings [122].

To summarize: $V-A$ and $V+A$ currents lead to drastically different predictions. However, a small admixture of $V+A$ will be difficult to detect as a consequence of the incoherent addition of right- and lefthanded amplitudes.

2.2.2 Radiative corrections

Perturbative corrections to the lowest-order result affect the total decay rate as well as differential distributions. Their inclusion is a necessary prerequisite for any analysis that attempts a precision analysis of top decays. Both QCD and electroweak corrections are well under control and will be discussed in the following.

QCD corrections

The correction to the decay rate is usually written in the form

$$\Gamma = \Gamma_{Born}\left(1 - \frac{2}{3}\frac{\alpha_s}{\pi} f\right) \tag{2.29}$$

The correction function f has been calculated in [123] for nonvanishing and vanishing b mass. In the limit $m_b^2/m_t^2 \to 0$ the result simplifies considerably, but remains a valid approximation:

$$\begin{aligned} f &= \mathcal{F}_1/\mathcal{F}_0 \\ \mathcal{F}_0 &= 2(1-y)^2(1+2y) \\ \mathcal{F}_1 &= \mathcal{F}_0\left[\pi^2 + 2Li_2(y) - 2Li_2(1-y)\right] \\ &\quad +4y(1-y-2y^2)\ln y + 2(1-y)^2(5+4y)\ln(1-y) \\ &\quad -(1-y)(5+9y-6y^2) \end{aligned} \tag{2.30}$$

where $y = m_W^2/m_t^2$. This formula was confirmed in [124]. In the limit $m_t^2 >> m_W^2$ f approaches the value $f(0) = 2/3\pi^2 - 5/2 \approx 4$. For $m_t \approx 175$ GeV the QCD correction amounts to

$$\delta_{QCD} \approx 3.7\alpha_s/\pi \tag{2.31}$$

and lowers the decay rate by about 10%. This has a non-negligible impact on the height and width of a toponium resonance or its remnant.

The complete α_s^2 corrections are presently unknown, and the scale μ in $\alpha_s(\mu^2)$ is uncertain. Indications for a surprisingly large correction of order α_s^2, corresponding to a rather small scale have been obtained. Diagrams with light fermion insertions into the gluon propagator have been calculated numerically [125] and analytically [126] in the limit $m_t \gg M_W$

$$\begin{aligned}\Gamma &= \Gamma_{\rm Born}\left[1-\frac{2}{3}\frac{\alpha_{\overline{\rm MS}}(m_t^2)}{\pi}\left(4\zeta_2-\frac{5}{2}\right)\right.\\&\left.+\left(\frac{\alpha_{\overline{\rm MS}}}{\pi}\right)^2\left(-\frac{2n_f}{3}\right)\left(\frac{4}{9}-\frac{23}{18}\zeta_2-\zeta_3\right)\right]\end{aligned} \tag{2.32}$$

The BLM prescription [127] suggests that the dominant α_s^2 coefficients can be estimated through the replacement

$$-\frac{2n_f}{3}\rightarrow\left(11-\frac{2n_f}{3}\right) \tag{2.33}$$

and absorbed through a change in the scale. For the problem at hand this corresponds to a scale $\mu = 0.122m_t$ resulting in a fairly large effective value of α_s of 0.15 instead of 0.11 for $\mu = m_t$. The applicability of the BLM recipe has been verified for the $b \rightarrow c$ transitions at the points of maximal and of minimal recoil [128, 129].

The δ spike in the energy distribution of the hadrons from the decay $t \rightarrow b + W$ is smeared by quark fragmentation (not treated in this context).

Hard gluon radiation leads to a slight shift and distortion of the energy spectra with a tail extending from the lower limit given by two-body kinematics upwards to $m_t - m_W$

$$\frac{m_t^2+m_b^2-m_W^2}{2m_t}\le E_{had} < m_t - m_W \tag{2.34}$$

Including finite W-width effects and $m_b \neq 0$ the differential hadron energy (and W energy) distribution has been calculated in [130]. The hadron energy distribution is shown in Fig.2.7 for $m_t = 180\ GeV$.

The lepton spectrum (as well as the neutrino spectrum) receives its main correction close to the end points where the counting rates are fairly low. The shape is hardly different from the lowest-order result [119].

Results for the corrected angular distributions of charged leptons and neutrinos from the decay of polarized t quarks are also available in the literature [120]. It has been shown that the deviations from the factorizable form (2.25) are below 10^{-3} such that the Born approximation is well justified for this purpose.

Electroweak corrections

Electroweak corrections to the top quark decay rate can be found in [124, 131]. They involve a large number of diagrams. For asymptotically large top masses the Higgs exchange diagram depicted above, provides the dominant contribution. Defining the Born term by means of the Fermi coupling G_F, one derives in this limit

$$\Gamma = \Gamma(G_F)_{BORN}\left[1+\delta_{EW}\right] \tag{2.35}$$

$$\delta_{EW} = \frac{G_F m_t^2}{4\sqrt{2}\pi^2}\left[\frac{17}{4}+\log\frac{m_H^2}{m_t^2}\right] + \text{subleading terms}$$

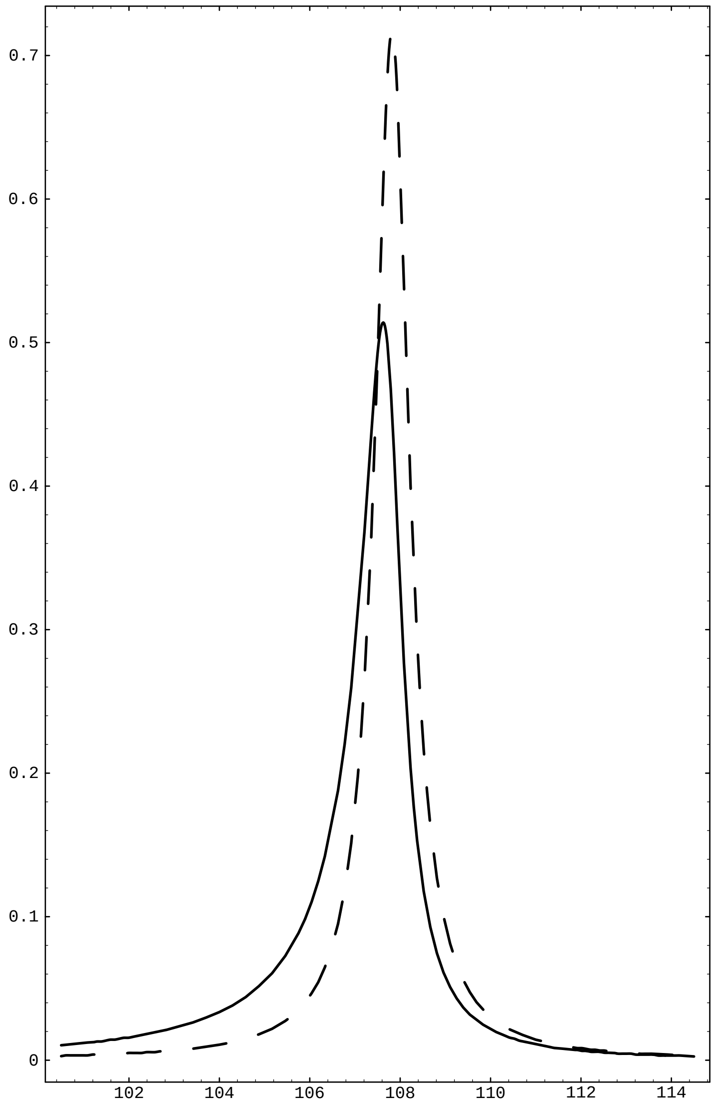

Figure 2.7: *Normalized distribution of the W energy for* $m_t = 180$ *GeV without (dashed) and with (solid curve) QCD corrections.*

While the Higgs–top coupling is the origin of the strong quadratic dependence on the top mass, the Higgs itself is logarithmically screened in this limit. However, the detailed analysis reveals that the subleading terms are as important as the leading terms so that finally we observe only a very weak dependence of δ_{EW} on the top and the Higgs masses. The numerical value of the corrections turns out to be small, $\delta_{EW} \approx +2\%$. Electroweak corrections in the context of the two Higgs doublet model can be found in [132] and are of comparable magnitude.

The positive correction δ_{EW} is nearly cancelled by the negative correction δ_Γ of -1.5% from the nonvanishing finite width of the W. The complete prediction taken from [133] is displayed in table 2.1 for the choice $\alpha_s(\mu^2 = m_t^2)$. For $\mu = 0.112 m_t$ the

m_t [GeV]	$\alpha_s(m_t)$	$\Gamma^{\rm Born}_{\rm nar.w.}$ [GeV]	$\delta_\Gamma^{(0)}$ [%]	$\delta^{\rm nw}_{\rm QCD}$ [%]	$\delta_{\rm EW}$ [%]	Γ [GeV]
170	.108	1.41	-1.52	-8.34	1.67	1.29
180	.107	1.71	-1.45	-8.35	1.70	1.57
190	.106	2.06	-1.39	-8.36	1.73	1.89

Table 2.1: *Top width as a function of top mass and the comparison of the different approximations.*

QCD correction amounts to -11.6 % instead of -8.3%. This variation characterises the present theoretical uncertainty, which could be removed by a full α_s^2 calculation only. Additional uncertainties, e.g. from the input value of α_s ($\sim 1\%$) or from the fundamental uncertainty in the relation between the pole mass m_t and the experimentally measured excitation curve (assuming perfect data) of perhaps 0.5 GeV can be neglected in the forseable future.

Hence, it appears that the top quark width (and similarly the spectra to be discussed below) are well under theoretical control, including QCD and electroweak corrections. The remaining uncertainties are clearly smaller than the experimental error in Γ_t, which will amount to 5-10% even at a linear collider.

2.2.3 Non–standard top decays

The theoretical study of non–standard top decays is motivated by the large top quark mass which could allow for exciting novel decay modes, even at the Born level. A few illustrative, but characteristic examples will be discussed in some detail in the following chapters.

Charged Higgs decays

Charged Higgs states $H^\pm$ appear in 2–doublet Higgs models in which, out of the eight degrees of freedom, three Goldstone bosons build up the longitudinal states of the vector bosons and three neutral and two charged states correspond to real physical particles. A strong motivation for this extended Higgs sector is provided by supersymmetry which requires the Standard Model Higgs sector to be doubled in order to generate masses for the up and down–type fermions. In the minimal version of that model, the masses of the charged Higgs particles are predicted to be larger than the W mass, mod. radiative corrections,

$$m(H^{\pm}) > m(W^{+}) \text{ [mod. rad. corr.]}$$

We shall adopt this specific model for the more detailed discussion in the following paragraphs.

If the charged Higgs mass is lighter than the top mass, the top quark may decay into H^+ plus a b quark [134],

$$t \to b + H^{+}$$

The coupling of the charged Higgs to the scalar (t, b) current is defined by the quark masses and the parameter $\tan\beta$,

$$J(b,t) = \sqrt{\frac{G_F}{\sqrt{2}}}\,[(m_b \tan\beta + m_t \cot\beta) - \gamma_5\,(m_b \tan\beta - m_t \cot\beta)] \tag{2.36}$$

The parameter $\tan\beta$ is the ratio of the vacuum expectation values of the Higgs fields giving masses to up and down–type fermions, respectively. For the sake of consistency, related to grand unification, we shall assume $\tan\beta$ to be bounded by

$$1 < \tan\beta = \frac{v_2}{v_1} < \frac{m_t}{m_b} \sim 50 \tag{2.37}$$

with $v = \sqrt{v_1^2 + v_2^2}$ corresponding to the ground state of the Standard Model Higgs field. The width following from the coupling (2.36) has a form quite similar to the Standard Model decay mode [see e.g. [66]],

$$\Gamma(t \to b + H^{+}) = \frac{G_F m_t^3}{8\sqrt{2}\pi}\left[1 - \frac{m_H^2}{m_t^2}\right]^2 \left[\left(\frac{m_b}{m_t}\right)^2 \tan^2\beta + \cot^2\beta\right] \tag{2.38}$$

The branching ratio of this novel Higgs decay mode is compared with the W decay mode in Fig.2.8a. In the medium $\tan\beta$ range the W decay mode is dominant; the Higgs decay branching ratio is in general small, yet large enough, in particular for small $\tan\beta \gtrsim 1$ and large $\tan\beta \lesssim m_t/m_b \sim 50$, to be clearly observable [6].

The detection of this scalar decay channel is facilitated by the characteristic decay pattern of the charged Higgs bosons

$$H^{+} \to \tau^{+} + \nu_\tau \quad \text{and} \quad c + \bar{s}$$

into *SM* particles. Since $H^{\pm}$ bosons couple preferentially to down–type fermions [135] for $\tan\beta > 1$,

$$\Gamma(H^{+} \to \tau^{+}\nu_\tau) \;=\; \frac{G_F m_\tau^2}{\sqrt{2}}\frac{m_H}{4\pi}\tan^2\beta \tag{2.39}$$

$$\Gamma(H^{+} \to c\bar{s}) \;=\; \frac{3G_F m_c^2}{\sqrt{2}}\frac{m_H}{4\pi}\left[\left(\frac{m_s}{m_c}\right)^2 \tan^2\beta + \cot^2\beta\right] \tag{2.40}$$

Figure 2.8: **(a)** *Branching ratios for the decays* $t \to bW^+$ *and* $t \to bH^+$ *in two–doublet Higgs models.*

Figure 2.8: **(b)** *Branching ratios for charged Higgs decays to* τ *leptons and quarks.*

Figure 2.8: **(c)** *Inclusive branching ratios for $t \to l + X$ in two–doublet Higgs models and breaking of the lepton universality. $BR_l(t) = 1/9$ in the Standard Model is indicated by the broken line.*

the τ decay mode wins over the quark decay mode [Fig.2.8b], thus providing a clear experimental signature. A first signal of top decays into charged Higgs particles would therefore be the breakdown of μ, e *vs.* τ universality in semileptonic top decays, Fig.2.8c. Other possible decay modes of charged Higgs bosons, in particular chargino/neutralino decays for small $\tan\beta$, also lead to characteristic final states.

Top decay to stop

Another exciting decay mode in supersymmetry models is the decay of the top quark to the SUSY scalar partner stop plus neutralinos, mixtures of neutral gauginos and higgsinos [136, 137]. This possibility is intimately related to the large top mass which leads to novel phenomena induced by the strong Yukawa interactions. These effects do not occur in light–quark systems but are special to the top (and eventually the bottom) system.

The mass matrix of the scalar SUSY partners $(\tilde{t}_L, \tilde{t}_R)$ to the left– and right–handed top–quark components (t_L, t_R) is built up by the following elements [138]

$$\mathcal{M}^2 = \left\| \begin{array}{cc} m^2_{\tilde{t}_L} + m_t^2 + (\frac{1}{2} - \frac{2}{3}s_w^2)\cos 2\beta m_Z^2 & \delta\tilde{m}^2_{LR} \\ \delta\tilde{m}^2_{LR} & m^2_{\tilde{t}_R} + m_t^2 + \frac{2}{3}s_w^2 \cos 2\beta m_Z^2 \end{array} \right\|$$

Large Yukawa interactions mix the $\tilde{t}_L$ and $\tilde{t}_R$ states with the strength $\sim m_t$ to form the mass eigenstates $\tilde{t}_1, \tilde{t}_2$. Unlike the five light quark species, these Yukawa interactions of $\mathcal{O}(m_t)$ can be so large in the top sector that after diagonalizing the mass matrix, the smaller eigenvalue may drop below the top quark mass,

$$m_{\tilde{t}_1} < m_t \quad [\; : \text{possible} \;]$$

The decay modes

$$t \to \tilde{t} + \text{neutralinos}$$

then compete with the ordinary W decay mode. Identifying the lightest SUSY particle with the photino $\tilde{\gamma}$, for example, the mass of which we neglect in this estimate,

$$\frac{\Gamma(t \to \tilde{t}\tilde{\gamma})}{\Gamma(t \to bW)} \approx \frac{8\sqrt{2}\pi\alpha}{9G_F m_t^2} \frac{[1 - m_{\tilde{t}}^2/m_t^2]^2}{[1 - m_W^2/m_t^2]^2[1 + 2m_W^2/m_t^2]} \tag{2.41}$$

This ratio is in general less than 10%. The subsequent $\tilde{t}$ decays

$$\begin{aligned} \tilde{t} &\to b\tilde{W}, \tilde{W} \to W\tilde{\gamma} \;\; \text{or} \;\; l\tilde{\nu} \;\; etc. \\ \tilde{t} &\to c\tilde{\gamma} \end{aligned}$$

lead to an overall softer charged lepton spectrum and, as a result of the escaping photinos, to an increase of the missing energy, the characteristic signature for SUSY induced phenomena [6, 139].

FCNC decays

Within the Standard Model, FCNC decays like $t \to c\gamma$ are forbidden at the tree level by the GIM mechanism. However, they do occur in principle at the one–loop level, though strongly suppressed. The suppression is particularly severe for top decays since the quarks building up the loops, must be down–type quarks with m_b^2 setting the scale of the decay amplitude, $\Gamma_{FCNC} \sim \alpha G_F^2 m_b^4 m_t$. A sample of branching ratios is given below [140]:

$$\begin{aligned} BR(t \to cg) &\sim 10^{-10} & \qquad BR(t \to cZ) &\sim 10^{-12} \\ BR(t \to c\gamma) &\sim 10^{-12} & \qquad BR(t \to cH) &\sim 10^{-7} \end{aligned}$$

At this level, the FCNC t decays generated by the Standard Model cannot be observed, even given millions of top quarks in proton colliders. On the other hand, if these decay modes were detected, they would be an undisputed signal of new physics beyond the Standard Model. From such options we select one illustrative, though very speculative example for brutal GIM breaking. It is tied to the large top mass and holds out faint hopes to be observable even in low rate e^+e^- colliders.

The GIM mechanism requires all L and R quark components of the same electric charge in different families to carry identical isospin quantum numbers, respectively. This rule is broken by adding quarks in LR symmetric vector representations [141] to the "light" chiral representations or mirror quarks [142]:

$$\underline{\text{vector quarks:}} \qquad \cdots \quad \begin{bmatrix} t \\ b \end{bmatrix}_L \quad \begin{matrix} t_R \\ b_R \end{matrix} \qquad \begin{bmatrix} U \\ D \end{bmatrix}_L \begin{bmatrix} U \\ D \end{bmatrix}_R$$

$$\underline{\text{mirror quarks:}} \qquad \cdots \quad \begin{bmatrix} t \\ b \end{bmatrix}_L \quad \begin{matrix} t_R \\ b_R \end{matrix} \qquad \begin{matrix} U_L \\ D_L \end{matrix} \quad \begin{bmatrix} U \\ D \end{bmatrix}_R$$

Low energy phenomenology requires the masses M of the new U, D quarks to be larger than 300 GeV.

Depending on the specific form of the mass matrix, mixing between the normal chiral states and the new states may occur at the level $\sim \sqrt{m/M}$, so that FCNC (t, c) couplings of the order $\sim \sqrt{m_t m_c/M^2}$ can be induced. FCNC decays of top quarks, for example,

$$BR(t \to cZ) \sim \text{fraction of } \%$$

are therefore not excluded. Such branching ratios can easily be measured at the LHC.

Summa. For the illustrative examples outlined above, the Standard Model decay mode $t \to b + W^+$ is in general dominant so that t quarks can be tagged easily. Non–standard decays are correspondingly rare, yet frequent enough to be detected in mixed Standard Model – non–Standard Model $t\bar{t}$ pair decays at e^+e^- colliders. Very rare decay modes, in particular FCNC decays with clear signatures, can be investigated at the LHC.

2.3 Top quarks in hadron colliders

Searching for new quarks and exploring their properties has been a most important task at hadron colliders in the past. The Tevatron proton-antiproton collider is the only machine in which top quarks have been produced so far. The high energy collider LHC is needed to provide the large number of events [order 10^7] for a detailed study of the top quark properties.

The main production mechanisms for top quarks in proton-antiproton collisions, Fig.2.9, are gluon-gluon and quark-antiquark fusion [143]

$$gg \text{ and } q\bar{q} \to t\bar{t}.$$

W–gluon fusion [144]

$$Wg \to t\bar{b}$$

is an interesting weak process that will allow us to measure the tbW coupling.

Figure 2.9: *The main production mechanisms for top quarks in $p\overline{p}$ and pp colliders [generic diagrams].*

2.3.1 Hadronic fusion mechanism

The dominant Born terms of the total cross section for top–pair production in $gg/q\overline{q} \to t\bar{t}$ fusion are well-known to be of the form [143]

$$\sigma_{gg}(\hat{s}) = \frac{4\pi\alpha_s^2}{12\hat{s}} \left[(1+\rho+\frac{\rho^2}{16}) \ln\frac{1+\beta}{1-\beta} - \beta\,(\frac{7}{4}+\frac{31}{16}\rho) \right] \tag{42a}$$

$$\sigma_{q\overline{q}}(\hat{s}) = \frac{8\pi\alpha_s^2}{27\hat{s}}\,\beta\,[1+\frac{\rho}{2}] \tag{42b}$$

with $\rho = 4m_t^2/\hat{s}$ and $\beta = \sqrt{1-\rho}$ being the velocity of the t quarks in the $t\bar{t}$ cm frame with invariant energy $\sqrt{\hat{s}}$. The total pp cross sections then follow by averaging the partonic cross sections over the $q\overline{q}$ and gg luminosities in pp collisions,

$$\sigma\,(pp\to\, t\bar{t}) = \int_{4m_t^2/s}^{1} d\tau\, \frac{d\mathcal{L}\,(gg)}{d\tau} \sigma_{gg}\,(\tau s) + [q\overline{q}] \tag{2.43}$$

Since the parton luminosities rise steeply for $\tau \to 0$, the $t\bar{t}$ production cross sections, increase dramatically with rising energy.

Higher-order QCD corrections [145], [146] include loop corrections to the Born terms and $2 \to 3$ contributions like $gg \to t\bar{t}g$, $q\bar{q} \to t\bar{t}g$ etc. The integrated expressions for the total cross sections can still be cast into a simple form

$$\sigma_{ij}(\hat{s}, m_t^2, \mu^2) = \frac{\alpha_s^2(\mu^2)}{m_t^2} \left[f_{ij}^{(0)}(\rho) + 4\pi\alpha_s(\mu^2) \left(f_{ij}^{(1)}(\rho) + \bar{f}_{ij}^{(1)}(\rho) \ln \frac{\mu^2}{m_t^2} \right) \right] \tag{2.44}$$

where $\hat{s} = x_1 x_2 s$ and the dominant lowest-order contributions $f_{ij}^{(0)}(\rho)$ are given by the parton cross sections above; in addition $f_{gq}^{(0)} = f_{g\bar{q}}^{(0)} = 0$. The subleading higher-order expressions for $f_{ij}^{(1)}$ and $\bar{f}_{ij}^{(1)}$ are given in Refs.[145], [146]. The heavy quarks are treated within the on-shell renormalization scheme with m_t being the "physical" mass of the top quark. Outside the heavy quark sector, the $\overline{MS}$ scheme has been employed. These higher-order terms have to be used in conjunction with the running coupling $\alpha_s(\mu^2)$ and the gluon/light-quark parton densities evolved in 2-loop evolution equations. μ is the renormalization scale, identified here also with the factorization scale; typical scales that have been chosen are $\mu = m_t$ and $\sqrt{m_t^2 + p_T^2}$. More technical details are discussed in Ref.[12]. The subdominant $2 \to 3$ contributions add up to less than 10% of the dominant lowest-order results.

It is also instructive to study separate, physically distinct components of the α_s^3 results [147]. Whereas the initial (final) state bremsstrahlung (ISGB) processes, illustrated for the gluon initiated reactions in Fig.2.10, dominate around threshold $[\sqrt{\hat{s}} \geq 2m_t$ or $p_t < m_t)]$, the gluon splitting (GS) and the flavor excitation (FE) contributions become equally important for $\sqrt{\hat{s}} \gg 2m_t$ or $p_t \geq m_t$.

Figure 2.10: *Generic QCD diagrams of the dominant higher order mechanisms.*

Near the $t\bar{t}$ threshold the cross sections are affected by resonance production and Coulomb rescattering forces [66], [148], [149]. These corrections can be estimated in a simplified potential picture. The driving 1-gluon exchange potential is attractive if the $t\bar{t}$ is in color-singlet state and repulsive in a color-octet state [149],

$$\begin{aligned} \sigma^{(1)}(gg \to t\bar{t}) &= \frac{2}{7}\, \sigma_B(gg \to t\bar{t})\, |\Psi^{(1)}|^2 \\ \sigma^{(8)}(gg \to t\bar{t}) &= \frac{5}{7}\, \sigma_B(gg \to t\bar{t})\, |\Psi^{(8)}|^2 \end{aligned} \tag{2.45}$$

$$\sigma^{(8)}(q\bar{q}\to t\bar{t}) \quad = \quad \sigma_B(q\bar{q}\to t\bar{t})\,|\,\Psi^{(8)}\,|^2$$

The Coulombic attraction leads to a sharp rise of the cross section at the threshold in the singlet channel, even if no resonance can be formed anymore, since the phase space suppression of the Born term $\sigma_B \propto \beta_t$ is neutralized by the Coulomb enhancement of the wave function $|\Psi_1|^2 \propto \alpha_s/\beta$. In the octet channel, by contrast, the cross sections are strongly reduced by the Coulombic repulsion which leads effectively to an exponential fall-off of the cross sections $\sigma_8 \propto \exp\left[-\pi\alpha_s/6\beta_t\right]$ at the threshold. Due to the averaging over parton luminosities [149] the effects are less spectacular in pp than in e^+e^- collisions.

The calculation of the production cross section for top pairs can be refined by summing up the radiation of infrared gluons in the initial state. These effects are large in the threshold region. Various algorithmic techniques have been developed to approach this problem. Either a cut–off scale (CS) is introduced [150] at which the infrared radiation is stopped, or principle–value (PVR) techniques are adopted [151, 152] to perform the resummation. Even if the method is fixed, there are still non–negligible uncertainties due to the cut–off choice and due to different algorithmic approaches.

In addition to the uncertainties in resummation techniques, the theoretical predictions depend on the error in α_s, the specific choice of the renormalization and factorization scales near $\mu \sim m_t$, and to a lesser extent on the parton distributions. The size of the uncertainties may be estimated from the spread of the theoretical predictions which appears to be of order 20%.

Genuine electroweak contributions of $\mathcal{O}\left(\alpha\alpha_s^2\right)$ have been calculated to both the $q\bar{q}$ and $gg\to t\bar{t}$ subprocesses [153]. The corrections include vertex corrections and box diagrams built-up by the electroweak vector bosons and the Higgs boson. Except for a small region close to the production threshold, the corrections are always negative. After convoluting the cross sections of the subprocesses with the parton distributions, a reduction of the Born cross section at a level of 10% is expected.

Recent results for the cross sections $\sigma(p\bar{p}\to t\bar{t})$ at the Tevatron and $\sigma(pp\to t\bar{t})$ at the LHC are summarized in Table 2.2. The resummation of infrared gluon radiation increases the cross section with respect to the fixed order α_s^3 prediction. With an integrated luminosity of $10^4 pb^{-1}$ in low–luminosity runs at the beginning of the LHC operation, about 10^7 top–quark pairs will be produced at this machine – a solid base for the first step of high–precision top analyses.

The final states in the fusion processes can be characterized by three observables. The average invariant energy $<\sqrt{\hat{s}}>$ of the $t\bar{t}$ pair is just a few m_t. The top production is central, $<y>=0$ with a spread $\Delta y = \pm 2$, the rapidity values where the cross section has fallen to 1/2 of its maximum. The distribution of the transverse momenta has its maximum value at $p_t^{max} \sim m_t/2$.

Method	$\sigma(p\bar{p} \to t\bar{t})$	$\sigma(pp \to t\bar{t})$	Ref.
NLO, fix ord.	$4.20^{+0.28}_{-0.54}$ nb		[154]
NLO, resum.	$4.94^{+0.71}_{-0.45}$ nb		[150]
NLO, resum.	$5.52^{+0.07}_{-0.45}$ nb		[151]
NLO, resum.	$4.75^{+0.63}_{-0.68}$ nb	$0.77^{+0.25}_{-0.12}$ nb	[152]

Table 2.2: *Theoretical predictions of the cross sections for $p\bar{p} \to t\bar{t}$ at the Tevatron, $\sqrt{s} = 1.8$ TeV, and for $pp \to t\bar{t}$ at the LHC, $\sqrt{s} = 14$ TeV, for $m_t = 175$ GeV.*

2.3.2 Wg Fusion to $t\bar{b}$

The interaction radius in the QCD gg fusion process shrinks with rising energy so that the cross section $\sigma(gg \to t\bar{t}\,) \sim \alpha_s^2/\hat{s}$ [mod. log's] vanishes asymptotically. By contrast, the interaction radius in the weak fusion process [144] is set by the Compton wave length of the W boson and therefore asymptotically non-zero, $\sigma \to G_F^2 m_W^2/2\pi$. Folding this subprocess with the quark-gluon luminosities, the fall-off of the total cross section $\sigma(pp \to t\bar{b})$ is less steep than for the QCD fusion processes. The Wg fusion process is suppressed at masses of order 175 GeV by about a factor five: $\sigma(Wg \to tb) \sim 100\,pb$. More than 10^6 top quarks will nevertheless be produced by this mechanism at an integrated luminosity of $\int \mathcal{L} = 10^4 pb^{-1}$.

A close inspection of the diagrams in Fig.2.10 reveals immediately that the by far dominant part of the cross section is due to b exchange, with the b quark being near its mass shell. Since the b quark is almost collinear to the incoming gluon, this cross section is logarithmically enhanced $\sim \ln(m_t^2/m_b^2)$ over other mechanisms. This naturally suggests to approximate the process by the subprocess $u + b \stackrel{W}{\to} d + t$ with the b-quark distribution generated perturbatively by gluon splitting based on massless evolution equations. The weak cross sections can be presented in a compact form,

$$\begin{aligned}
\sigma(ub \stackrel{W}{\to} dt) &= \frac{G_F^2 m_W^2}{2\pi}\,\frac{(\hat{s}\, - m_t^2)^2}{\hat{s}\,(\hat{s}\, + m_W^2 - m_t^2)} && \to \frac{G_F^2 m_W^2}{2\pi} \\
\sigma(d\bar{b} \stackrel{W}{\to} u\bar{t}) &= \frac{G_F^2 m_W^2}{2\pi}\left[1 + \frac{\hat{s}\,(2m_W^2 - m_t^2) - 2m_W^2 m_t^2}{\hat{s}^{\,2}}\right.
\end{aligned}$$

$$- \frac{(2\hat{s} \ + 2m_W^2 - m_t^2)m_t^2}{\hat{s}\ ^2} \log \frac{\hat{s} \ + m_W^2 - m_t^2}{m_W^2} \Bigg] \rightarrow \frac{G_F^2 m_W^2}{2\pi}$$

and identically the same expressions for the $\mathcal{C}$-conjugate reactions.

Top quarks are created in $u+g$ collisions, anti-top quarks in $d+g$ collisions where the absorption of a W^- transforms a $\bar{b}$ quark to a $\bar{t}$ quark. The naïve expectation from valence quark counting for the ratio of $t/\bar{t}$ cross sections, $\sigma(u \rightarrow t) : \sigma(d \rightarrow \bar{t}) \sim 2 : 1$ is corroborated by a detailed analysis. The cross section is reduced by an order of magnitude with respect to gluon fusion/quark–antiquark annihilation.

2.3.3 The discovery of the top quark and mass measurements

After first indications one year earlier, the experimental proof for the discovery of top quarks was delivered by the CDF collaboration [3] and the D0 collaboration early in 1995.

Top signals can be classified according to the number of isolated and non–isolated charged leptons in the final state. The CDF collaboration found 6 dilepton candidates with a background of 1.3 ± 0.3 events; moreover, they also found 37 events with tagged b quarks (see Fig.2.11), containing a W boson and at least 3 jets. Similarly, the D0 collaboration isolated 17 top candidate events with a background of 3.8 ± 0.6 events.

The reconstructed mass from CDF is shown in Fig.2.12. Combining the two measurements from CDF and D0 the present value of the top mass is given [108] by

$$m_t = 175.5 \pm 5.1 GeV$$

i.e. the t mass is known within an error of 3 percent. The production rate, Fig.2.13, coincides with the theoretical expectation for a top mass of ~ 175 GeV.

Several methods can be used to measure the top–quark mass in proton–(anti) proton collisions at the Tevatron and LHC quite accurately: (i) jjj recoil–mass measurements in 1–lepton events; (ii) The most precise measurement of the top mass can be performed by evaluating the (l^+l^-) invariant mass in trilepton events where l' and l^+ are isolated while l^- belongs to a b jet [155]. Since $\langle m\,(bl^+)\rangle \propto m_t$, with the coefficient determined by the invariant l^+l^- mass distribution and the $b \rightarrow l^-$ fragmentation function, this method is the least background-prone determination of the top mass [156]. Simulations for the LHC have shown that a precision of $\delta m_t = \pm 5\,\mathrm{GeV}$ can eventually be achieved. This number does not only match the accuracy from electroweak radiative corrections but it improves the precision by at least a factor of 2. If finally all methods are combined, a precision of $\delta m_t \approx 2$ to 3 GeV may be achieved.

Figure 2.11: *Candidate event for top–antitop production at the Tevatron from the CDF Collaboration, adopted from Ref. [108]. Both top quarks decay into a W–boson plus a bottom quark. The* W^+ *decays to* e^+ *plus an invisible neutrino, and the* W^- *decays into a quark and antiquark that show up as jets of hadrons.*

Figure 2.12: *Reconstructed mass distributions for the b–tagged* $W+ \geq 4-jet$ *events (solid), adopted from Ref. [108]. Also shown are the background shape (dotted) and the sum of background plus* $t\bar{t}$ *Monte Carlo for* $M_{top} = 175$ GeV/c^2 *(dashed), with the background constrained to the calculated value,* $6.9^{+2/5}_{-1/9}$ *events. The inset shows the likelihood fit used to determine the top mass. [CDF [3]].*

Figure 2.13: *Combined CDF and D0 cross–section and mass measurements, compared with the theoretical expection for ($p\bar{p} \to t\bar{t}$) as a function of top mass, derived in Ref.[150].*

2.4 Top quarks in the e^+e^- continuum

A variety of reactions is conceivable for top quark production at an electron positron collider. Characteristic Feynman diagrams are shown in Fig.2.14. e^+e^- annihilation through the virtual photon and Z (Fig.2.14a) dominates and constitutes the reaction of interest for the currently envisaged energy region.

In addition one may also consider [157] a variety of gauge boson fusion reactions (Fig.2.14b-d) that are in close analogy to $\gamma\gamma$ fusion into hadrons at e^+e^- machines of lower energy. Specifically these are single top production,

$$e^+e^- \to \bar{\nu}e^- t\bar{b} \tag{2.46}$$

or its charge conjugate and top pair production through neutral or charged gauge boson fusion

$$\begin{aligned} e^+e^- &\to e^+e^- t\bar{t} \\ e^+e^- &\to \bar{\nu}\nu t\bar{t} \end{aligned} \tag{2.47}$$

The experimental observation of these reactions would allow to determine the coupling of top quarks to gauge bosons, in particular also to longitudinal W bosons and Z bosons, in the space-like region and eventually at large momentum transfers. This would constitute a nontrivial test of the mechanism of spontaneous symmetry breaking.

The various cross sections increase with energy in close analogy to $\gamma\gamma$ reactions, and eventually even exceed e^+e^- annihilation rates. However, at energies accessible

Figure 2.14: *Feynman diagrams for $t\bar{t}$ or $t\bar{b}$ production in e^+e^- colliders.*

in the foreseeable future these reactions are completely negligible: for an integrated luminosity of $5 \cdot 10^{40} cm^{-2}$, at $E_{cm} = 500\ GeV$ and for $m_t = 150\ GeV$ one expects about five $e^+e^-t\bar{t}$ event (still dominated by $\gamma\gamma$ fusion). At that same energy the cross sections for $e^+\nu\bar{t}b + c.c.$ and $\nu\bar{\nu}t\bar{t}$ final states are still one to two orders of magnitude smaller.

Another interesting class of reactions is e^+e^- annihilation into heavy quarks in association with gauge or Higgs bosons:

$$e^+e^- \rightarrow t\bar{t}Z \tag{2.48}$$
$$e^+e^- \rightarrow t\bar{b}W^- \tag{2.49}$$
$$e^+e^- \rightarrow t\bar{t}H \tag{2.50}$$
$$e^+e^- \rightarrow t\bar{b}H^- \tag{2.51}$$

Two amplitudes contribute to the first reaction [158]: The $t\bar{t}$ system may be produced through a virtual Higgs boson which by itself was radiated from a Z (Fig.2.15). The corresponding amplitude dominates the rate and provides a direct measurement of the Yukawa coupling. The radiation of longitudinal Z's from the quark line in principle also carries information on the symmetry breaking mechanism of the theory. The transverse part of the $t\bar{t}Z$ coupling, i.e. the gauge part, can be measured directly through the cross section or various asymmetries in $e^+e^- \rightarrow t\bar{t}$. The longi-

Figure 2.15: *Amplitudes relevant for $e^+e^- \to t\bar{t}Z$ and for $e^+e^- \to t\bar{t}H$.*

tudinal part, however, could only be isolated with $t\bar{t}Z$ final states. For an integrated luminosity of $10^{41} cm^{-2}$ at $E_{CM} = 1$ TeV one expects only about 400 events (Fig.2.16) and it is therefore not clear whether these can be filtered from the huge background and eventually used for a detailed analysis.

Light Higgs bosons may be produced in conjunction with $t\bar{t}$ [159]. They are radiated either from the virtual Z with an amplitude that is present also for massless fermions or directly from heavy quarks as a consequence of the large Yukawa coupling. The latter dominates by far and may therefore be tested specifically with heavy quark final states. The predictions for the rate are shown in Fig.2.17. Depending on the mass of the Higgs and the top quark, the reaction could perhaps be detected with an integrated luminosity of $10^{41} cm^{-2}$ [160].

Top quark production in $\gamma\gamma$ collisions is conceivable at a "Compton collider". It requires special experimental provisions for the conversion of electron beams into well-focused beams of energetic photons through rescattering of laser light. This will be discussed in a separate part at the end of this section.

2.4.1 $e^+e^- \to t\bar{t}$

Born predictions

From the preceding discussion it is evident that the bulk of top studies at an e^+e^- collider will rely on quarks produced in e^+e^- annihilation [23] through the virtual γ and Z, with a production cross section of the order of σ_{point}. For quarks tagged at an angle ϑ, the differential cross section in Born approximation is a binomial in $\cos\vartheta$

$$\frac{d\sigma}{d\cos\vartheta} = \frac{3}{8}\left(1+\cos^2\vartheta\right)\sigma_U + \frac{3}{4}\sin^2\vartheta\sigma_L + \frac{3}{4}\cos\vartheta\sigma_F \qquad (2.52)$$

U and L denote the contributions of unpolarized and longitudinally polarized gauge bosons along the ϑ axis, and F denotes the difference between right and left polar-

Figure 2.16: *The Higgs mass (m_H) dependences of the total cross sections of* $e^+e^- \to t\bar{t}Z$ *for various top quark masses* m_t. *The c.m. energy* $\sqrt{s}$ *is set to be 500 GeV (a) and 1 TeV (b). (From [158].)*

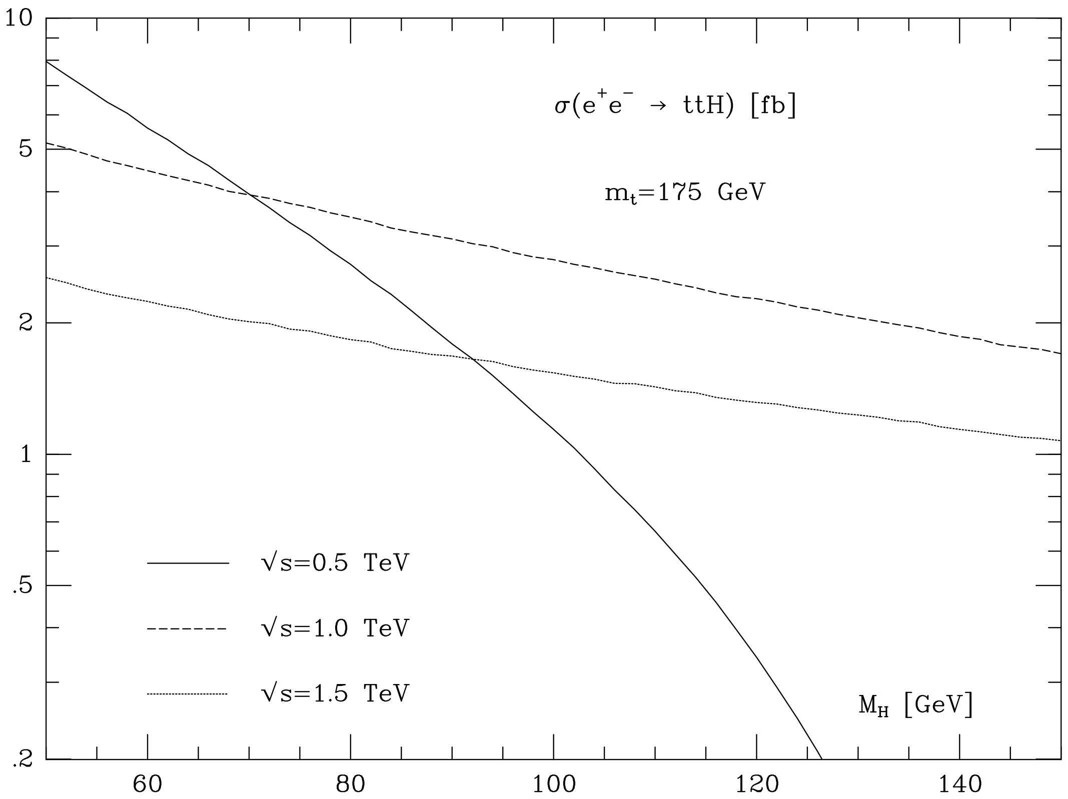

Figure 2.17: *The cross section $\sigma(e^+e^- \to t\bar{t}H)$ (from [159]).*

izations. The total cross section is the sum of U and L,

$$\sigma = \sigma_U + \sigma_L \tag{2.53}$$

the forward/backward asymmetry is given by the ratio

$$A^{FB} = \frac{3}{4}\frac{\sigma_F}{\sigma} \tag{2.54}$$

The σ^i can be expressed in terms of the cross sections for the massless case in Born approximation,

$$\begin{aligned} \sigma_B^U &= \beta\sigma^{VV} + \beta^3\sigma^{AA} \\ \sigma_B^L &= \frac{1}{2}\left(1-\beta^2\right)\beta\sigma^{VV} \\ \sigma_B^F &= \beta^2\sigma^{VA} \end{aligned} \tag{2.55}$$

with

$$\begin{aligned} \sigma^{VV} &= \frac{4\pi\alpha^2(s)e_e^2e_Q^2}{s} \\ &+\frac{G_F(s)}{\sqrt{2}}e_e e_Q(v_e+\rho a_e)v_Q\frac{m_Z^2\,(s-m_Z^2)}{(s-m_Z^2)^2+\left(\frac{s}{m_Z}\Gamma_Z\right)^2} \end{aligned}$$

$$
\begin{aligned}
& +\frac{G_F^2}{32\pi}\left(v_e^2+a_e^2+2\rho v_e a_e\right) v_Q^2 \frac{m_Z^4 s}{\left(s-m_Z^2\right)^2+\left(\frac{s}{m_Z}\Gamma_Z\right)^2} \\
\sigma^{AA} &= \frac{G_F^2}{32\pi}\left(v_e^2+a_e^2+2\rho v_e a_e\right) a_Q^2 \frac{m_Z^4 s}{\left(s-m_Z^2\right)^2+\left(\frac{s}{m_Z}\Gamma_Z\right)^2} \\
\sigma^{VA} &= \frac{G_F\alpha(s)}{\sqrt{2}} e_e(\rho v_e+a_e) e_Q a_Q \frac{m_Z^2\left(s-m_Z^2\right)}{\left(s-m_Z^2\right)^2+\left(\frac{s}{m_Z}\Gamma_Z\right)^2} \\
& +\frac{G_F^2}{16\pi}\left(2 v_e a_e+\rho(v_e^2+a_e^2)\right) v_Q a_Q \frac{m_Z^4 s}{\left(s-m_Z^2\right)^2+\left(\frac{s}{m_Z}\Gamma_Z\right)^2}
\end{aligned}
\tag{2.56}
$$

The fermion couplings are given by

$$
v_F = 2I_3^f - 4e_f \sin^2\theta_w \quad , \qquad a_f = 2I_3^f \tag{2.57}
$$

and the possibility of longitudinal electron polarization ($\rho = -1; +1; 0$ for right-handed; lefthanded; unpolarized electrons) has been included. In the subsequent numerical examples $G_F m_Z^2$ has been replaced by

$$
G_F m_Z^2 = \frac{\pi\alpha(s)}{\sqrt{2}\sin^2\theta_W \cos^2\theta_W} \tag{2.58}
$$

with $\sin^2\theta_W$ ($\approx$0.23) interpreted as $\sin^2\theta_{eff}$ [161] this formula accommodates the leading logarithms from the running coupling constant as well as the quadratic top mass terms in the threshold region. For $\alpha(s)$ we adopt [37]

$$
\begin{aligned}
1-\frac{\alpha}{\alpha(s)} &= \sum_\ell \frac{\alpha}{3\pi}\left(\ln\frac{s}{m_\ell^2}-\frac{5}{3}\right) \\
& +0.00165+0.003\ln(1+s/1\ GeV^2)
\end{aligned}
\tag{2.59}
$$

Radiative corrections

<u>QCD corrections</u> to this formula are available for arbitrary m^2/s up to first order in α_s:

$$
\begin{aligned}
\sigma &= \frac{(3-\beta^2)}{2}\beta\sigma^{VV}\left(1+\frac{4}{3}\frac{\alpha_s}{\pi}K_V\right) \\
& +\beta^3\sigma^{AA}\left(1+\frac{4}{3}\frac{\alpha_s}{\pi}K_A\right)
\end{aligned}
\tag{2.60}
$$

The exact result [162] for $K_{V,A}$ can be cast in the following form

$$
\begin{aligned}
K_V &= \frac{1}{\beta}\left[A+\frac{P_V}{(1-\beta^2/3)}\log\frac{1+\beta}{1-\beta}+\frac{Q_V}{(1-\beta^2/3)}\right] \\
K_A &= \frac{1}{\beta}\left[A+\frac{P_A}{\beta^2}\log\frac{1+\beta}{1-\beta}+\frac{Q_A}{\beta^2}\right]
\end{aligned}
\tag{2.61}
$$

$$
\begin{aligned}
A &= (1+\beta^2)\left[Li_2\left[\left(\frac{1-\beta}{1+\beta}\right)^2\right] + 2Li_2\left(\frac{1-\beta}{1+\beta}\right) + \log\frac{1+\beta}{1-\beta}\log\frac{(1+\beta)^3}{8\beta^2}\right] \\
&\quad +3\beta\log\frac{1-\beta^2}{4\beta} - \beta\log\beta \\
P_V &= \frac{33}{24} + \frac{22}{24}\beta^2 - \frac{7}{24}\beta^4 \\
P_A &= \frac{21}{32} + \frac{59}{32}\beta^2 + \frac{19}{32}\beta^4 - \frac{3}{32}\beta^6 \\
Q_V &= \frac{5}{4}\beta - \frac{3}{4}\beta^3 \\
Q_A &= -\frac{21}{16}\beta + \frac{30}{16}\beta^3 + \frac{3}{16}\beta^5
\end{aligned} \tag{2.62}
$$

QCD enhancement factors are well approximated by [163]

$$
\begin{aligned}
R_V &= 1 + \frac{4}{3}\alpha_s\left[\frac{\pi}{2\beta} - \frac{3+\beta}{4}\left(\frac{\pi}{2} - \frac{3}{4\pi}\right)\right] \\
R_A &= 1 + \frac{4}{3}\alpha_s\left[\frac{\pi}{2\beta} - \left(\frac{19}{10} - \frac{22}{5}\beta + \frac{7}{2}\beta^2\right)\left(\frac{\pi}{2} - \frac{3}{4\pi}\right)\right] \\
\alpha_s &= \frac{12\pi}{25\log(4p_t^2/\Lambda^2)}.
\end{aligned} \tag{2.63}
$$

Next to leading order corrections have been calculated recently for vector as well as axial current induced parts. Four contributions have to be considered separately in both cases:

i) A purely gluonic correction proportional C_F^2, denoted R_A, since it is equaly present in an abelian theory like QED. The threshold behaviour $\sim 1/\beta^2$ is a consequence of the Coulomb singularity and has to be absorbed in the Sommerfeld rescattering correction. ii) The corresponding nonabelian part proportional $C_F C_A$ is characteristic for the nonabelian group structure. For small β it is enhanced $\sim \ln\beta/\beta$; a consequence of the large QCD coupling close to threshold. These two parts have been evaluated through semianalytical methods [164, 165, 166]. The remaining two contributions iii) and iv) with a gluon split into a light or massive quark pair with a colour structure $\sim C_F T n_l$ and $C_F T$ are available in analytical and semianalytical form [167]. Top production in the continuum, from $2m_t$ plus about 10 GeV upwards is thus well under control.

For small β the leading (abelian) corrections can be obtained from Sommerfeld's rescattering formula ($x \equiv \frac{4}{3}\frac{\pi\alpha_s}{\beta}$)

$$
K_V^{Som} = \frac{x}{1-e^{-x}} = 1 + \frac{x}{2} + \frac{x^2}{12} - \frac{x^4}{720} + \dots \tag{2.64}
$$

To arrive at a reliable prediction close to threshold these terms have to be resummed. For β above ~ 0.2, corresponding to an energy roughly 10 GeV above the threshold, the fixed order calculation in NLO approximation is adequate, and for the following discussion even eq. 2.63 provides a valid approximation.

Initial state radiation has an important influence on the magnitude of the cross section. $\sigma(s_{eff})$ is folded with the Bonneau Martin structure function, supplemented by the summation of large logarithms. This leads to a significant suppression by about a factor

$$\left(\frac{\delta W}{m_t}\right)^\beta \approx 0.5 - 0.6 \tag{2.65}$$

with $\beta = \frac{2\alpha}{\pi}\left(\ln\frac{m_t^2}{m_e^2} - 1\right) = 0.12$ and $\delta W = 1 - 5\ GeV$ in the resonance and threshold region. The correction factor increases rapidly with energy, but stays below 0.9 in the full range under consideration (Fig.2.18).

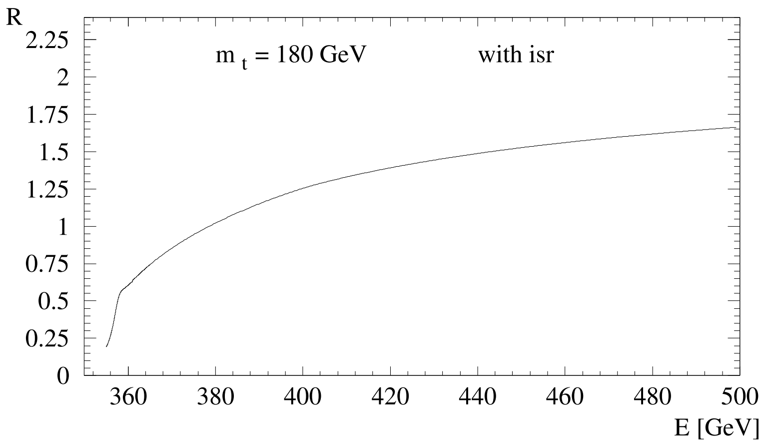

Figure 2.18: *Cross section for $t\bar{t}$ production, including resonances, QCD corrections and initial state radiation in units of σ_{point}.*

Electroweak corrections to the production cross section in the continuum have been studied in [168]. Apart from a small region close to threshold they are negative. Relative to the G_F parametrized Born approximation they decrease the cross section by about 7%, for m_H between 100 and 1000 GeV, and E_{cm} fixed at 500 GeV. For even larger energies the corrections decrease the $t\bar{t}$ cross section even further. This is partially compensated by Higgs and Z boson radiation. QCD and electroweak corrections are thus of equal importance.

Figure 2.19: *Genuine electroweak corrections to top production in e^+e^- annihilation. From [168].*

Close to threshold and for relatively small Higgs boson masses a rapid increase of these corretions is observed which can be attributed to the attractive Yukawa potential induced by light Higgs boson exchange. Several GeV above threshold, and for m_H around or below 100 GeV it is more appropriate to split these corrections into hard and soft exchange and incorporate the latter in an instantaneous Yukawa potential [169].

Longitudinal polarization

It should be mentioned that linear colliders might well operate to a large extent with polarized (electron) beams. The cross section for this case can be derived from (2.56). For top quarks the resulting right/left asymmetry

$$A_{LR} = (\sigma_L - \sigma_R)/(\sigma_L + \sigma_R) \tag{2.66}$$

is sizable and amounts to about -0.4, reducing the production cross section with righthanded electrons. However, selection of righthanded electron beams decreases the W pair cross section even stronger, thereby enhancing the top quark signal even before cuts are applied. Electroweak corrections to A_{LR} in the threshold region have been calculated in [170].

2.4.2 Top quark fragmentation

For $m_t \sim 175$ GeV, the strong–interaction fragmentation process and the weak decay mechanism are intimately intertwined. The lifetime $\tau_* < \Lambda^{-1}$ is so short that the mesonic $(t\bar{q})$ and baryonic (tqq) bound states cannot be built–up any more. Depending on the initial top quark energy, even remnants of the t quark jet may not form any more [66]. Hadrons can be created in the string stretched between the t and the $\bar{t}$ only if the quarks are separated by about 1 fermi before they decay. If the flight path $\gamma\tau_* < 1/2$ fm, i.e.

$$E < \frac{1}{2}\frac{m_t^4}{m_W^3} \tag{2.67}$$

the length of the $t - \bar{t}$ string is too short to form hadrons and jets cannot develop any more along the flight direction of the top quarks.

The perturbative radiation of soft gluons, too, is interrupted by the t quark decay [171]. The angular distribution (Θ) and the energy distribution (ω) of the radiated gluons is approximately given by

$$dP_g = \frac{4\alpha_s}{3\pi}\frac{\Theta^2 d\Theta^2}{\left[\Theta^2 + \frac{1}{\gamma^2}\right]^2 + \left[\frac{\Gamma}{\gamma\omega}\right]^2}\frac{d\omega}{\omega} \tag{2.68}$$

for a short–lived radiation source accelerated to $\gamma = E_t/m_t$. The gluons accumulate on the surface of a cone with half–aperture $\Theta_c \sim \gamma^{-1}$ for a long–lived t, but $\sim \gamma^{-1}\sqrt{\gamma\Gamma/\omega}$

if the particle decays quickly. The energy spectrum rises from zero to a maximum at $\omega \sim \gamma\Gamma$ before falling off $\sim 1/\omega$ for large ω, if the width is greater than the confinement scale Λ.

Top quarks are decelerated only by the early radiation of hard, non–collinear gluons. The non–zero t quark width Γ acts as an infrared cut–off for gluon radiation.

Neglecting the rare hard non–collinear gluon radiation, the flux tube forms between the b and $\bar{b}$ quarks after the decay of the top quarks, $e^+e^- \to t\bar{t} \to b\bar{b}W^+W^-$, if the top mass is so large that no t jet remnants are left–over. As a result, the light hadrons created in the flux tube, will be boosted into the $b\bar{b}$ hemisphere while the region opposite to the $b\bar{b}$ hemisphere will be depleted of particles [172]. This is demonstrated in Fig.2.20 where the distribution of the azimuthal angles of the final particles in the plane perpendicular to the $t\bar{t}$ direction is shown; the W bosons are assumed to decay leptonically in this event sample and the rapidity of the final particles is restricted to $|y| < 1$, with B decay products removed. The distribution of particles created in the $b\bar{b}$ string ["1–jet"] is clearly distinct from the distribution where the b and $\bar{b}$ flux lines are connected to the t and $\bar{t}$ fragments and three jets develop ["3–jet"].

2.4.3 Static t parameters

Because of the large t mass, deviations from the Standard Model may manifest themselves in the top quark sector first. Examples in which the large mass is crucial, are provided by multi–Higgs doublet models, models of dynamical symmetry breaking and compositeness. These effects can globally be described by form factors parametrizing the electroweak $t\bar{t}$ production current ($a = \gamma, Z$) and the weak (t, b) decay current ($a = -$) [173, 174, 175],

$$j^a_\mu \sim F^a_{1L}\gamma_\mu P_L + F^a_{1R}\gamma_\mu P_R + \frac{i\sigma_{\mu\nu}q_\nu}{2m_t}[F^a_{2L}P_L + F^a_{2R}P_R] \qquad (2.69)$$

[$P_{L,R}$ project on the left and right chirality components of the wave functions.] In the Standard Model, $F^-_{1L} = 1$ while all other F^-_i vanish; $F^\gamma_{1L} = F^\gamma_{1R} = 1$ and $F^\gamma_{2L} = F^\gamma_{2R} = 0$, analogously for the Z current. $\mathcal{CP}$ invariance requires $F^{\gamma,Z}_{2L} = F^{\gamma,Z}_{2R}$ in the $t\bar{t}$ production current, and equal phases for F^-_{1L} and F^-_{2R} *etc.* in the decay current. The static values of the form factors $F^{\gamma,Z}_2$ are the anomalous magnetic and electric dipole moments of the top quark.

The form factors are determined experimentally by measuring the angular distribution of the $t\bar{t}$ decay products, $e^+e^- \to t\bar{t}, t \to bW^+, W^+ \to f\bar{f}'$ *etc.* The corresponding helicity amplitudes have been given in Refs.[173, 174] at the quark level. This requires the top quark to be treated as a free particle, the polarization of which not being affected by non–perturbative hadronic binding effects. This assumption is justified by the short lifetime of the top quark as discussed earlier. While the general helicity analysis can be found in the literature [173, 174], we shall focus here on a few physically interesting specific examples.

Figure 2.20: *Distributions of the azimuthal angles of particles with* $|y| < 1$ *[B decay products removed], created in the* $b\bar{b}$ *flux tube (full curve) and in final states in which the* b *and* $\bar{b}$ *flux lines have been connected with* t *and* $\bar{t}$ *fragments (dashed curve);* $\sqrt{s} = 500$ *GeV, Ref.[172].*

Anomalous magnetic dipole moments of the top quark

If the electrons in $e^+e^- \to t\bar{t}$ are left–handedly polarized, the top quarks are preferentially produced as left–handed particles in the forward direction and only a small fraction is produced as right–handed particles in the backward direction. As a consequence of this Standard Model prediction, the backward direction is most sensitive to small anomalous magnetic moments of the top quarks. This is demonstrated quantitatively in Fig.2.21 where the angular distribution of the top quarks is broken down to the various helicity contributions. It is apparent that the anomalous magnetic moments can be bounded to a few percent through the measurement of the angular dependence of the t quark cross section. Also in a recent study [122] it is demonstrated that both production and decay distributions are sensitive probes of new physics, manisfest in production or decay vertices.

Figure 2.21: *Angular distributions of the t production cross sections for fixed t and $\bar{t}$ helicities in polarized $e_L^- e_R^+$ annihilation. The parameter δ measures the anomalous magnetic (γ, Z) dipole moment of the top quark. From Ref.[174].*

Electric dipole moments of the top quark

A term $\sim F_2 \sigma_{\mu\nu} q_\nu \gamma_5$ can only be generated in a $\mathcal{CP}$ non–invariant electromagnetic or Z interaction. The static limit $d^{\gamma,Z}$ of F_2 is the electric dipole moment of the top quark. Independently of the $\mathcal{CP}$ properties of the $t \to bW$ decay amplitude, such a contribution would be signalled by a non–zero expectation value of the $\mathcal{CP}$ odd momentum tensor [175]

$$T_{ij} = (q_+ - q_-)_i \frac{(q_+ \times q_-)_j}{|q_+ \times q_-|} \tag{2.70}$$

The greatest sensitivity is achieved by choosing the unit momentum vectors of the charged W–decay leptons for $q_\pm$

$$\langle T_{ij} \rangle = \frac{\sqrt{s}}{e} \left[c_\gamma d^\gamma + c_Z d^Z \right] \cdot \mathrm{diag} \left[-\frac{1}{6}, -\frac{1}{6}, +\frac{1}{3} \right] \tag{2.71}$$

where the coefficient c_γ, for instance, falls rapidly from zero at threshold to ~ -0.4 at $\sqrt{s} = 500$ GeV for $m_t = 150$ GeV. Correlations between $q_+ \times q_-$ and the initial

e^+e^- beam direction can be exploited to disentangle d^γ from d^Z. Sensitivity limits to the electric dipole moments are listed in the following table for a top mass $m_t = 150$ GeV and the integrated luminosity $\int \mathcal{L} = 10$ fb^{-1}:

$\sqrt{s}$	$d^{\gamma,Z}$
310 GeV	$< 7.0 \times 10^{-18}$ e cm
500 GeV	$< 2.8 \times 10^{-18}$ e cm

Other correlations, like $q_{e^+}[q_{e^+} \times q_b - q_{e^-} \times q_{\bar{b}}]$, and energy asymmetries can be defined that are sensitive to $\mathcal{CP}$ violation in the decay current [175] (see also Ref.[173]).

Normal polarization of the top quarks

A non–zero component of the t polarization vector that is normal to the production plane, can be generated only by the interference between complex helicity flip and non–flip amplitudes. Such relative phases can arise from $\mathcal{CP}$ violation but also from higher order loop corrections due to gluon exchange in the final state [56, 176, 173] or electroweak corrections involving Higgs and gauge bosons [173]. The QCD induced normal polarization is generally less than 2%, the electroweak normal polarization is smaller still.

[By contrast, longitudinal and transverse polarization components within the $t\bar{t}$ production plane are generated already at the tree level of the electroweak interactions and they are large in general; see [56] for the discussion of details.]

The polarization of the top quark is transmitted through the decay process to the polarization of the W boson. Since the b quark is always left–handedly polarized, the W emitted parallel to the t polarization vector, for instance, must be longitudinally polarized, while it is left–handedly polarized if emitted in the opposite direction. The W polarization reflects itself in the angular distribution of the charged decay lepton. As a result of the preceding discussion, the lepton l^+ in the decay chain $t \rightarrow bW^+ \rightarrow l^+\nu_l$ will the be emitted preferentially parallel to the t spin while the emission into the opposite direction is forbidden [118],

$$d\Gamma(\vec{s}_t) = d\Gamma_0 \cdot \tfrac{1}{2}(1 + \cos\theta_{l^+}) \tag{2.72}$$

This property is approximately preserved if radiative QCD corrections are taken into account [120].

Angular correlations of $t\bar{t}$ decay products

As stated in the previous chapter, top quarks are produced through the virtual photon and Z. In the threshold region they are polarized to a degree

$$P_t = A_{RL} \approx -0.4 \tag{2.73}$$

Assuming for the distribution of leptons from the decay of polarized top quarks

$$\frac{dN}{dx\, d\cos\theta} = f(x) + g(x) P_t \cos\theta \tag{2.74}$$

(with $g(x) = f(x)$ in the Standard Model, see eq.2.24) the angular distribution allows to test for the chirality of the tb current. Implicitly it was assumed that hadronization does not affect the top spin degrees of freedom [117, 178]. This assumption can be tested independently through the study of correlations between t and $\bar{t}$ decay products. In the threshold region the spins are correlated $\propto (1 + \frac{1}{3}\vec{s_+} \cdot \vec{s_-})$. This leads to the following correlated $\ell_+\ell_-$ distribution:

$$\frac{dN}{dx_+ dx_- d\cos\theta_{+-}} = f_+(x_+) f_-(x_-) + \frac{1}{3} g_+(x_+) g_-(x_-) \cos\theta_{+-} \tag{2.75}$$

where $f_+ = f_-$ and $g_+ = -g_-$. θ_{+-} denotes the angle between ℓ_+ and ℓ_-. After averaging the lepton energies,

$$\frac{dN}{d\cos\theta_{+-}} = 1 + \frac{1}{3} h_+ h_- \cos\theta_{+-} \tag{2.76}$$

Note that the coefficient of the correlation term is $-h_+^2/3$ and hence always negative (assuming CP conservation). Since $|h_+| \leq 1$ it ranges between 0 and $-1/3$. The limiting value $-1/3$ is assumed in the Standard Model. A detailed disussion with illustrative examples is given in [6].

2.4.4 Top quark production in $\gamma\gamma$ collisions

It has been repeatedly advocated [179] to convert an electron collider into a photon collider in order to have access with large luminosities to $C = +1$ final states. $\gamma\gamma$ fusion into a Higgs boson is one interesting possibility [180], W pair production leading to a variety of tests of the W magnetic moment is another one [181]. Here we will deal with $t\bar{t}$ production, which on the one hand could be considered to be a background to the other reactions, but could on the other hand allow the study of top quark couplings to real photons, a subject interesting in its own right.

Adjusting the helicities of incoming electron (P_e) and photon (P_γ) from the laser source appropriately ($2P_e P_\gamma = -1$), most of the electron energy is transferred to the scattered photon (Fig.2.22). The helicity of the scattered photon is dominantly flipped. Therefore, adjusting the two laser beams in an opposite helicity configuration (and the electron beams accordingly) one obtains a $\gamma\gamma$ configuration peaked at large energies (Fig.2.23) and dominantly in a state of helicity zero (Fig.2.24). Since the $t\bar{t}$ cross section close to threshold is dominated by the helicity zero configuration (Fig.2.25), one finds a large top cross section in the threshold region even after folding with the $\gamma\gamma$ luminosity for appropriately polarized electron and laser beams (Fig.2.26). For details see [182].

Figure 2.22: *Photon energy spectrum for different combinations of helicities of photons from the laser source and the electron beam ($E_\gamma = 1.26\ eV$, $E_e = 250\ GeV$) for collinear configuration.*

Figure 2.23: *$\gamma\gamma$ luminosities for unpolarized initial state (dashed) and for both laser beams and both electron beams polarized (solid).*

Figure 2.24: *Decomposition of the $\gamma\gamma$ luminosity into the non-flip (solid), single-flip (dashed), and double-flip (dotted) contribution for $h_{\gamma\gamma} = 0$ in the initial state and polarized beams.*

Figure 2.25: *Cross section for $\gamma\gamma \to t\bar{t}$ with polarized (solid, dashed) and unpolarized (dotted) photons.*

Figure 2.26: *Cross section for* $t\bar{t}$ *production in units of* σ_{point} *after folding with the* $\gamma\gamma$ *luminosity. Solid:* $2\lambda P = 2\tilde{\lambda}\tilde{P} = -1$. *Dashed:* $2\lambda P = 2\lambda\tilde{P} = 0$.

2.5 Threshold behaviour

The previous section dealt with top quark production sufficiently far above threshold for the reaction to be well described by the Born cross section, modified slightly by QCD and electroweak corrections. This is in contrast to the situation in the threshold region, where QCD plays an important role and controls the cross section. Strong forces modify the Born prediction. They compensate the phase space suppression and enhance the production rate significantly, leading to a step function like behaviour at threshold. The large top decay rate also plays an important role. Quarkonium resonances cease to exist and merge into a structureless excitation curve which joins smoothly with the continuum prediction above the nominal threshold.

This sharply rising cross section allows to study top quarks in a particularly clean environment and with large rates. The following physics questions can be addressed:

– The QCD potential can be scrutinized at short distances, with the non perturbative tail cut off by the top decay. As a result Λ_{QCD} or α_s could be determined accurately.
– The top quark mass can be measured with a precision which is only limited by the theoretical understanding of the excitation curve, but in any case better than 500 MeV.
– Top quarks are strongly polarized (about 40%) even for unpolarized beams; and longitudinal beam polarisation will enhance this value even further. Detailed studies of top decays, in particular of the $V-A$ structure of the tbW coupling are therefore feasible.
– The interquark potential is – slightly – modified by the Yukawa potential induced by Higgs exchange. The excitation curve and the top quark momentum distribution may therefore lead to an indirect measurement of the Yukawa coupling.
– The large number of top quarks in combination with the constrained kinematics at threshold could facilitate the search for new decay modes expected in extensions of the SM.

With this motivation in mind the following points will be discussed: After a brief review of qualitative features of threshold production (section 2.5.1), the present status of our theoretical understanding of the total cross section will be presented in section 2.5.2.

The momentum distribution of top quarks and their decay products offers an alternative and complementary route to probe the interquark potential, as shown in section 2.5.3. Spin effects and angular distributions are sensitive towards the small P-wave contribution induced by the axial part of the neutral current. The theoretical framework and the resulting predictions are collected in section 2.5.4. Rescattering, relativistic corrections and other terms of order α_s^2 will be touched upon in section 2.5.5.

2.5.1 Introductory remarks

For a qualitative understanding it is illustrative to compare the different scales which govern top production close to threshold. The quarks are produced at a scale comparable to their Compton wave length

$$d_{\rm prod} \sim 1/m_t \tag{2.77}$$

Electroweak vertex corrections do not alter this behaviour significantly, since Z- or W-boson exchange proceeds at a distance $\approx 1/m_Z$ which is still short compared to scales characteristic for the bound state dynamics. For the QCD potential

$$V_{\rm QCD} = -\frac{4}{3}\frac{\alpha_s}{r} \tag{2.78}$$

one anticipates an effective coupling constant $\frac{4}{3}\alpha_s \approx 0.2$, if α_s is evaluated at the scale of the Bohr momentum

$$k_B \approx \frac{4}{3}\alpha_s\frac{m_t}{2} \approx 20 GeV \tag{2.79}$$

The resulting Bohr radius

$$r_{\rm Bohr} = 1/k_B \tag{2.80}$$

is small compared to hadronic scales. The binding energy of the 1S level

$$E_B = \left(\frac{4}{3}\alpha_s\right)^2\frac{m_t}{4} \approx 2GeV \tag{2.81}$$

and, quite generally, the separation between different resonances, is smaller than the decay rate

$$2\Gamma_t \approx 3GeV \tag{2.82}$$

whence all resonances will merge and join smoothly with the continuum.

The coupling strength κ of the Yukawa potential

$$V_Y = -\frac{\kappa}{r}e^{-m_H r} \quad \text{with} \quad \kappa = \sqrt{2}G_F\frac{m_t^2}{4\pi} = 0.042 \tag{2.83}$$

is comparable to the QCD coupling $4/3\alpha_s = 0.2$ in magnitude. The exponential damping, however, with a cutoff $1/m_H \ll r_{\rm Bohr}$ and a lower limit $m_H > 65$ GeV, reduces the impact of the Yukawa potential quite drastically. (The situation may be different in multi-Higgs-models: the couplings could be enhanced and, even more important, the Higgs might be lighter!) Furthermore, the nonrelativistic treatment is no longer adequate and retardation effects must be taken into consideration.

The large top quark width plays a crucial role for the threshold behaviour. The long distance part of the potential becomes irrelevant with a cutoff corresponding to momenta $x_0^{-1} \sim \sqrt{2m_t\Gamma_t} \sim 24$ GeV,and the $t\bar{t}$ system can be described entirely withing the framework of perturbative QCD. Instead of summing the contributions from a large number of high radial excitations one may directly calculate the imaginary part of the Greens function for complex energy

$$\begin{aligned}\sigma(e^+e^- \to t\bar{t}) &= \frac{24\pi^2\alpha^2}{s}\frac{\rho_v(s)}{m_t^2}\left(1-\frac{16}{3}\frac{\alpha_s}{\pi}\right)\sum_n |\psi_n(0)|^2 \frac{\Gamma_t}{(E_n-E)^2+\Gamma_t^2} \\ &= \frac{24\pi^2\alpha^2}{s}\frac{\rho_v(s)}{m_t^2}\left(1-\frac{16}{3}\frac{\alpha_s}{\pi}\right)\sum_n Im\frac{\psi_n(0)\psi_n^*(0)}{E_n-E-i\Gamma_t} \\ &= -\frac{24\pi^2\alpha^2}{s}\frac{\rho_v(s)}{m_t^2}\left(1-\frac{16}{3}\frac{\alpha_s}{\pi}\right) ImG(0,0,E+i\Gamma) \qquad (2.84)\end{aligned}$$

The factor $\rho_v(s)$ incorporates the contributions from the intermediate photon and Z and is given by

$$\rho_v^{Born}(s) = \left|e_te_e + \frac{1}{y^2}\frac{v_tv_eM_\theta^2}{s-M_Z^2+iM_Z\Gamma_Z}\right|^2 + \left|\frac{1}{y^2}\frac{v_ta_eM_G^2}{s-M_Z^2+iM_Z\Gamma_Z}\right| \qquad (2.85)$$

$$v_f = 2I_{3f} - 4e_f\sin^2\theta_W \qquad a_f = 2I_{3f} \qquad y = 16\sin^2\theta_W\cos^2\theta_W$$

($\alpha = \alpha_{\text{eff}} = 1/128$ has been adopted in the numerical evaluation. Radiative corrections to this formula have been discussed in [170].)

The problem can be solved in closed analytical form for an exact Coulomb potential [183]; to arrive at a realistic prediction of the total (and, in sect 2.5.3 of the differential) cross section a realistic QCD potential must be used.

2.5.2 The QCD potential

On the basis of earlier conceptual work in [184, 185] the asymptotic behaviour of the static potential has been derived in NLO [186, 187] and even NNLO [188]. In momentum space the potential reads in the $\overline{MS}$ subtraction scheme

$$\begin{aligned}V\left(Q^2,\alpha_{\overline{MS}}(Q^2)\right) \;&=\; -\frac{16\pi}{3}\frac{\alpha_{\overline{MS}}(Q^2)}{Q^2}\left[1+\left(\frac{31}{3}-\frac{10}{9}n_f\right)\frac{\alpha_{\overline{MS}}(Q^2)}{4\pi}\right. \\ &\left. +\left(\frac{4343}{18}+66\zeta_3+54\pi^2-\frac{9}{4}\pi^4-\left(\frac{1229}{27}+\frac{52}{3}\zeta_3\right)n_f+\frac{100}{81}n_f^2\right)\left(\frac{\alpha_{\overline{MS}}(Q^2)}{4\pi}\right)^2\right] \qquad (2.86)\end{aligned}$$

The renormalization scale μ^2 has been chosen as Q^2, and n_f refers to the number of massless quarks. For the momentum range above 20 GeV explored by the $t\bar{t}$ system n_f =5 seems adequate. In practice one connects the theoretically predicted short distance part smoothly with the empirically determined potential above ~0.1 fermi (Fig. 2.27, 2.28) The large decay rate acts as a cutoff and the predictions are fairly insensitive to the actual regularisation of the potential for small Q^2. However, an additional constant which can be traded against a shift in m_t must be carefully calibrated.

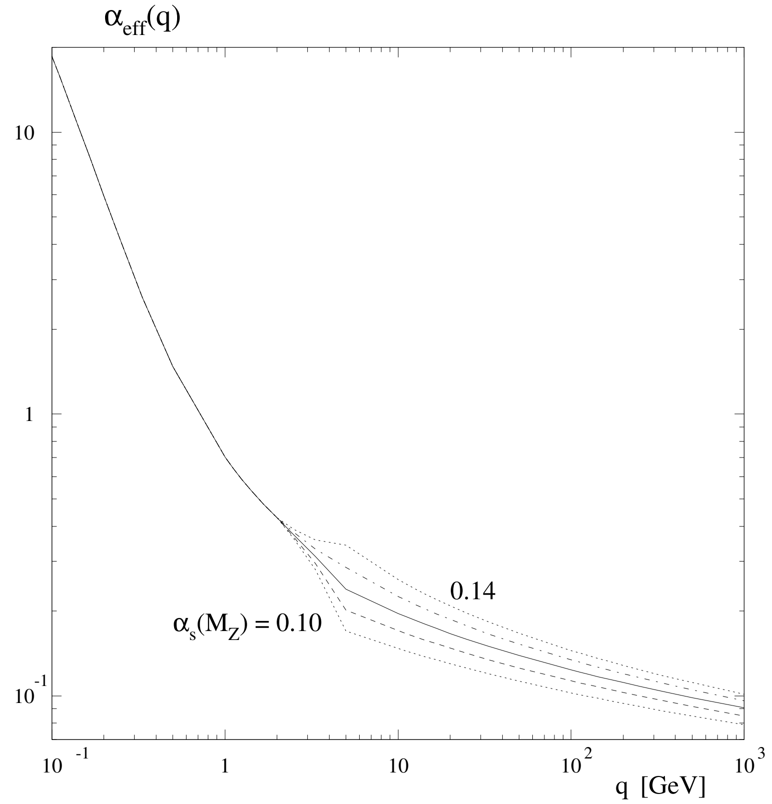

Figure 2.27: α_{eff} *for different values of* $\alpha_s(M_Z)$*: solid: 0.12, dashed: 0.11, dashed-dotted: 0.13, dotted: 0.10 and 0.14; [198].*

2.5.3 Realistic predictions for $\sigma_{t\bar{t}}$.

For a realistic QCD potential the Green's function can only be calculated with numerical methods. An elegant algorithm for a solution in coordinate space has been suggested in [189]. As a consequence of the optical theorem (see also eqn. (2.84)) only the imaginary part of $G(\vec{r} = 0, \vec{r}' = 0, E + i\Gamma_t)$ is needed to predict the total cross

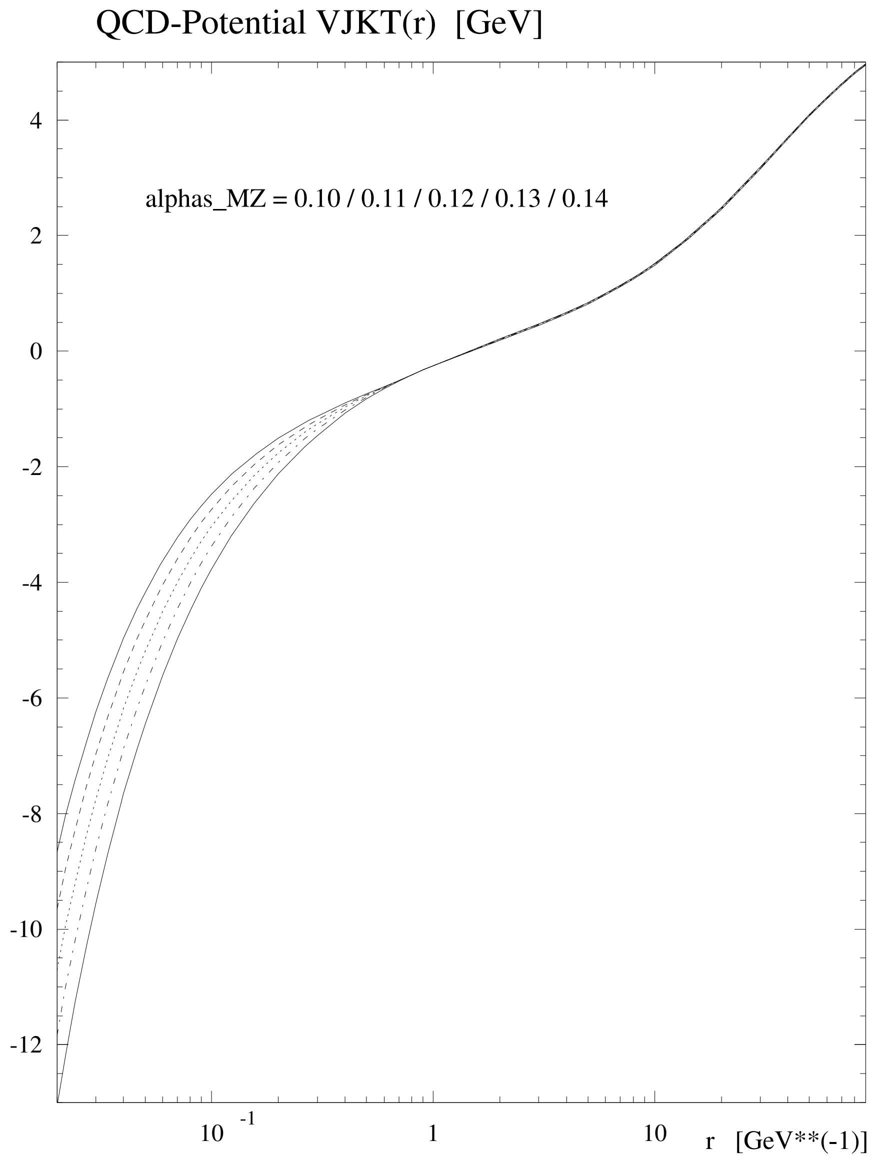

Figure 2.28: *QCD potential in the position space V_{JKT} for different values of $\alpha_s(M_Z)$: solid: 0.12, dashed: 0.11, dashed-dotted: 0.13, dotted: 0.10 and 0.14; [198].*

section. The differential equation for the Green's function

$$\left[(E+i\Gamma_t)-\left(-\frac{\nabla^2}{m_t}+V(\vec{r})\right)\right]G(\vec{r},\vec{r}'=0,E+i\Gamma_t)=\delta(\vec{r}) \tag{2.87}$$

is solved in a way which provides direct access to $\mathrm{Im}G(\vec{r}=0,\vec{r}'=0,E+i\Gamma_t)$ without the need to calculate the full $\vec{r}$ dependence. Alternatively, in [190, 191] the Green's function in momentum space was obtained from the Lippmann-Schwinger equation

$$\begin{aligned}G(\vec{p},E+i\Gamma_t) &= G_0(\vec{p},E+i\Gamma_t)+G_0(\vec{p},E+i\Gamma_t)\\ &\quad\times\int\frac{d\vec{q}}{(2\pi)^3}\tilde{V}(\vec{p}-\vec{q})G(\vec{q},E+i\Gamma_t)\\ G_0(\vec{p},E+i\Gamma_t) &= \frac{1}{E-p^2/m_t+i\Gamma_t}\end{aligned} \tag{2.88}$$

The total cross section is in this case obtained from the integral over the differential distribution

$$\frac{d\sigma}{d^3p}=\frac{3\alpha^2}{\pi s m_t^2}\rho_v(s)\Gamma_t|G(\vec{p},E+i\Gamma_t)|^2 \tag{2.89}$$

This second formulation is particularly suited to introducing a momentum and energy dependent width $\Gamma(p,E)$ which allows to incorporate the phase space suppression and certain α_s^2 rescattering corrections to be discussed below in section 2.5.6.

It is well known that the coupling of the virtual photon to the quarkonium bound-state is modified by "hard" gluon exchange. The vertex correction to the vector current produces an additional factor $\left(1-\frac{16}{3}\frac{\alpha_s}{\pi}\right)$ for the quarkonium decay rate into e^+e^- through the virtual photon or Z. This factor can be calculated by separating the gluon exchange [192] correction to the vertex into the instanteneous potential piece and a remainder which is attributed to gluons with high virtualities of order m_t. A similar approach has been developed in [169] for Higgs exchange. The vertex correction is again decomposed into a part which is given by the instantaneous Yukawa potential

$$V_{Yuk}(r)=-\kappa\frac{e^{-m_H r}}{r} \tag{2.90}$$

with $\kappa=\sqrt{2}Gm_t^2/4\pi$ and a remainder which is dominated by highly virtual Higgs exchange. The rapid increase of the correction in the threshold region (cf. sect. 3.1.2) is driven by the potential; the remainder, the hard vertex correction, is fairly energy independent. The total cross section is thus sensitive to the top mass, the width (which in the SM is uniquely determined by m_t), the strong coupling constant α_s and the mass of the Higgs boson. The dependence on the top quark mass is illustrated in Fig. 2.29. Apart from the trivial shift of the threshold due to a change in m_t

the shape of σ is affected by the rapidly increasing width of the top quark which amounts to 0.81 GeV, 1.57 GeV and 2.24 GeV for $m_t = 150$ GeV, 180 GeV, and 200 GeV respectively. A fairly pronounced 1S peak is still visible for $m_t = 150$ GeV, for $m_t = 200$ GeV, however, only a smooth shoulder is predicted. The behaviour is qualitatively very similar, if we keep m_t fixed say at 180 GeV and decrease or increase Γ_t be the corresponding amount. The shape of the cross section will therefore allow to determine the width of the top quark. A qualitatively very different response is observed towards a change in α_s (Fig. 2.29). The binding energy increases with α_s, the aparent threshold is thus lowered (This is the reason for the strong correlation between α_s and m_t in the experimental analysis based on σ_{tot} only [193, 194].) and the height of the "would-be resonance" is increased. Even several GeV above threshold one observes a slight increase of the cross section with α_s, a consequence of the enhanced attraction between t and $\bar{t}$. A variation in m_H for m_H above ~ 65 GeV affects mainly the normalization of the cross section. Measurements with a precision better than 10% will become sensitive to the effect of a relatively light Higgs boson.

Up to this point the amplitude induced by virtual Z and γ are included in Born approximation only. Electroweak corrections and initial state radiation are neglected. A detailed discussion of electroweak corrections to the cross section and the left right asymmetry in the context of the SM can be found in [170]. The corresponding discussion for the two-Higgs-doublet model is presented in [195]. In this model one might encounter enhanced Yukawa couplings which would amplify the effect under discussion.

Initial state radiation leads to a fairly drastic distortion of the shape of the cross section, in particular to a smearing of any pronounced structure.

Beamstrahlung and the energy spread of the beam lead to a further smearing of the apparent cross section. These accelerator dependent issues are treated in more detail in [194, 196].

2.5.4 Momentum distributions of top quarks

The Green's function in momentum space and the momentum distribution of top quarks (and thus their decay products) are intimately related [197, 190]

$$\frac{d\sigma_n}{d\vec{p}}(\vec{p}, E) = \frac{3\alpha^2 Q_t^2}{\pi s m_t^2}\Gamma_t \left|G(\vec{p}, E + i\Gamma_t)\right|^2 \tag{2.91}$$

with

$$G(\vec{p}, E + i\Gamma_t) = \int d\vec{r} e^{i\vec{p}\vec{r}} G(\vec{r}, \vec{r}' = 0, E + i\Gamma_t) \tag{2.92}$$

As discussed in sect. 2.5.2, the Green's function can be obtained in momentum space as a solution of the Lippmann-Schwinger equation. For an energy close to the 1S peak it exhibits a fairly smooth behaviour reminiscent of the 1S wave function in

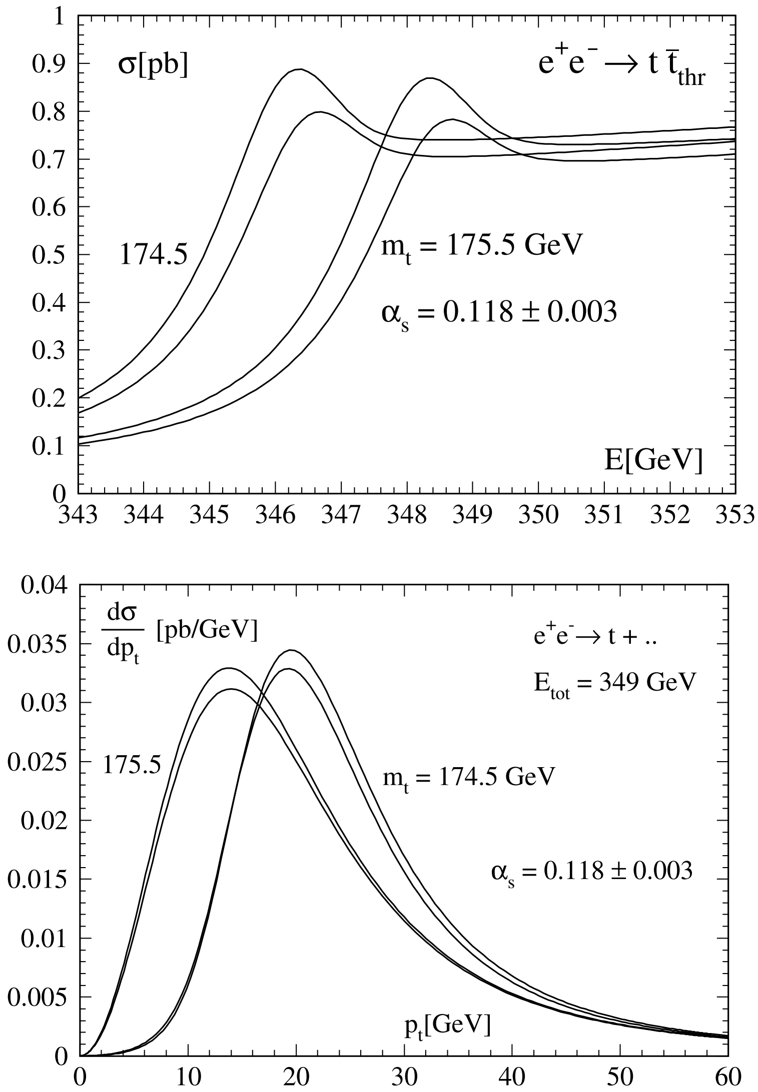

Figure 2.29: *Upper part: The cross section for the production of top quarks near the threshold. Demonstrated is the sensitivity of the cross section to the value of the top mass and the QCD coupling (normalized at the Z mass). Lower part: The momentum spectrum of the top quarks near the threshold for a fixed total c.m. energy. The momentum depends strongly on the top mass, yet less on the QCD coupling. Refs.[190].*

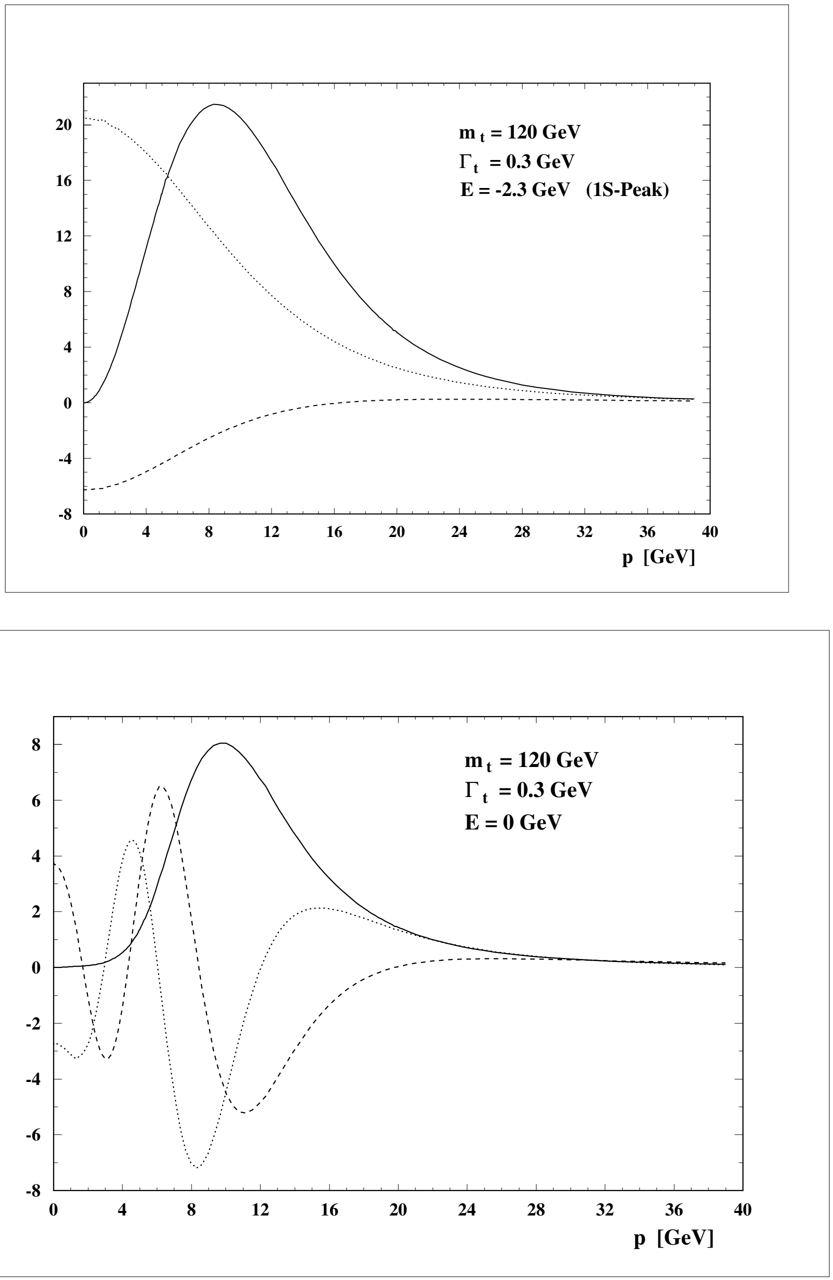

Figure 2.30: *Real (dashed) and imaginary (dotted) parts of the Green's function for an energy corresponding to the 1S peak (upper figure) and for $E = 0$ (lower figure). Solid curve: $|pG(p)|^2 \cdot 0.002$; [190].*

momentum space (Fig. 2.30). With increasing energy an oscillatory pattern of the amplitude is observed, and a shift towards larger momenta (Fig. 2.30). These results are intentionally displayed for $m_t = 120$ GeV, where the oscillations are still clearly visible, in contrast to m_t=180 GeV where all oscillations are smeared by the large width Γ_t. The corresponding predictions for the distributions at $m_t = 180$ GeV are displayed in Fig. 2.31. The transition from a wide distribution below the nominal

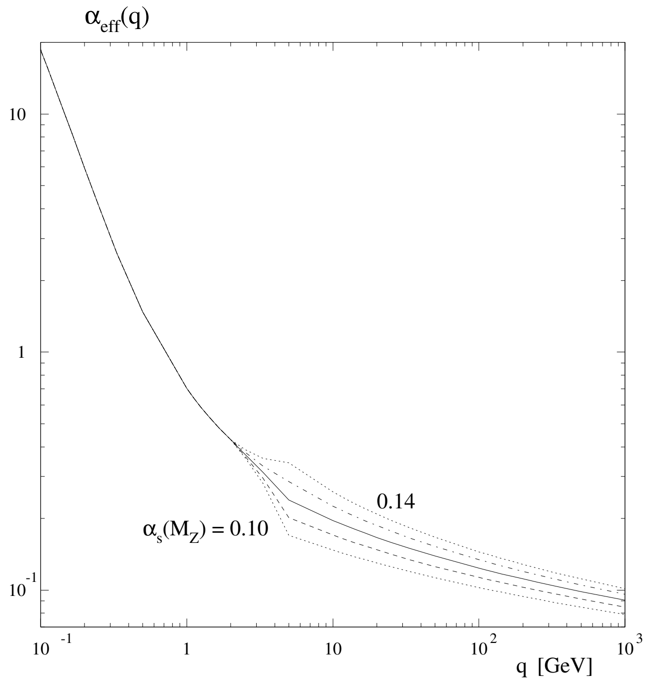

Figure 2.31: *Momentum distribution of top quarks for three different cms energies.*

threshold to a narrow one with the location of the peak determined by trivial kinematics is clearly visible. The impact on the energy distribution of the W's from top decay is shown in Fig. 2.32. The dependence on α_s and m_t can be seen in Fig. 2.29 [198].

2.5.5 Angular distributions and polarization

Close to threshold the production amplitude is dominantly S-wave which leads to an isotropic angular distribution. The spin of top quarks is alligned with the beam direction, with a degree of polarization determined by the electroweak couplings, the beam polarization and the mass of the top quark, but independent of the production dynamics, in particular of the potential.

Small, but nevertheless experimentally accessible corrections do arise from the small admixture of P-wave contributions and from rescattering of the top quark decay products. Let us concentrate for the moment on the first mechanism. P-wave

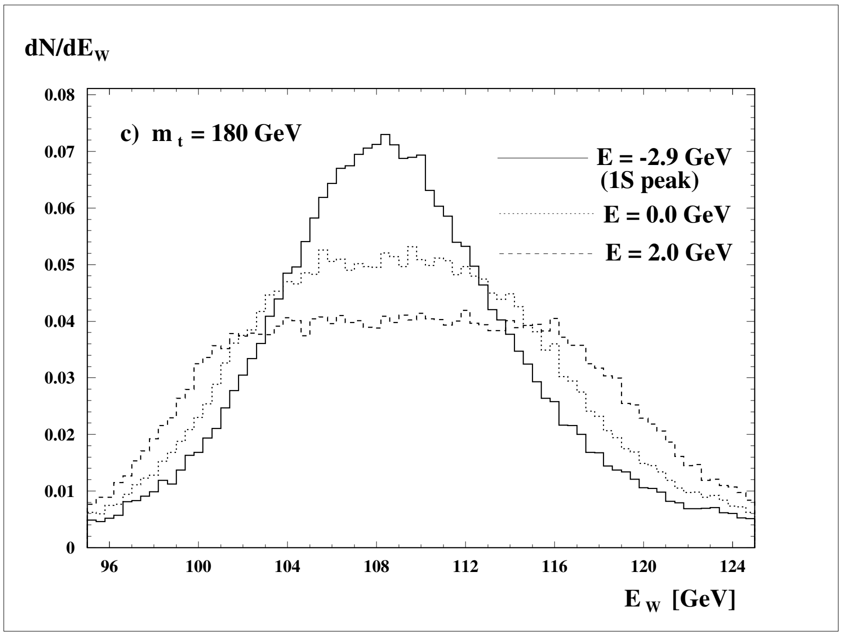

Figure 2.32: *Energy distribution of W's from top quark decay for three different cms energies.*

amplitudes are proportional to the top quark momentum. For stable noninteracting particles the momentum vanishes at threshold. However, as discussed in the previous section the expectation value of the quark momentum is nonzero for all energies — a consequence of the large top decay rate and the uncertainty principle. Technically the P-wave contribution is calculated with the help of the Green's function technique. The generalization of the Lippman-Schwinger equation (2.88) from S- to P-waves reads as follows [199] (for a related discussion in coordinate space see [200])

$$\mathcal{F}(\mathrm{p}, E) \quad = \quad G_0(p, E) + G_0(p, E) \int \frac{d^3k}{(2\pi)^3} \frac{\mathbf{p}\cdot\mathbf{k}}{\mathbf{p}^2} V(\mathbf{p}-\mathbf{k}) \mathcal{F}(k, E) \qquad (2.93)$$

It is then straightforward to calculate the differential momentum distribution and the polarization of top quarks produced in electron positron annihilation.

The following abbreviations will be useful below:

$$\begin{aligned} v_f &= 2I_f^3 - 4q_f \sin^2\theta_{\mathrm{W}}, \qquad a_f = 2I_f^3. \\ a_1 &= q_e^2 q_t^2 + (v_e^2 + a_e^2) v_t^2 d^2 + 2q_e q_t v_e v_t d \\ a_2 &= 2v_e a_e v_t^2 d^2 + 2q_e q_t a_e v_t d \\ a_3 &= 4v_e a_e v_t a_t d^2 + 2q_e q_t a_e a_t d \\ a_4 &= 2(v_e^2 + a_e^2) v_t a_t d^2 + 2q_e q_t v_e a_t d \end{aligned} \qquad (2.94)$$

$$d = \frac{1}{16\sin^2\theta_{\rm W}\cos^2\theta_{\rm W}}\,\frac{s}{s-M_Z^2}.$$

P_- (P_+) denotes the longitudinal electron (positron) polarization and $\chi = (P_+ - P_-)/(1-P_+P_-)$ can be interpreted as effective longitudinal polarization of the virtual intermediate photon or Z boson.

The differential cross section, summed over polarizations of quarks and including S-wave and S-P–interference contributions, is thus given by [200, 199]

$$\begin{aligned} \frac{d^3\sigma}{dp^3} &= \frac{3\alpha^2\Gamma_t}{4\pi m_t^4}(1-P_+P_-)\left[(a_1+\chi a_2)\left(1-\frac{16\alpha_s}{3\pi}\right)|G(\mathrm{p},E)|^2 + \right. \\ &\quad \left. +(a_3+\chi a_4)\left(1-\frac{12\alpha_s}{3\pi}\right)\frac{\mathrm{p}}{m_t}\Re\left(\,G(\mathrm{p},E)F^*(\mathrm{p},E)\,\right)\,\cos\vartheta\right]. \end{aligned} \tag{2.95}$$

The vertex corrections from hard gluon exchange for S-wave and P-wave amplitudes are included in this formula. It leads to the following forward-backward asymmetry

$$\mathcal{A}_{\rm FB}(\mathrm{p},E) = C_{\rm FB}(\chi)\,\varphi_{\rm R}(\mathrm{p},E), \tag{2.96}$$

with

$$C_{\rm FB}(\chi) = \frac{1}{2}\,\frac{a_3+\chi a_4}{a_1+\chi a_2}, \tag{2.97}$$

$\varphi_{\rm R} = \Re\,\varphi$, and

$$\varphi(\mathrm{p},E) = \frac{(1-4\alpha_s/3\pi)}{(1-8\alpha_s/3\pi)}\,\frac{\mathrm{p}}{m_t}\,\frac{F^*(\mathrm{p},E)}{G^*(\mathrm{p},E)}. \tag{2.98}$$

This result is still differential in the top quark momentum. Replacing $\varphi(\mathrm{p},E)$ by

$$\Phi(E) = \frac{(1-4\alpha_s/3\pi)}{(1-8\alpha_s/3\pi)}\,\frac{\int_0^{\mathrm{p}_m} d\mathrm{p}\,\frac{\mathrm{p}^3}{m_t}\,F^*(\mathrm{p},E)G(\mathrm{p},E)}{\int_0^{\mathrm{p}_m} d\mathrm{p}\,\mathrm{p}^2\,|G(\mathrm{p},E)|^2}. \tag{2.99}$$

one obtains the integrated forward-backward asymmetry again. A cutoff p_m must be introduced to eliminate the logarithmic divergence of the integral.

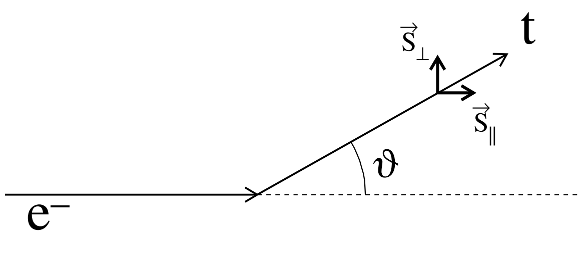

Figure 2.33: *Definition of the spin directions. The normal component* $\mathrm{s}_{\rm N}$ *points out of the plane.*

Polarization [199, 201]:
To describe top quark polarization in the threshold region it is convenient to align the reference system with the beam direction (Fig. 2.33) and to define

$$\mathbf{s}_{\|} = \mathbf{n}_{e^-}, \quad \mathbf{s}_{\mathrm{N}} = \frac{\mathbf{n}_{e^-} \times \mathbf{n}_t}{|\mathbf{n}_{e^-} \times \mathbf{n}_t|}, \quad \mathbf{s}_{\perp} = \mathbf{s}_{\mathrm{N}} \times \mathbf{s}_{\|}. \tag{2.100}$$

In the limit of small β the quark spin is essentially aligned with the beam direction apart from small corrections proportional to β, which depend on the production angle.

Including the QCD potential one obtains for the three components of the polarization [199]

$$\begin{aligned}
\mathcal{P}_{\|}(\mathbf{p}, E, \chi) &= C_{\|}^0(\chi) + C_{\|}^1(\chi)\,\varphi_{\mathrm{R}}(\mathrm{p}, E)\,\cos\vartheta && (2.101)\\
\mathcal{P}_{\perp}(\mathbf{p}, E, \chi) &= C_{\perp}(\chi)\,\varphi_{\mathrm{R}}(\mathrm{p}, E)\,\sin\vartheta && (2.102)\\
\mathcal{P}_{\mathrm{N}}(\mathbf{p}, E, \chi) &= C_{\mathrm{N}}(\chi)\varphi_{\mathrm{I}}(\mathrm{p}, E)\sin\vartheta\,, && (2.103)
\end{aligned}$$

$$\begin{aligned}
C_{\|}^0(\chi) &= -\frac{a_2 + \chi a_1}{a_1 + \chi a_2}, & C_{\|}^1(\chi) &= \left(1 - \chi^2\right)\frac{a_2 a_3 - a_1 a_4}{\left(a_1 + \chi a_2\right)^2}, \\
C_{\perp}(\chi) &= -\frac{1}{2}\frac{a_4 + \chi a_3}{a_1 + \chi a_2}, & C_{\mathrm{N}}(\chi) &= -\frac{1}{2}\frac{a_3 + \chi a_4}{a_1 + \chi a_2} = -C_{\mathrm{FB}}(\chi),
\end{aligned} \tag{2.104}$$

with $\varphi_{\mathrm{I}} = \Im\varphi$, and $\varphi(\mathrm{p}, E)$ as defined in (2.98). The momentum integrated quantities are obtained by the replacement $\varphi(\mathrm{p}, E) \to \Phi(E)$. The case of non-interacting stable quarks is recovered by the replacement $\Phi \to \beta$, an obvious consequence of (2.99).
Let us emphasize the main qualitative features of the result:

- Top quarks in the threshold region are highly polarized. Even for unpolarized beams the longitudinal polarization amounts to about -0.41 and reaches ± 1 for fully polarized electron beams. This later feature is of purely kinematical origin and independent of the structure of top quark couplings. Precision studies of polarized top decays are therefore feasible.

- Corrections to this idealized picture arise from the small admixture of P-waves. The transverse and the normal components of the polarization are of order 10%. The angular dependent part of the parallel polarization is even more suppressed. Moreover, as a consequence of the angular dependence its contribution vanishes upon angular integration.

- The QCD dynamics is solely contained in the functions φ or Φ which is the same for the angular distribution and the various components of the polarization. (However, this "universality" is affected by the rescattering corrections.) These functions which evidently depend on QCD dynamics can thus be studied in a variety of ways.

- The relative importance of P-waves increases with energy, $\Phi \sim \sqrt{E/m_t}$. This is expected from the close analogy between $\Phi_{\rm R} = \Re\,\Phi$ and β. In fact, the order of magnitude of the various components of the polarization above, but close to threshold, can be estimated by replacing $\Phi_{\rm R} \to {\rm p}/m_t$ (Fig. 2.34).

- The imaginary part of Φ approaches a constant value $\approx \frac{2}{3}\alpha_s$ (Fig. 2.34). The component of the polarization normal to the production plane is thus approximately independent of E and essentially measures the strong coupling constant. In fact one can argue that this is a unique way to get a handle on the scattering of heavy quarks through the QCD potential.

As discussed before, $C_{\|}^0$ assumes its maximal value ± 1 for $\chi = \mp 1$ and the coefficient $C_{\|}^1$ is small throughout. The coefficient $C_\perp$ varies between $+0.7$ and -0.5 whereas $C_{\rm N}$ is typically around -0.5. The dynamical factors Φ are around 0.1 or larger, such that the P-wave induced effects should be observable experimentally.

2.5.6 Rescattering

For a particle with a very small decay rate production and decay amplitudes can be clearly separated. This is fairly evident from the space-time picture of such a sequence. Prior to its decay the particle travels away from the production point and any coherence is lost between the two reactions. The situation is different for the case under discussion, an unstable top quark which decays within the range of interaction between t and $\bar{t}$. In such a situation the decay products from t are still affected by the force originating from $\bar{t}$ and vice versa (Fig. 2.35).

In ref. [202, 203] it has been demonstrated that the total cross section remains unaffected by rescattering in order α_s. This result had been anticipated in [190] on the basis of earlier work which considered the decay rate of a muon bound in the strong field of a nucleus [204]. In contrast momentum and angular distributions [200, 203, 205] as well as the top quark polarization [201] are affected by rescattering between t and $\bar{b}$ and between $\bar{t}$ and b (rescattering between b and $\bar{b}$ can be ignored [201]). For example the momentum distribution has to be corrected by a factor $(1 + \psi_1(p, E))$ with

$$\psi_1({\rm p}, E) = 2\,\Im \int \frac{d^3k}{(2\pi)^3} V(|\mathbf{k} - \mathbf{p}|) \frac{G({\rm k}, E)}{G({\rm p}, E)} \frac{\arctan\frac{|\mathbf{k}-\mathbf{p}|}{\Gamma_t}}{|\mathbf{k} - \mathbf{p}|} \tag{2.105}$$

$$\tag{2.106}$$

The distribution is shifted towards smaller momenta by about 5% (Fig. 2.36), an effect that could become relevant in precision experiments. The influence on the forward-backward asymmetry and the polarization is even more pronounced [201], as far as the S-P-wave interference terms are concerned which are thus intrinsically of order β. A detailed discussion of these effects can be found in [201].

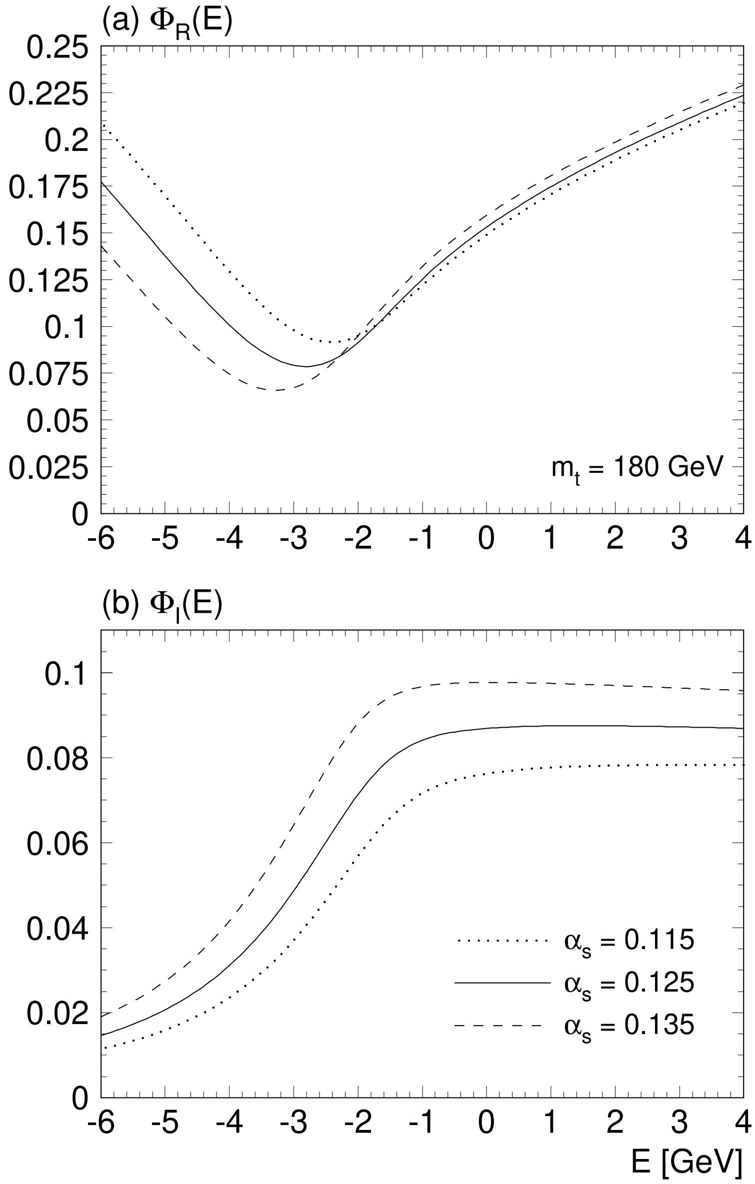

Figure 2.34: *Real and imaginary part of $\Phi(E)$ for three different values of α_s (from [201]).*

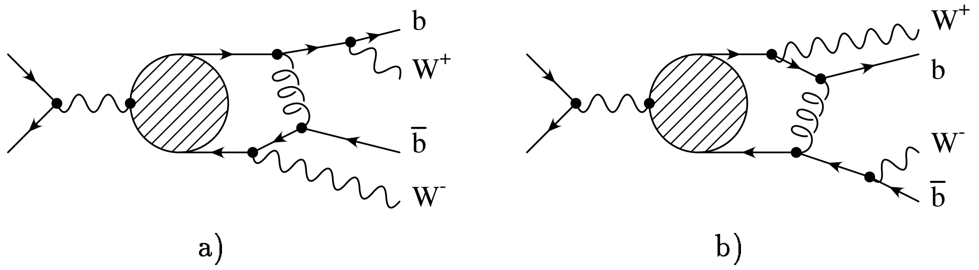

Figure 2.35: *Lowest order rescattering diagrams.*

2.5.7 Relativistic corrections

In $\mathcal{O}(\alpha_s^2)$ one anticipates effects from relativistic corrections, from the reduction of the phase space through the binding energy and from the Coulomb wave function of the b quark. Individually these effects are large. A full calculation of all relativistic $\mathcal{O}(\alpha_s^2)$ effects is not available at present and one has to resort to models and analogies [190, 197, 191]. For example, it has been shown [204, 206] that the decay rate of a muon bound in the field of a nucleus is given by

$$\Gamma = \Gamma_{\text{free}} \left[1 - 5(Z\alpha)^2\right] \left[1 + 5(Z\alpha)^2\right] \left[1 - \frac{(Z\alpha)^2}{2}\right], \tag{2.107}$$

where the first correction factor originates from the phase space suppression, the second from the Coulomb enhancement, and the third from time dilatation. Thus there is no first order correction to the total rate from rescattering in the nucleus potential, similar to the $t\bar{t}$ case discussed above. The second order contributions evidently compensate to a large extent. In a model calculation where these features are implemented [191] through a momentum dependent width, it is found that the total cross section as well as the momentum distribution are hardly affected. These considerations have recently been confirmed in a more formal approach [207].

2.5.8 Perspectives for e^+e^-experiments

The investigation of top quarks constitutes one of the physics goals for a future linear e^+e^-collider [5, 6, 13, 194]. With an R value between ~ 0.7 in the region very close to threshold and about 2 in the continuum (Fig.2.18) one expects 5 000 to 10 000 $t\bar{t}$ events for an integrated luminosity of $10^{40} cm^{-2}$. This large counting rate must be extracted from the background which consists mainly of W-pair and Z-pair production. (Table 2.3).

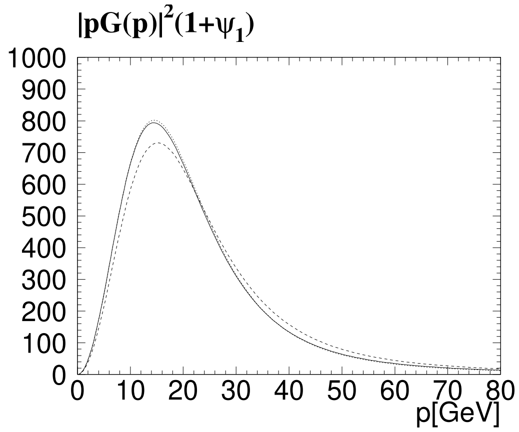

a) E = -3 GeV

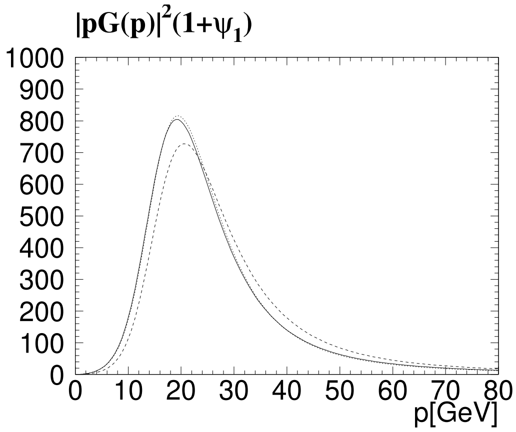

b) E = 0 GeV

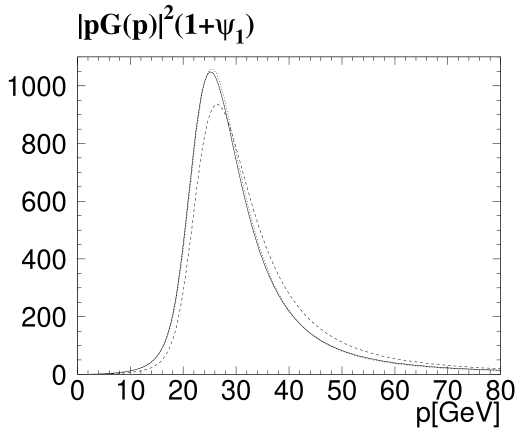

c) E = 2 GeV

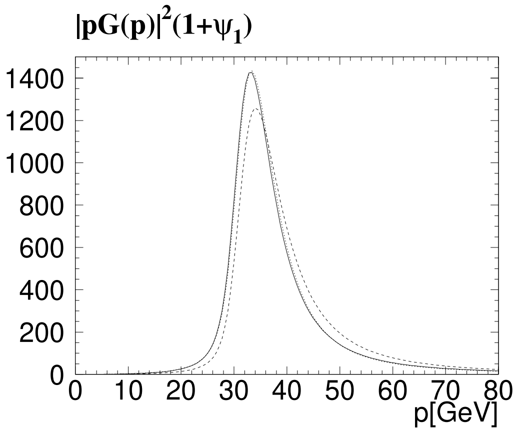

d) E = 5 GeV

Figure 2.36: *Modification of the momentum distribution through rescattering. Dashed line: no rescattering corrections included; Solid line: rescattering contribution with full potential included; dotted line: rescattering contribution with pure Coulomb potential and* $\alpha_s = 0.187$ *included (from [201]).*

Table 2.3: *Cross sections in picobarn for the $t\bar{t}$ signal and for the main background processes. The $t\bar{t}$ cross section is taken as 0.7 times the "point cross section" R. All cross sections are obtained with the inclusion of initial state radiation (from[6]).*

Top mass (GeV)	180
$E_{c.m.}$ (GeV)	370
$t\bar{t}$	0.444
$f\bar{f}$	25.6
W^+W^-	10.3
Z^0Z^0	0.792

t quark selection

Selection of $t\bar{t}$ final states on the basis of topology, charged particle multiplicity and missing energy (Fig.2.37) leads to a drastic reduction of the background with still acceptable loss in efficiency.

Signal to background ratios from 3 to 7 can be reached with these simple methods with tagging efficiencies between 20% and 30%. The selection of events with leptons aims at the prominent subsample with semileptonic $t \to bW(\to \ell\nu)$ decays. As discussed before these events are particularly useful for the analysis of the tbW coupling. The additional suppression from the semileptonic branching ratio may pay off in terms of a pure event sample. Selecting b jets through their content of energetic leptons or through the displaced decay vertex of B mesons one may achieve up to 50% efficiency with a S/B ratio of up to 5. In the subsequent considerations, taken from [6], a conservative $t\bar{t}$ tagging efficiency of 25% and a S/B ratio of 5 were assumed.

Threshold scan

As stated already in the introduction two important goals of top quark physics can be anticipated in the context of the SM: The determination of the top quark mass through the measurement of t quark decay products and the threshold scan which will provide information on m_t, and at the same time on the interaction between t and $\bar{t}$ through the QCD potential and eventually through Higgs exchange.

The extraction of the rapidly varying cross section depends critically on the beam energy spread and on the smearing through beamstrahlung. A large variety of machine designs can be found in the literature which differ drastically in luminosity and energy smearing. Even in the most favorable (TESLA) design the toponium peak is almost completely smeared out. There remains, however, a marked step at threshold. This indicates that the determination of m_t will be possible to fairly high accuracy from the shape of the cross section; the normalisation might carry information on the strenght of the QCD potential. The extraction of more subtle parameters like the

Figure 2.37: *Characteristic distributions for $t\bar{t}$ signal events (shaded histograms) and background events (white histograms). the normalisation of the distributions is arbitary. (a) Thrust, (b) charged particle multiplicity and (c) missing energy distributions.*

Yukawa coupling or the top quark decay width will presumably be difficult, assuming of course that they are not too different from their standard model values.

Figure 2.38: *Sensitivity of the exitation curve, convoluted by the luminosity spectrum of the TESLA collider design, to the top quark mass, at* $m_t = 180 GeV$. *The full lines correspond to the nominal value of* m_t, *the dashed (doted) lines to values which differ from their nominal value by* $\pm 200 MeV$, *(*$\pm 400 MeV$*). The " eperimental" points correspond to a measuring time of* 10^6 *seconds each.*

This expectation is borne out by a more detailed simulation (Fig.2.38), which suggests that a one sigma deviation of one to several hundred MeV can be achieved.

Allowing for a realistic uncertainty in α_s and hence in the QDC potential an error of 400 MeV to 600 MeV is expected. Using the total cross section, the momentum distribution and the forward backward asymmetry simultaneously [194, 196], this can be further reduced to even less than 100 MeV (Fig. 2.39);

more than an order of magnitude superior to the expectations from jet analysis at an hadron collider.

t quark reconstruction

The study of the excitation curve is complemented by the reconstruction of top quark decay products, leading to an independent mass determination. This may arise from the analysis of the W momentum in semileptonic $t\bar{t}$ events, a method particularly suited for the threshold region. At energies significantly higher than $2m_t$ the invariant mass per hemisphere is a sensitive measure of m_t. Identifying jets and combining them to reconstruct the top quark in a constrained fit seems at present to be the most promising technique, leading to a determination of the order of 1 GeV.

Combining the results of the different techniques the systematic experimental errors should be well under control [6]. To evaluate the influence of fragmentation

Figure 2.39: *Results of the* χ^2 *fit using the total cross section and the momentum distribution (from [196]).*

Figure 2.40: *"Explored" regions (below the curves) for different values of* $\int \mathcal{L}$ *in the* $M_{H^\pm}$ *vs.* $\tan\beta$ *plane (99.73% C.L.) (from [139]).*

and to relate this kinematic top mass to the one determined in the threshold scan seem to be the limiting factors at present.

Anomalous top quark decays

The search for anomalous top quark decays is facilitated by the favourable signal to background ratio predicted for electron positron annihilation [6, 139]. These decays could be an important element in the study of physics beyond the standard model.

The decay mode $t \to H^+b$ is predicted with a sizeable branching ratio in a two Higgs doublett model. It would manifest itself by an excess of τ leptons (discussed before) as a consequence of the large branching ratio for $H \to \tau\nu$. Searching for τ "jets" with a single charged prong and posssible additional neutral particles leads to a total τ efficiency of 30%. This allows the detection of the anomalous decay $t \to H^+b$ with a statistical significance of at least 3 standard deviations for a large part of the parameter space, in particular large $\tan\beta$ in a data sample of 10 fb^{-1}, as exemplified in Fig.2.40.

With the masses of supersymmetric particles being only loosely constrained the decay mode $t \to \tilde{t}\tilde{\gamma}$ followed by the decay chain $\tilde{t} \to b\tilde{W} \to bW\tilde{\gamma}$ would provide a remarkable laboratory for supersymmetry. An exploratory study [6, 139] indicates that this channel, if kinematically accessible, may be detected and studied with a a reasonable investment of luminosity.

Bibliography

[1] S.L. Glashow, *Nucl. Phys.* **B 22** (1961) 579;
S. Weinberg, *Phys. Rev. Lett.* **19** (1967) 1264;
A. Salam, in "*Elementary Particle Theory*", Stockholm 1968.

[2] M. Kobayashi and T. Maskawa, *Prog. Theor. Phys.* **49** (1973) 652.

[3] F. Abe et cal. [CDF Coll.], *Phys. Rev. Lett.* **74** (1995) 2626;
S. Abachi et al. [D0 Coll.], *Phys. Rev. Lett.* **74** (1995) 2632.

[4] J. Lefrançois, Proceedings Intern. Europhysics Conference on High Energy Physics, Marseille 1993.

[5] E. Accomando et al., DESY–ECFA study: "Physics with e^+e^- Linear Colliders", DESY 97–100, *Phys. Rep.* **C** in press.

[6] P. Igo-Kemenes, J.H. Kühn [conv.], in DESY 93-123 A,B.

[7] C. Jarlskog (ed.), "*CP Violation*", World Scientific; see in particular the contribution by I.I.Y. Bigi, V.A. Khoze, N.G. Uraltsev and A.I. Sanda in this compendium.

[8] S. Bethke, A. Ricker and P.M. Zerwas, *Z. Phys.* **C 49** (1991) 59.

[9] H. Fritzsch, Workshop on Strong Coupling Gauge Theories and Beyond, Nagoya, 1990, Report MPI–PAE/PTh 64/90, and references quoted therein.

[10] W. Buchmüller in Ref.[11].

[11] J.H. Kühn, P.M. Zerwas [conv.] et al., "*Z physics at LEP 1*", CERN 89–08.

[12] E. Reya, P.M. Zerwas [conv.] et al., in Proceedings ECFA LHC Workshop, Aachen 1990, CERN 90–10.

[13] P.M. Zerwas, Top Physics at e^+e^-Linear Colliders, Proceedings Saariselkä Workshop; DESY 91-108;
J.H. Kühn, Proceedings 2nd Intern. Workshop on Physics and Experiments with Linear Colliders, Waikoloa 1993.

[14] J.H. Kühn, in Proceedings SLAC Summer Institute on Particle Physics, Stanford 1995, SLAC-R-494 CONF-9507258-UC-414.

[15] J.F Donoghue, D. Treille [conv.] et al., Proceedings of the Workshop "*High–Luminosity Extension of LEP* ", CERN 1990.

[16] K.G. Chetyrkin, A. Kwiatkowski, and J.H. Kühn, *Phys. Reports* **277** (1996) 189.

[17] K.G. Chetyrkin, A.L. Kataev and F.V. Tkachov, *Phys. Lett.* **B 85** (1979) 277;
M. Dine and J. Sapirstein, *Phys. Rev. Lett.* **43** (1979) 668;
W. Celmaster and R.J. Consalves, *Phys. Rev. Lett.* **44** (1980) 560.

[18] S.G. Gorishny, A.L. Kataev and S.A. Larin, *Phys. Lett.* **B 259** (1991) 144.
L.R. Surguladze and M.A. Samuel, *Phys. Rev. Lett.* **66** (1991) 560.
K.G. Chetyrkin, *Phys. Lett.* **B 391** (1997) 402.

[19] B.A. Kniehl and J.H. Kühn, *Phys. Lett.* **B 224** (1989) 229;
B.A. Kniehl and J.H. Kühn, *Nucl. Phys.* **B 329** (1990) 547.

[20] K.G. Chetyrkin and J.H. Kühn, *Phys. Lett.* **B 308** (1993) 127.

[21] K.G. Chetyrkin and O.V. Tarasov, *Phys. Lett.* **B 327** (1994) 114;
S.A. Larin, T. van Ritbergen and J.A.M. Vermaseren, *Phys. Lett.* **B 320** (1994) 159.

[22] J. Schwinger, "Particles, Sources and Fields" Vol.II; Addison–Wesley 1973;
G. Källén and A. Sabry, K. Dan. Vidensk. Selsk. Mat.-Fys. Medd. **29** (1955) No. 17.

[23] J. Jersak, E. Laermann and P.M. Zerwas, *Phys. Lett.* **B 98** (1981) 363, and *Phys. Rev.* **D 25** (1982) 1218.

[24] K.G. Chetyrkin and J.H. Kühn, *Phys. Lett.* **B 248** (1990) 359;
K.G. Chetyrkin, A. Kwiatkowski and J.H. Kühn, *Phys. Lett.* **B 282** (1992) 221;
K.G. Chetyrkin and A. Kwiatkowski, *Phys. Lett.* **B 319** (1993) 307.

[25] A.H. Hoang, J.H. Kühn, and T. Teubner, *Nucl. Phys.* **B 452** (1995) 173.

[26] K.G. Chetyrkin, J.H. Kühn, and M. Steinhauser, *Phys. Lett.* **B 371** (1996) 93, *Nucl. Phys.* **B 482** (1996) 213, and hep-ph/9705254.

[27] T. van Ritbergen, J.A.M. Vermaseren, and S.A. Larin, hep-ph/9701390.

[28] K.G. Chetyrkin, hep-ph/9703278;
T. van Ritbergen, J.A.M. Vermaseren, and S.A. Larin, hep-ph/9703284.

[29] N. Gray, D.J. Broadhurst, W. Grafe and K. Schilcher, *Z. Phys.* **C 48** (1990) 673.

[30] A.H. Hoang, M. Ježabek, J.H. Kühn, and T. Teubner, *Phys. Lett.* **B 325** (1994) 495;
M.H. Seymour, *Nucl. Phys.* **B 436** (1995) 163.

[31] Opal Coll., R. Akers et al., *Phys. Lett.* **B 353** (1995) 595.

[32] Delphi Coll., P. Abreu et al., CERN/PPE-97-039.

[33] A. Akhundov, D. Bardin and T. Riemann, *Nucl. Phys.* **B 276** (1988) 1;
J. Bernabeu, T. Pich and A. Santamaria, *Phys. Lett.* **B 200** (1988) 200;
W. Beenakker and W. Hollik, *Z. Phys.* **C 40** (1988) 141;
B. Lynn and R. Stuart, *Phys. Lett.* **B 252** (1990) 676.

[34] A. Djouadi, J.H. Kühn and P.M. Zerwas, *Z. Phys.* **C 46** (1990) 411;
A. Djouadi, B. Lampe and P.M. Zerwas, *Z. Phys.* **C 67** (1995) 123.

[35] A.B. Arbuzov, D. Yu. Bardin and A. Leike, *Mod. Phys Lett.* **7** (1992) 2029 and Erratum **9** (1994) 1515.

[36] M. Veltman, *Nucl. Phys.* **B 123** (1977) 89.

[37] S. Eidelmann and F. Jegerlehner, *Z. Phys.* **C 67** (1995) 585.

[38] A. Djouadi and C. Verzegnassi, *Phys. Lett.* **B 195** (1987) 265.

[39] B.A. Kniehl, J.H. Kühn, and R.G. Stuart, *Phys. Lett.* **B 214** (1988) 621.

[40] L. Avdeev, J. Fleischer, S. Mikhailov, and O.V. Tarasov, *Phys. Lett.* **B 336** (1994) 560, Erratum *Phys. Lett.* **B 349** (1995) 597.

[41] K.G. Chetyrkin, J.H. Kühn, and M. Steinhauser, *Phys. Lett.* **B 351** (1995) 331, *Phys. Rev. Lett.* **75** (1995) 3397.

[42] J. Fleischer, O.V. Tarasov, F. Jegerlehner, and P. Raczka, *Phys. Lett.* **B 293** (1992) 437;
A. Kwiatkowski and M. Steinhauser, *Phys. Lett.* **B 344** (1995) 359.

[43] A. Czarnecki and J.H. Kühn, *Phys. Rev. Lett.* **77** (1996) 3955;
A. Czarnecki and K. Melnikov, hep-ph/9609302, TTP96-33, to appear in *Phys. Rev.* **D**.

[44] LEP Electroweak Working Group, R. Clare et al., "A Combination of Preliminary Electroweak Measurements and Constraints on the Standard Model", CERN Report LEPEWWG/97–01.

[45] G. Girardi, W. Hollik and C. Verzegnassi, *Phys. Lett.* **B 240** (1990) 492.

[46] A. Denner, J. Guth, W. Hollik and J. Kühn, *Z. Phys.* **C 51** (1991) 695.

[47] A.A. Akhundov, D.Yu. Bardin and A. Leike, *Phys. Lett.* **B 261** (1991) 321;
A.B. Arbuzov, D.Yu. Bardin and A. Leike, PHE-91-012.

[48] D.Yu. Bardin et al., Dubna Preprint E2-88-324.

[49] J.H. Kühn and R.G. Stuart, *Phys. Lett.* **B 200** (1988) 360;
S. Jadach, J.H. Kühn, R.G. Stuart and Z. Was, *Z. Phys.* **C 38** (1988) 609.

[50] Z. Wąs and S. Jadach, *Phys. Lett.* **B 219** (1989) 103.

[51] J.E. Campagne and R. Zitoun, *Z. Phys.* **C 43** (1989) 469.

[52] F.A. Berends, G.J.H. Burgers and W.L. van Nerven, *Nucl. Phys.* **B 297** (1988) 429; Erratum *Nucl. Phys.* **B 304** (1988) 92.

[53] I. Bigi, *Phys. Lett.* **B 155** (1985) 125.

[54] M.V. Danilov, Proceedings of the LP-HEP 91 Conference, Geneva 1991.

[55] K. Abe, Proceedings, Intern. Conference on HEP, Singapore 1990.

[56] J.H. Kühn, A. Reiter and P.M. Zerwas, *Nucl. Phys.* **B 272** (1986) 560.

[57] G. Köpp, L.M. Sehgal and P.M. Zerwas, *Nucl. Phys.* **B 123** (1977) 77.

[58] J.D. Bjorken, *Phys. Rev.* **D 40** (1989) 1513.

[59] A. Czarnecki, M. Jezabek, T. Körner and T.H. Kühn, *Phys. Rev. Lett.* **73** (1994) 384;
G. Bonvicini and L. Randall, *Phys. Rev. Lett.* **73** (1994) 392.

[60] R.H. Dalitz, G.R. Goldstein and R. Marshall, *Z. Phys.* **C 43** (1989) 441.

[61] R.D. Field and R.P. Feynman, *Nucl. Phys.* **B 136** (1978) 1.

[62] A. Ali, E. Pietarinen, G. Kramer and J. Willrodt, *Phys. Lett.* **B 93** (1980) 155.

[63] B. Andersson, G. Gustafson, G. Ingelman and T. Sjöstrand, *Phys. Reports* **C 97** (1983) 33.

[64] G. Marchesini and B.R. Webber, *Nucl. Phys.* **B 310** (1988) 461.

[65] G. Altarelli and G. Parisi, *Nucl. Phys.* **B 126** (1977) 298.

[66] I. Bigi, Y.L. Dokshitzer, V.A. Khoze, J. Kühn and P. Zerwas, *Phys. Lett.* **B 181** (1986) 157.

[67] B. Mele and P. Nason, *Phys. Lett.* **B 245** (1990) 635.

[68] P. Roudeau, Proceedings, Lepton–Photon Symposium, Geneva 1991.

[69] J.D. Bjorken, *Phys. Rev.* **D 17** (1978) 171.

[70] C. Peterson, D. Schlatter, I. Schmitt and P. Zerwas, *Phys. Rev.* **D 27** (1983) 105.

[71] X. Artru and G. Mennessier, *Nucl. Phys.* **B 70** (1974) 93.

[72] D.A. Morris, *Nucl. Phys.* **B 313** (1989) 634.

[73] B. Andersson, G. Gustafson and B. Söderberg, *Z. Phys.* **C 20** (1983) 317.

[74] M.G. Bowler, *Z. Phys.* **C 11** (1981) 169.

[75] N.A. Campbell, A. Huntley and C. Michael, *Nucl. Phys.* **B 306** (1988) 51;
K.D. Born, E. Laermann, R. Sommer, T.F. Walsh and P.M. Zerwas, *Phys. Lett.* **B 329** (1994) 325.

[76] J.G. Körner, G. Schierholz and J. Willrodt, *Nucl. Phys.* **B 185** (1981) 365.

[77] M. Bengtsson and P.M. Zerwas, *Phys. Lett.* **B 208** (1988) 306.

[78] R. Barate et al. [Aleph Coll.], CERN–PPE/97–002 and *Z. Phys.* C in press.

[79] B. Adeva et al. [L3 Coll.], *Phys. Lett.* **B 248** (1990) 227.

[80] L. Lönnblad, C. Peterson and T. Rögnvaldsson, *Phys. Rev. Lett.* **65** (1990) 1321; *Nucl. Phys.* **B 349** (91) 675.

[81] O. Nachtmann and A. Reiter, *Z. Phys.* **C 16** (1982) 45.

[82] W. Bartel et al., *Phys. Lett.* **B 101** (1981) 129; and *Phys. Lett.* **B 134** (1984) 275;
H. Aihara et al., *Z. Phys.* **C 28** (1985) 31.

[83] Ya.I. Azimov, Yu.L. Dokshitzer, V.A. Khoze and S.I. Troyan, *Phys. Lett.* **B 165** (1985) 147.

[84] V. Barger, K. Cheung, and W.Y. Keung, *Phys. Rev.* **D 41** (1990) 1541.

[85] G.T. Bodwin, E. Braaten, and G.P. Lepage, *Phys. Rev.* **D 51** (1995) 1125.

[86] K. Cheung, W.Y. Keung, and T.C. Yuan, *Phys. Rev. Lett.* **76** (1996) 877; P. Cho, *Phys. Lett.* **B 368** (1996) 171.

[87] G.C. Branco, H.P. Nilles and K.H. Streng, *Phys. Lett.* **B 85** (1979) 269.

[88] K. Hagiwara et al., *Phys. Lett.* **B 267** (1991) 527; Erratum *Phys. Lett.* **B 316** (1993) 631.

[89] Opal Collaboration, G. Alexander et al., *Phys. Lett.* **B 384** (1996) 343.

[90] V.M. Driesen, J.H. Kühn, and E. Mirkes, *Phys. Rev.* **D 49** (1994) 3197, and references therein.

[91] E. Braaten and Yu-Qi Chen, *Phys. Rev. Lett.* **76** (1996) 730.

[92] H. Fritzsch and J.H. Kühn, *Phys. Lett.* **B 90** (1980) 164.

[93] F. Amiri and C.R. Ji, *Phys. Rev.* **D 35** (1987) 3318.

[94] E. Braaten, K. Cheung, and T.C. Yuan, *Phys. Rev.* **D 48** (1993) R5049.

[95] V.V. Kiselev, A.K. Likhoed, M.V. Shevlyagin, Phys. Atom. Nucl. **57** (1994) 689.

[96] A. Leike and R. Rückl, Nucl. Phys. (Proc. Supp.) **37B** (1994) 215, and references therein.

[97] Delphi Coll., P. Abreu et al., CERN-PPE/96-194.

[98] C.H. Shepherd-Themistocleous, Proceedings, 28th Intern. Conference on HEP, Warsaw 1996, Z. Ajduk and A. Wróblewski (eds.), World Scientific.

[99] P.N. Ratoff, ibid., p. 884.

[100] J.D. Richman, ibid., p. 143.

[101] M. Bosman and R. Rückl in Ref. [11] and references therein.

[102] M. Neubert and B. Stech, hep-ph/9705292, in *Heavy Flavours II*, World Scientific (1997), A.J. Buras and M. Lindner (eds.).

[103] A. Buras and J. Fleischer, hep-ph/9704376, in *Heavy Flavours II*, World Scientific (1997), A.J. Buras and M. Lindner (eds.).

[104] B. Datta, E.A. Paschos and U. Türke, *Phys. Lett.* **B 196** (1987) 382.

[105] L.K. Gibbons, Proceedings, 28th Intern. Conference on HEP, Warsaw 1996, Z. Ajduk and A. Wróblewski (eds.), World Scientific.

[106] G. Gratta et al., *Nouvo Cim.* **103A** (1990) 821.

[107] H. Albrecht et al. (ARGUS), *Phys. Lett.* **B 192** (1987) 245;
M. Artuso et al. (CLEO), *Phys. Rev. Lett.* **62** (1989) 2233.

[108] C. Quigg, "Top–ology", Report FERMILAB–Pub–97/091–T.

[109] LEP Electroweak Working Group, R. Clare et al., "A Combination of Preliminary Electroweak Measurements and Constraints on the Standard Model", CERN Report CERN–PPE/96–183.

[110] G.L. Kane and M.E. Peskin, *Nucl. Phys.* **B 195** (1982) 29.

[111] C. Albajar et al. [UA1 Coll.], *Phys. Lett.* **B 255** (1991) and Erratum *Phys. Lett.* **B 262** (1991) 497.

[112] D. Schaile and P.M. Zerwas, *Phys. Rev.* **D 45** (1992) 3262.

[113] M. Veltman, *Act. Phys. Pol.* **B 8** (1977) 475.

[114] M. Chanowitz, M. Furman and I. Hinchliffe, *Nucl. Phys.* **B 153** (1979) 402.

[115] N. Cabibbo, L. Maiani, G. Parisi and R. Petronzio, *Nucl. Phys.* **B 158** (1979) 296.

[116] M. Lindner, *Z. Phys.* **C 31** (1986) 295.

[117] J.H. Kühn, *Act. Phys. Pol.* **B 12** (1981) 347;
J.H. Kühn, *Act. Phys. Austr.* **Suppl.XXIV** (1982) 203.

[118] J.H. Kühn and K.H. Streng, *Nucl. Phys.* **B 198** (1982) 71.

[119] M. Jeżabek and J.H. Kühn, *Nucl. Phys.* **B 320** (1989) 20.

[120] A. Czarnecki, M. Jeżabek and J.H. Kühn, *Nucl. Phys.* **B 351** (1991) 70;
A. Czarnecki, M. Jeżabek, J.G. Körner, and J.H. Kühn, *Phys. Rev. Lett.* **73** (1994) 384;
A. Czarnecki and M. Jeżabek, *Nucl. Phys.* **B 427** (1994) 3.

[121] M. Jeżabek and J.H. Kühn, *Phys. Lett.* **B 239** (1994) 317.

[122] M. Schmitt, in Workshop Report on e^+e^- Linear Colliders DESY 96-123D, p. 67, P.M. Zerwas (ed.).

[123] M. Jeżabek and J.H. Kühn, *Nucl. Phys.* **B 314** (1989) 1.

[124] A. Denner and T. Sack, *Nucl. Phys.* **B 358** (1991) 46.
A. Czarnecki, *Phys. Lett.* **B 252** (1990) 467.
C.S. Li, R.J. Oakes, T.C. Yuan, *Phys. Rev.* **D 43** (1991) 3759.

[125] B. H. Smith and M. B. Voloshin, *Phys. Lett.* **B 340** (1994) 176.

[126] A. Czarnecki, *Act. Phys. Pol.* **B 26** (1995) 845.

[127] S. J. Brodsky, G. P. Lepage, and P. B. Mackenzie, *Phys. Rev.* **D 28** (1983) 228.

[128] A. Czarnecki, *Phys. Rev. Lett.* **76** (1996) 4124.

[129] A. Czarnecki and K. Melnikov, TTP97-08, hep-ph/9703277 and TTP97-05, hep-ph/9703291.

[130] A. Czarnecki, M. Jeżabek and J.H. Kühn, *Act. Phys. Pol.* **B 20** (1989) 961.

[131] G. Eilam,R.R. Mendel, R. Migneron and A. Soni, *Phys. Rev. Lett.* **66** (1991) 3105.

[132] A. Denner and A.H. Hoang, Nucl. Phys. **B397** (1993) 483.

[133] M. Jeżabek and J. H. Kühn, *Phys. Rev.* **D 48** (1993) R1910; E: ibid. **D49** (1994) 4970.

[134] G.L. Kane, Proceedings, Madison Workshop 1979;
I. Bigi et al. in Ref.[66];
J.F. Gunion, H.E. Haber, G. Kane and S. Dawson, *The Higgs Hunter's Guide*, Addison–Wesley 1990;
C.S. Li and T.C. Yuan, *Phys. Rev. Lett.* **42** (1990) 3088.

[135] J. Gunion et al., Ref.[134];
A. Mendez and A. Pomarol, *Phys. Lett.* **B 252** (1990) 461;
C.S. Li and R.J. Oakes, *Phys. Rev.* **D 43** (1991) 855.

[136] K. Hikasa and M. Kobayashi, *Phys. Rev.* **D 36** (1987) 724.

[137] F. M. Borzumati and N. Polonsky, in Workshop Report on e^+e^- Linear Colliders DESY 93-123D, p. 41, P.M. Zerwas (ed.).

[138] J. Ellis and S. Rudaz, *Phys. Lett.* **B 128** (1983) 248;
A. Bouquet, J. Kaplan and C. Savoy, *Nucl. Phys.* **B 262** (1985) 299.

[139] A. Venturi, Workshop Report on e^+e^- Linear Colliders DESY 96-123D, p. 269, P.M. Zerwas (ed.).

[140] G. Eilam, J.L. Hewett and A. Soni, *Phys. Rev.* **D 44** (1991) 1473.

[141] H. Fritzsch, *Phys. Lett.* **B 224** (1989) 423.

[142] W. Buchmüller and M. Gronau, *Phys. Lett.* **B 220** (1989) 641.

[143] M. Glück, J.F. Owens and E. Reya, *Phys. Rev.* **D 15** (1978) 2324;
B.L. Combridge, *Nucl. Phys.* **B 151** (1979) 429.

[144] S. Willenbrock and D.A. Dicus, *Phys. Rev.* **D 34** (1986) 155;
C.–P. Yuan, *Phys. Rev.* **D 41** (1990) 42.

[145] P. Nason, S. Dawson and R. K. Ellis, *Nucl. Phys.* **B 303** (1988) 607; *ibid.* **B**327 (1989) 49.

[146] W. Beenakker, H. Kuijf, W. L. van Neerven and J. Smith, *Phys. Rev.* **D 40** (1989) 54.

[147] R. Meng, G. A. Schuler, J. Smith and W. L. van Neerven, *Nucl. Phys.* **B 339** (1990) 325.

[148] S. Güsken, J. H. Kühn and P. M. Zerwas, *Phys. Lett.* **B 155** (1985) 185.

[149] V. Fadin, V. Khoze, *JETP Lett.* **46** (1987) 417; *Sov. J. Nucl. Phys.* **48** (1988) 487;
V. Fadin, V. Khoze and T. Sjöstrand, CERN-TH 5687/90.

[150] E. Laenen, J. Smith and W.L. van Neerven, *Nucl. Phys.* **B 369** (1992) 543.

[151] E.L. Berger and H. Contopanagos, *Phys. Lett.* **B 361** (1995) 115.

[152] S. Catani, M. Maugani, P. Nason and L. Trentadue, *Phys. Lett.* **B 378** (1996) 329.

[153] W. Beenakker, A. Denner, W. Hollik and T. Sack, *Nucl. Phys.* **B 411** (1994) 343.

[154] R.K. Ellis, *Phys. Lett.* **B 259** (1991) 492.

[155] K.J. Foley et al., Workshop on Experiments, Detectors and Experimental Areas for the Supercollider, Berkeley 1987.

[156] L. Fayard and G. Unal in Ref.[12].

[157] O.J.P. Eboli, G.C. Marques, S.F. Novales and A.A. Natale, *Phys. Rev.* **D 34** (1986) 771;
S. Dawson and S. Willenbrock, *Nucl. Phys.* **B 284** (1987) 449;
C.P. Yuan, *Nucl. Phys.* **B 310** (1988) 1;
R.P. Kauffman, *Phys. Rev.* **D 41** (1990) 3343;
H. Veltman, *Phys. Rev.* **D 43** (1991) 2236.

[158] K. Hagiwara, H. Murayama and T. Watanabe, *Nucl. Phys.* **B 367** (1991) 257.

[159] A. Djouadi, J. Kalinowski and P.M. Zerwas, DESY 91-104.

[160] M. Martinez and S. Orteu, in Workshop Report on e^+e^- Linear Colliders, DESY 96-123D, p. 75, P.M. Zerwas (ed.).

[161] M. Consoli, W. Hollik and F. Jegerlehner, in "Z Physics at LEP 1", G. Altarelli (ed.), CERN89-08.

[162] J. Jersak, E. Laermann and P.M. Zerwas, *Phys. Rev.* **D 25** (1982) 363;
J. Schwinger, "Particles, Sources and Fields", Addison-Wesley (1973);
L. Reinders, H. Rubinstein and S. Yazaki, *Phys. Reports* **C 127** (1985) 1.

[163] J. Schwinger in [162];
S. Güsken, J.H. Kühn and P. Zerwas, *Phys. Lett.* **B 155** (1985) 185.

[164] K.G. Chetyrkin, J.H. Kühn, and M. Steinhauser, *Nucl. Phys.* **B 482** (1996) 213.

[165] K.G. Chetyrkin, A. Hoang, J.H. Kühn, M. Steinhauser, and T. Teubner, *Phys. Lett.* **B 384** (1996) 233.

[166] K.G. Chetyrkin, J.H. Kühn, and M. Steinhauser, TTP97-18, hep-ph/9705254.

[167] A. Hoang, J.H. Kühn, and T. Teubner, *Nucl. Phys.* **B 452** (1995) 173.

[168] W. Beenakker, S.C. van der Marck and W. Hollik, *Nucl. Phys.* **B 365** (1991) 24.

[169] M. Jeżabek and J.H. Kühn, Phys. Lett. **B316** (1993) 360.

[170] B. Grzadkowski, P. Krawczyk, J.H. Kühn, and R.G. Stuart, Nucl. Phys. **B281** (1987) 18.

[171] G. Jikia, *Phys. Lett.* **B 257** (1991) 196.

[172] T. Sjöstrand and P.M. Zerwas, Proceedings, e^+e^- Collisions at 500 GeV: The Physics Potential, DESY 92–123A.

[173] G.L. Kane, G.A. Ladinsky and C.–P. Yuan, *Phys. Rev.* **D 45** (1992) 124.

[174] C. Schmidt and M.E. Peskin, Workshop on Physics and Experiments with Linear Colliders, Saariselkä 1991.

[175] W. Bernreuther et al. in Ref.[6];
W. Bernreuther, A. Brandenburg and P. Overmann, DESY 96-123D, p. 49.

[176] A. Devoto, J. Pumplin, W. Repko and G.L. Kane, *Phys. Rev. Lett.* **43** (79) 1062;

[177] G.L. Kane, Proceedings, SLAC Summer Institute 1990.

[178] J.H. Kühn, *Nucl. Phys.* **B 237** (1984) 77.

[179] I.F. Ginzburg et al., *Nucl. Inst. Meth.* **205** (1983) 47;
V.I. Telnov in Proc. Workshop "Physics with Linear Colliders", Saariselkä 1991, and references therein.

[180] F. Richard, LAL91-62 and references therein.

[181] S.Y. Choi and F. Schrempp, DESY 91-086.

[182] J. Steegborn, Diploma Thesis, University of Karlsruhe.

[183] V.S. Fadin and V.A. Khoze, *JETP Lett.* **46** (1987) 525,

[184] T. Appelquist, M. Dine and I. Muzinich, *Phys. Rev.* **D 17** (1978) 2074.

[185] L. Susskind, in "Weak and Electromagnetic Interactions at High Energies", Les Houches (1977).

[186] W. Fischler, *Nucl. Phys.* **B 129** (1977) 157.

[187] A. Billoire, *Phys. Lett.* **B 92** (1980) 343.

[188] M. Peter, *Phys. Rev. Lett.* **78** (1997) 602.

[189] J.M. Strassler and M.E. Peskin, *Phys. Rev.* **D 43** (1991) 1500.

[190] M. Reżabek, J.H. Kühn and T. Teubner, *Z. Phys.* **C 56** (1992) 653.

[191] M. Reżabek and T. Teubner, *Z. Phys.* **C 59** (1993) 669.

[192] For a pedagogical discussion see e.g. the appendix of W. Buchmüller and S.-H. H. Tye, Phys. Rev. **D24** (1981) 132.

[193] K. Fujii, Lectures presented at SLAC Summer Institute on Particle Physics, Stanford 1995.

[194] P. Igo-Kemenes, M. Martinez, R. Miguel, and S. Orteu, in Proceedings, e^+e^- *Collisions at 500 GeV: The Physics Potential*, Part C; P.M. Zerwas (ed.), DESY 93-123C, p. 319.

[195] R. Guth and J.H. Kühn, Nucl. Phys. **B368** (1992) 38.

[196] P. Comas, R. Miquel, M. Martinez, and S. Orteu, DESY 96-123D, p. 59.

[197] Y. Sumino, K. Fujii, K. Hagiwara, H. Murayama, C.-K. Ng, *Phys. Rev.* **D 47** (1993) 56

[198] For a detailed and pedagogical discussion of the interplay between the QCD potential and the momentum distribution see M. Ježabek, J.H. Kühn, and T. Teubner, DESY 93–123C, p. 303, and [14].

[199] R. Harlander, M. Ježabek, J.H. Kühn and T. Teubner, *Phys. Lett.* **B 346** (1995) 137.

[200] H. Murayama and Y. Sumino, *Phys. Rev.* **D 47** (1993) 82.

[201] R. Harlander, M. Ježabek, J.H. Kühn, and M. Peter, Z. Phys. **C73** (1997) 477.

[202] K. Melnikov and O. Yakovlev, *Phys. Lett.* **B 324** (1994) 217.

[203] Y. Sumino, PhD Thesis, University of Tokyo, 1993 (unpublished).

[204] R.W. Huff, *Ann. Phys.* **16** (1961) 288.

[205] K. Fujii, T. Matsui and Y. Sumino, *Phys. Rev.* **D 50** (1994) 4341.

[206] H. Überall, *Phys. Rev.* **119** (1960) 365.

[207] W. Mödritsch and W. Kummer, *Nucl. Phys.* **B 430** (1994) 3.